SYNTHESIS AND CHARACTERISATION OF LANTHANIDE COMPLEXES WITH NITROGEN- AND OXYGEN-DONOR LIGANDS

Tatenda Madanhire

2016

SYNTHESIS AND CHARACTERISATION OF LANTHANIDE COMPLEXES WITH NITROGEN- AND OXYGEN-DONOR LIGANDS

By

Tatenda Madanhire

Submitted in fulfillment of the requirements for the degree of Magister Scientiae to be awarded at the Nelson Mandela Metropolitan University

January 2016

Supervisor: Dr A. Abrahams

DECLARATION BY STUDENT

FULL NAME: Tatenda Madanhire

STUDENT NUMBER: 210154810

QUALIFICATION: MSc Chemistry

TITLE OF PROJECT: Synthesis and characterisation of lanthanide complexes with nitrogen- and oxygen-donor ligands

DECLARATION:

In accordance with Rule G5.6.3, I hereby declare that this dissertation is my own work and that it has not previously been submitted for assessment to another University or for another qualification.

SIGNATURE: _____

DATE: _____

DEDICATION

To my parents, Joram and Mavis

Table of contents

CHAPTER 4

Nd(III), Gd(III) and Ho(III) complexes with an o-vanillin derived Schiff base ligand

CHAPTER 5

Decomposition of an o-vanillin derived Schiff base ligand and its dinuclear Ce(III) complex

CHAPTER 6

Lanthanide-assisted conversion of thiosemicarbazones and thiosemicarbazides

Acknowledgements

I would like to thank my supervisor, Dr Abubak'r Abrahams for assisting and guiding me through my research. His endless support is greatly appreciated.

My sincere thanks go to Drs Eric Hosten and Richard Betz for their assistance with SC-XRD analyses, as well as Mr Henk Schalekamp for his technical support.

I wish to express my gratitude for the assistance given by Dr Percy Hlangothi and Mr Lukanyo Bolo for thermal analysis. Without them it would have been an impossible task.

I would like to deeply thank Mr Janvier Mukiza, Mr Gratien Habarurema, Mr Cameron Mathews, Mr Kwakhanya Mkwakwi and Mr Louis-Charl Coetzee for their insight and valued advice.

Many thanks go to the National Research Foundation (NRF) and Nelson Mandela Metropolitan University for providing an opportunity and facilities to execute my research.

I would like to acknowledge my brother, Godfrey and family for their endless love, support and motivation. Thank you for believing in my ability to succeed.

Lastly, I would like to thank God, the creator of chemistry, for being my source of knowledge and strength.

Abstract

The reactions of $Ln(NO_3)_3 \cdot 6H_2O$ (Ln = Pr, Nd or Er) with the potentially tridentate *O,N,O* chelating ligand 2,6-pyridinedimethanol (H_2pydm) were investigated, and complexes with the formula, $[Ln(H_2pydm)_2(NO_3)_2](NO_3)$ (Ln = Pr or Nd) and $[Er(H_2pydm)_3](NO_3)_3$ were isolated. The ten-coordinate Pr(III) and Nd(III) compounds crystallise in the triclinic space group P-1 while the nine-coordinate Er(III) complex crystallises in the monoclinic system ($P2_1/n$). The reaction of $PrCl_3 \cdot 6H_2O$ with H_2pydm yielded the compound, $[Pr(H_2pydm)_3](Cl)_3$, that crystallises in the monoclinic system, space group $P2_1/c$ with $\alpha = 90$, $\beta = 98.680(1)$ and $\gamma = 90°$. The nine-coordinate Pr(III) ion is bound to three H_2pydm ligands, with bond distances Pr-O 2.455(2)-2.478(2) Å and Pr-N 2.6355(19)-2.64(2) Å. X-ray crystal structures of all the H_2pydm complexes reveal that the ligand coordinates tridentately, *via* the pyridyl nitrogen atom and the two hydroxyl oxygen atoms. The electronic absorption spectra of complexes show 4*f*-4*f* transitions.

Rare-earth complexes, $[Ln(H_2L_1)_2(NO_3)_3]$ [Ln = Gd, Ho or Nd], were also prepared from a Schiff base. The X-ray single-crystal diffraction studies and SHAPE analyses of the Gd(III) and Ho(III) complexes shows that the complexes are ten-coordinate and exhibit distorted tetradecahedron geometries. With proton migration occurring from the phenol group to the imine function, complexation of the lanthanides to the ligand gives the ligand a zwitterionic phenoxo-iminium form.

A phenolate oxygen-bridged dinuclear complex, $[Ce_2(H_2L_1)(ovan)_3(NO_3)_3]$, has been obtained by reacting $Ce(NO_3)_3 \cdot 6H_2O$ with an *o*-vanillin derived Schiff base ligand, 2-((*E*)-(1-hydroxy-2-methylpropan-2-ylimino)methyl)-6-methoxyphenol (H_2L_1). Hydrolysis of the Schiff base occurred to yield *o*-vanillin, which bridged two cerium atoms with the Ce···Ce distance equal to 3.823 Å. The Ce(III) ions are both ten-coordinate, but have different coordination environments, showing tetradecahedron and staggered dodecahedron geometries, respectively.

The reaction of salicylaldehyde-*N*(4)-diethylthiosemicarbazone (H_2L_2) in the presence of hydrated Ln(III) nitrates led to the isolation of two novel compounds: (*E*)-2-[(*ortho*-hydroxy)benzylidene]-2-(thiomethyl)-thionohydrazide (**1**) and bis[2,3-diaza-4-(2-hydroxyphenyl)-1-thiomethyl-buta-1,3-diene]disulfide. The latter is a dimer of the former. For this asymmetric Schiff base, **1** and the symmetric disulfide, classical hydrogen bonds of the O–H···N as well as N–H···S (for **1**) type are apparent next to C–H···O contacts. 4-(4-Bromophenyl)-1-(propan-2-ylidene)thiosemicarbazide was also prepared upon reacting 4-(4-bromophenyl)-3-thiosemicarbazide with acetone in the presence of ethanol and $La(NO_3)_3{\cdot}6H_2O$. The C=S bond length was found to be 1.6686(16) Å which is in good agreement with other thioketones whose metrical parameters have been deposited with the Cambridge Structural Database. Classical hydrogen bonds of the N–H···N and the N–H···Br type are observed next to C–H···S contacts.

All synthesised compounds were characterised by microanalyses, single-crystal X-ray diffraction (except for $[Nd(H_2L_1)_2(NO_3)_3]$), ^{1}H NMR and IR spectroscopy.

Keywords: Lanthanide, Schiff base, thiosemicarbazone, thiosemicarbazide, bidentate, tridentate, crystal structure, geometry

Crystallographic data

Supplementary data for all the crystal structures reported herein are stored on the compact disc that is attached to the inside back cover of this dissertation.

The crystallographic data include:

- Final crystal data and details of the structure determinations
- Final coordinates and equivalent isotropic displacement parameters of the non-hydrogen atoms
- Hydrogen atom positions
- Isotropic displacement parameters
- All bond distances and bond angles
- Torsion angles
- Contact distances
- Hydrogen bonds

CHAPTER 1

Introduction

1.1 Motivation of study

Cancer is a collection of many related diseases that results from uncontrolled growth and spread of abnormal cells in the body and affects a significant number of people world-wide. Normally, body cells divide and grow to produce more cells when needed by the body. However, sometimes this process goes wrong, and more cells are created even when they are not needed [1]. This forms masses of tissue called tumours that are either benign (non-cancerous) or malignant (cancerous). Benign tumours can be removed and are not a big threat to life while cancer cells can break away from malignant tumours, invade and damage tissues and organs as they grow rapidly and uncontrollably. Various parts of the body affected include the prostate, lungs, oesophagus, bladder, cervix and breasts. According to GLOBOCAN findings in 2012, there were an estimated 14.1 million new cancer cases globally and 8.2 million cancer-related deaths.

For the past 10 years the number of researchers trying to increase the pool of available radiopharmaceuticals has increased significantly. At the forefront of these investigations were the elements rhenium and technetium, regarded as the workhorses of cancer diagnostic and therapeutic agents. Some of the platinum-based drugs such as cisplatin have been applied efficiently, but only for a limited range of cancers [2]. However, the use of cisplatin and other platinum complexes as anticancer agents is limited due to notable toxic side effects experienced such as kidney toxicity and nausea or intrinsic resistance [3,4]. Therefore, there is an urgent need to design new metal-based therapeutics with a broader spectrum of antitumour activity and improved pharmacological properties.

Recently, the isotopes of the 4*f* elements are playing an increasingly important role in nuclear medicine. An example is a β-emitter, ^{177}Lu ($t_{1/2}$ = 6.7 days, Eγ = 0.5 MeV), that possesses an imageable γ-emission [5]. A less energetic maximum γ radiation of 0.5 MeV and a small tumour cell-killing range ensures more selectivity and results in lower damage to normal tissues [6]. Some rare-earth radionuclides of choice for diagnostic and therapeutic purposes include ^{165}Er ($t_{1/2}$ = 10.3h, E_γ = 48.54 keV) which is applied as a tumour localising agent, ^{167}Tm ($t_{1/2}$ = 9.6 days, E_γ = 532 keV) used in tumour studies and ^{169}Yb ($t_{1/2}$ = 32 days, E_γ = 197.9 keV) that is utilised in tumour scanning. Erbium-165, known primarily as a bone seeker radionuclide, is injected intraperitoneally at a pH of 5 as ^{165}Er-citrate [7,8]. Isotopes of interest are ^{149}Tb, which is used as a toxin in targeted cancer therapy and ^{166}Ho which is applied in hepatic tumours and ovarian cancer [7].

Lanthanides (Lns) are of interest not only because of their therapeutic radioisotopes but also their ability to form complexes with variations in the identities of coordinating ligands, wide range of coordination numbers and molecular geometries. Rare-earth complexes offer potential advantages in medicinal inorganic chemistry due to their accessible redox states as well as broader structural diversity. The lanthanide compounds also exhibit interesting and unique photophysical, electrochemical and spectroscopic properties which may be of great significance in diagnosis [9,10]. Thus, new lanthanide complexes can be produced that bind to DNA in a different way than cisplatin; which can be used to overcome resistance [11]. The coordination chemistry of the lanthanides may provide an effective alternative to radiopharmaceutical development since lanthanide compounds are expected to be active in preventing tumour growth by competitively suppressing iron uptake thereby inhibiting reactive oxygen species (ROS) formation by binding to hydro-peroxides and masking the free radicals [12].

Pyridine is a heterocyclic organic compound that has been found to exhibit anticancer activity. Its derivatives such as pyridine epithilones and 2,6-diaryl-substituted pyridines have been discovered to show cytotoxic properties against several human cancer cell lines. Examples of these derivatives that have been reported to exhibit

cytotoxicity as well as topoisomerase 1 inhibitory activity are given in Figure 1 [13]. Several 2,6-bis(substituted) pyridine Ag(I) nitrate complexes were synthesised, characterised and evaluated for their *in vitro* anticancer activity against human cancer cell lines that include colon carcinoma (HT29), lung adenocarcinoma (A549) and breast adenocarcinoma (MCF7). Pyridine derivatives that were used in the complexation are pyridine-2,6-bis((*E*)-2-(2-phenylhydrazono)-3-oxopropanenitrile), pyridine-2,6-bis(2-cyano-N-phenyl-3-oxopropanethioamide) and pyridine-2,6-bis(3-oxopropanenitrile) [14]. Therefore, metal complexes of the pyridine derivative 2,6-pyridinedimethanol are relevant (Figure 2).

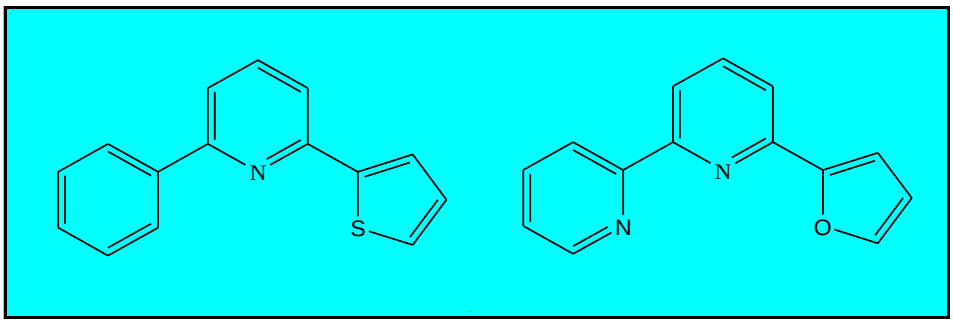

Figure 1: 2,6-substituted pyridines which exhibit anticancer activity.

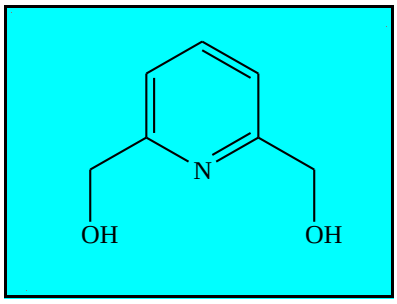

Figure 2: Structure of 2,6-pyridinedimethanol.

Thiosemicarbazones (TSCs) and Schiff bases are of significant interest because of their potentially beneficial antitumour activities [15-19]. Some of the derivatives of these compounds are also known to exhibit the same biological activities [20,21]. An example of a recently developed anticancer drug is triapine (3-aminopyridine-2-carboxaldehyde thiosemicarbazone) that has reached clinical phase II trials on several cancer cell lines. Thus, TSCs are receiving more attention presently due to their potential use against cancer in which their action has been shown to involve

interaction with heavy metal ions. Their antitumour activity is extremely selective and is dependent on the typology of tumour cells [22,23].

1.2 The Chemistry of the Lanthanides

1.2.1 Physical properties

The lanthanides are silvery white in colour and generally have high melting and boiling points between approximately 1000 and 3000 ^{o}C, respectively. These hard elements are good conductors of heat and electricity, and also exhibit paramagnetism (except La^{3+} and Lu^{3+}) [24-26]. The Ln^{3+} ions impart paramagnetism both to their solutions and solid compounds.

1.2.2 Chemical properties

A notable feature of the lanthanides is their ability to form chemical bonds with various non-metals. The rare-earth elements readily react in air to produce basic trioxides, except for cerium which forms a dioxide (CeO_2). Some lanthanides also combine with the non-metals nitrogen, hydrogen (to form hydrides, LnH_2), sulfur, carbon (to form carbides) and halogens (to give halides). However, Ln-C bonds are unstable under normal conditions. Reaction of the lanthanides with water also occurs to yield hydroxides [$Ln(OH)_3$] and hydrogen. They react with dilute acids thereby liberating hydrogen [25,26]. According to the hard-soft acid-base (HSAB) theory, the lanthanides are considered to be hard Lewis acids with a great affinity for hard oxygen and nitrogen donor-atoms in preference to sulfur and phosphorous [27,28]. Although many nitrogen containing complexes have been successfully prepared, many of these are hydrolytically unstable regardless of their thermal stability. The hydrolytic instability of the Ln–N bonds is suggested to result from the basicity behaviour of lanthanide ions in aqueous solutions having nitrogen containing ligands [29].

Lanthanide ions have a very small crystal-field stabilisation energy (about 6 kJ/mol) compared to the transition metal ions that have ligand-field effects in the range of 120-360 kJ/mol. As a result, the 4*f* electrons are chemically inert and do not readily form covalent bonds with ligands [30-32]. Lanthanide compounds are thus ionic and contain the metal in the +2, +3 or +4 oxidation states. Therefore, complex geometry is determined by steric and not electronic factors. The variation in chemical behaviour of the lanthanides may be attributed to the decrease in ionic radii across the series due to the lanthanide contraction. However, the chemical properties of the rare-earths are almost similar since the change in ionic radii of the lanthanides is very small. For this reason, separation of the elements in a pure state is difficult [30-33].

1.2.3 Lanthanide contraction

An important feature of the lanthanides is the lanthanide contraction: a steady decrease in atomic and ionic radii with increasing atomic number. This contraction is due to the ineffective screening of the nucleus by the 4*f* electrons, leading to a stronger attraction of the electrons to the nucleus in the outermost shell as the nuclear charge increases. The net result is a contraction in the atomic radius (see Table 1). The shielding effect of 4*f* electrons in lanthanide atoms is not as strong as that in lanthanide ions, and for this reason the lanthanide contraction is weaker in Ln atoms than in Ln^{3+} ions [25,26,33,34].

The lanthanide contraction is responsible for regular variations in the properties of lanthanides as atomic number increases. For instance, an increase in atomic number results in the increase in the stability constant of lanthanide complexes as well as a decrease in the alkalinity of Ln ions. In addition, there is a regular decrease in the pH at which hydrates start to precipitate from an aqueous solution with the increase in atomic number [34].

As the size of the lanthanide ions decreases from La^{3+} to Lu^{3+}, the ability to form complex ions increases and the lanthanides are therefore separated on an ion-exchange column based on this factor [33]. The lanthanide contraction also ascribes

for the covalent character of the lanthanide hydroxides. As ionic radii decreases, the covalent nature of the hydroxides increases leading to a decrease in basic strength. Therefore, $La(OH)_3$ is the most basic while $Lu(OH)_3$ has the least basicity [34,35].

Table 1: Atomic and ionic radii of lanthanides to show contraction [34].

Element	**Atomic number**	**Atomic radius (nm)**	**Ionic radius Ln^{3+} (nm)**
Lanthanum	57	0.187	0.115
Cerium	58	0.183	0.111
Praseodymium	59	0.182	0.109
Neodymium	60	0.181	0.108
Promethium	61	-	0.106
Samarium	62	0.179	0.104
Europium	63	0.204	0.112
Gadolinium	64	0.180	0.102
Terbium	65	0.178	0.100
Dysprosium	66	0.177	0.099
Holmium	67	0.176	0.097
Erbium	68	0.175	0.096
Thulium	69	0.174	0.095
Ytterbium	70	0.194	0.094
Lutetium	71	0.174	0.093

1.2.4 Geometries/ Stereochemistry

The lanthanides have coordination numbers ranging from three to twelve, with the most common coordination numbers being eight and nine. This is greater than that of transition metals which generally forms four- to six-coordinate complexes. These higher coordination numbers are due to the fact that the 4*f* elements have larger ionic

radii that can accommodate more ligands. The other reason being that the sum of the 6*s*, 6*p* and 5*d* orbitals is close to the coordination number of twelve (see Table 2) [27,28,34,36,37].

Table 2: Different coordination numbers and geometries adopted by various lanthanides.

Coordination number	Complex	Geometry
3	$[La\{CH(SiMe_3)_2\}_3]$	Pyramidal
4	$[Lu(2,6\text{-dimethylphenyl})_4]^-$	Tetrahedral
5	$[Er(CH_2SiMe_3)_3(thf)_2]$	Trigonal bipyramidal
6	$[YbCl_3(thf)_3]$	Octahedral
7	$[Pr(thf)_4Cl_3]$	Pentagonal bipyramidal
7	$[EuCl_7]^{4-}$ in Ba_2EuCl_7	Capped trigonal prismatic
8	$(Ph_4As)[Ln(S_2PEt_2)_4]$	Dodecahedral
8	$(Ph_4P)[Pr(S_2PMe_2)_4]$	Square antiprismatic
9	$[Nd(H_2O)_9]^{3+}$	Tri-capped trigonal prismatic
10	$[Pr(H_2O)_{10}]^{3+}$	Triangular cupola
12	$[Ce(NO_3)_6]^{2-}$	Icosahedral

A key breakthrough in understanding the ability of the lanthanides to give rise to high coordination numbers was made possible by the use of relatively fast X-ray diffraction methods, for example the establishment of the nine-coordinate tricapped trigonal prismatic coordination compound $[Nd(H_2O)_9](BrO_3)_3$ in 1939. As late as

1963 the chemist, H.J. Emeleus, stipulated that the rare-earths could form six-coordinate complexes [38].

The coordination number in rare-earth complexes is to a greater extent influenced by crowding in the coordination sphere, strength of the positively-charged metal ion and the electron-rich ligand [30]. Crowding in the coordination sphere can be explained by two factors, namely *first-order* and *second-order* steric effects. For *first-order* crowding, there is congestion among the donor-atoms directly bonded to the Ln^{3+} ion and inter-donor atom repulsions prevent more atoms from packing in direct interaction with the lanthanide. This results in complexes with normal or high coordination numbers. Hydroxide, water, halide and oxide ions are examples of such donors. For *second-order* crowding, groups such as $–CH(SiMe_3)_2$, $–N(SiMe_3)_2$ and bulky aryloxides and alkoxides attached to the donor-atoms, interact and determine how many of the ligands can bind to the lanthanide, leading to low coordination numbers [38]. Therefore, larger coordination numbers are attainable with small ligands such as SO_4^{2-} and NO_3^- and larger lanthanide ions, whereas ligands with bulky substituents lead to lower coordination numbers [39,40].

Ligands with small bite angles such as NO_3^- can also lead to higher coordination numbers, for example the twelve-coordinate $[Ln(NO_3)_6]^{3-}$ complex (Ln = La, Ce, Pr, Nd) [38,41].

1.2.5 Stable oxidation states

The most common and most stable oxidation state of the lanthanides is the +3 state. The sum of the first three ionisation energies of the lanthanides is relatively low, hence oxidation to the trivalent state. However, electrons are removed from the 5*d* and 6*s* subshells and not the 4*f* subshell due to the fact that 4*f* orbitals are shielded by the external 5*d* and 6*s* subshells, and therefore do not participate in bonding [25,26,34].

Although the +3 oxidation state is most common, some elements attain stable electronic configurations by losing 2 or 4 electrons to exhibit +2 and +4 oxidation

states. The +2 states are known in Sm, Eu and Yb, and the stability of the Sm^{2+}, Eu^{2+} and Yb^{2+} ions can be explained by their electronic configurations in the *f*-orbitals. The nearly half-filled $4f^6$ shell for Sm^{2+}, $4f^7$ half-filled shell for Eu^{2+} and the completely filled shell $4f^{14}$ for Yb^{2+} are all energetically stable according to Hund's rule [42]. Oxidation state +4 does exist for Ce, Pr, Tb and Dy. For cerium, loss of a further electron from Ce^{3+} to give Ce^{4+} results in an empty 4*f* shell which is energetically more favourable than the $4f^1$ subshell [34,43,44]. Possible oxidation states are listed in Table 3.

Table 3: Stable oxidation states of the lanthanides (most common state in bold) [39].

Element	**Electronic configuration**		**Oxidation states**
	Ground state	**Ln^{3+}**	
Lanthanum	$[Xe]4f^05d^16s^2$	$[Xe]4f^0$	**+3**
Cerium	$[Xe]4f^15d^16s^2$	$[Xe]4f^1$	**+3**,+4
Praseodymium	$[Xe]4f^35d^06s^2$	$[Xe]4f^2$	**+3**,+4
Neodymium	$[Xe]4f^45d^06s^2$	$[Xe]4f^3$	+2,**+3**
Promethium	$[Xe]4f^55d^06s^2$	$[Xe]4f^4$	+2,**+3**
Samarium	$[Xe]4f^65d^06s^2$	$[Xe]4f^5$	+2,**+3**
Europium	$[Xe]4f^75d^06s^2$	$[Xe]4f^6$	+2,**+3**
Gadolinium	$[Xe]4f^75d^16s^2$	$[Xe]4f^7$	**+3**
Terbium	$[Xe]4f^95d^06s^2$	$[Xe]4f^8$	**+3**,+4
Dysprosium	$[Xe]4f^{10}5d^06s^2$	$[Xe]4f^9$	**+3**,+4
Holmium	$[Xe]4f^{11}5d^06s^2$	$[Xe]4f^{10}$	**+3**
Erbium	$[Xe]4f^{12}5d^06s^2$	$[Xe]4f^{11}$	**+3**
Thulium	$[Xe]4f^{13}5d^06s^2$	$[Xe]4f^{12}$	+2,**+3**
Ytterbium	$[Xe]4f^{14}5d^06s^2$	$[Xe]4f^{13}$	+2,**+3**
Lutetium	$[Xe]4f^{14}5d^16s^2$	$[Xe]4f^{14}$	**+3**

The +2 and +4 states are converted to the +3 state, showing that it is the most stable oxidation state. For example, Ce^{4+} is strongly oxidising and Sm^{2+} is strongly reducing:

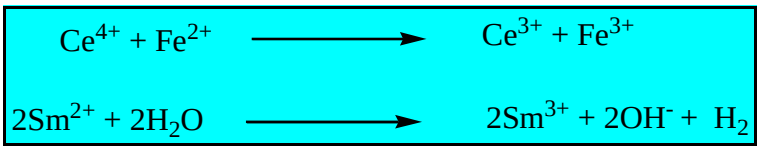

Pr^{4+} and Tb^{4+} are also good oxidizing agents in aqueous solution, whereas Eu^{2+} and Yb^{2+} loses an electron to attain the +3 state, and thus are good reducing agents [26,39,45].

1.2.6 Spectroscopic properties

The core-like behaviour of the 4*f* elements often gives line-like absorption spectra, resulting from *f-f* transitions [46]. The absorption spectra of the Ln complexes usually resemble that of the free ions because ligands have little effect on the 4*f* electrons, and are thus not influenced by the ligand-field [47]. Most Ln(III) compounds have transitions found in the near UV range, showing very weak or no absorption in the visible range [48]. The ground state configurations of the elements are given in Table 4 [31].

1.2.7 Lanthanide complexes with *O,N,O*-donor ligands

The La(III), Ce(III) and Eu(III) dipicolinate complexes with zero-dimensional structure have been synthesised by the mild hydrothermal technique. In these complexes the rare-earth ion is coordinated to 2,6-pyridinedicarboxylate groups in a tridentate mode, *via* the two oxygen atoms of the two carboxylate functions and one nitrogen atom. The nine-coordinate compounds exhibit distorted tricapped trigonal prism geometries. In the La(III) and Ce(III) complexes (Figure 3) the dipicolinate groups are in their dianionic form while in the Eu(III) complex the ligands are monoanionic [50].

Dipicolinic acid has also been utilised in the synthesis of heterometallic coordination polymers containing rare-earths, such as cerium. The ligand can form a nine-coordinate tris-chelate (*O,N,O*) with cerium(IV) and the free carboxylate oxygen atoms can interact with the alkali or alkaline-earth cations, such as barium [51-56].

Table 4: Electronic ground states of the Ln(III) ions [31,49].

Ion (Ln^{3+})	**Ground state**	**Colour**		**Ion (Ln^{3+})**	**Ground state**	**Colour**
La(III)	$^1S_0$	Colourless		Lu(III)	$^1S_0$	Colourless
Ce(III)	$^2F_{5/2}$	Colourless		Yb(III)	$^2F_{7/2}$	Colourless
Pr(III)	$^3H_4$	Green		Tm(III)	$^3H_6$	Green
Nd(III)	$^4I_{9/2}$	Violet		Er(III)	$^2I_{15/2}$	Pink
Pm(III)	$^5I_4$	Rose		Ho(III)	$^5I_8$	Yellow
Sm(III)	$^6H_{5/2}$	Cream		Dy(III)	$^6H_{15/2}$	Cream
Eu(III)	$^7F_0$	Pale pink		Tb(III)	$^7F_6$	Colourless
Gd(III)	$^8S_{7/2}$	Colourless				

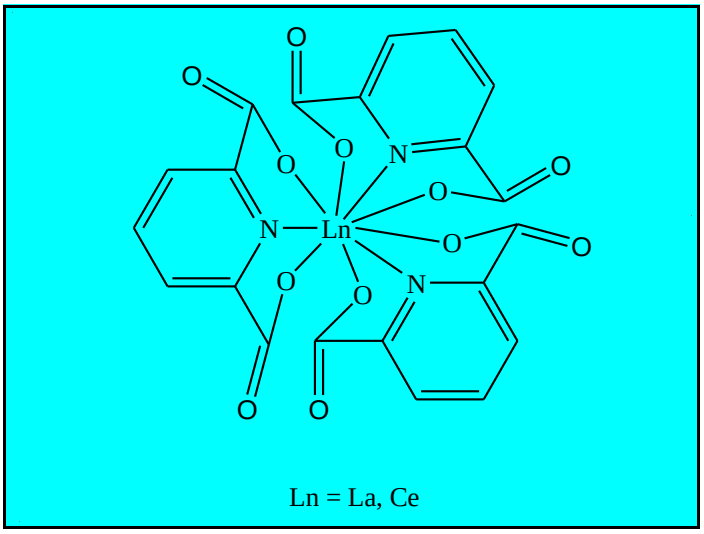

Figure 3: The structures of the La(III) and Ce(III) dipicolinate complexes. The guanidinium and piperazinium counter-ions for La(III) and Ce(III) complexes, respectively are omitted for clarity.

The samarium and dysprosium coordination compounds with the ligand, 6-diphenylamine carbonyl 2-pyridine carboxylic acid (HDPAP, Figure 4) have been synthesised and their luminescence properties have been investigated by An "*et al*" [57]. The crystal structure analyses revealed electroneutral nine-coordinate complexes with tricapped trigonal prism geometries. The ligand coordinates to each metal ion in a tridentate fashion through the pyridyl nitrogen atom, the carboxylate oxygen atom and the carbonyl oxygen atom. The coordination number of nine is achieved by complexation of three HDPAP molecules [57]. The samarium complex was found to emit characteristic red fluorescence of Sm(III) ions at room temperature whereas the Dy(III) complex emits the DPAP ligand phosphorescence.

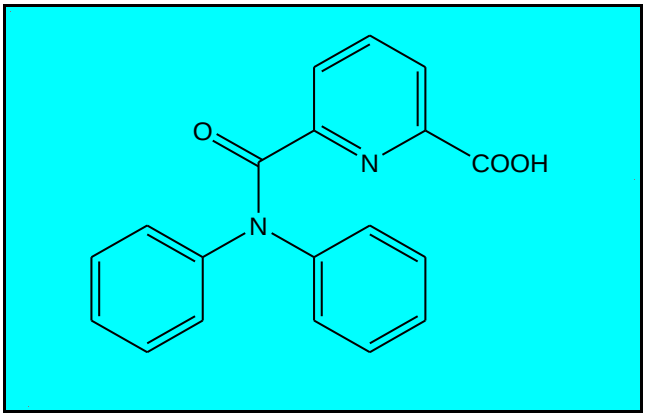

Figure 4: The structure of HDPAP.

1.2.8 Lanthanide complexes with Schiff bases

Schiff bases are products of the condensation reaction between carbonyl compounds and primary amines. The C=O group of an aldehyde or ketone is replaced by the azomethine group with the general formula $R_1HC=N-R_2$, where R_1 and R_2 are aryl, alkyl, heterocyclic or cycloalkyl groups [58]. Schiff bases are of great significance in coordination chemistry due to their applications in the medical and pharmaceutical fields. They are known to exhibit biological antifungal, antibacterial and antitumour activity [17-19]. Furthermore, Schiff bases are utilised as coordinating ligands, in electrochemistry and as catalysts, for example in the hydrogenation of olefins [59-62]. Their applications have been extended to ion-exchange, luminescence, magnetism and

in biological modelling [63]. Intramolecular hydrogen bonds between the oxygen and nitrogen atoms have been found to exist and play an important role in stabilising metal complexes [64].

Complexation of Schiff bases to metal ions has been performed to enhance the biological activity of some Schiff bases due to the synergistic effect [65,66]. A Schiff base ligand bis(*N*-salicylidene)-3-oxapentane-1,5-diamine (H_2L, Figure 5) has been prepared and coordinated to Sm(III), Eu(III) and Tb(III) to give complexes that bind to DNA *via* groove modes. In addition, evaluation of antioxidant activities of the compounds revealed that the complexes exhibit good antioxidant activities against the hydroxyl ($OH\cdot$) and the superoxide anion ($O_2^{-}\cdot$) radicals in *in vitro* studies. Coordination of the ligand to Sm(III) occurs in its dianionic form through all five donor sites to give a nine-coordinate $[Sm(L)(NO_3)(DMF)(H_2O)]$ complex with distorted tricapped trigonal prism shape [67].

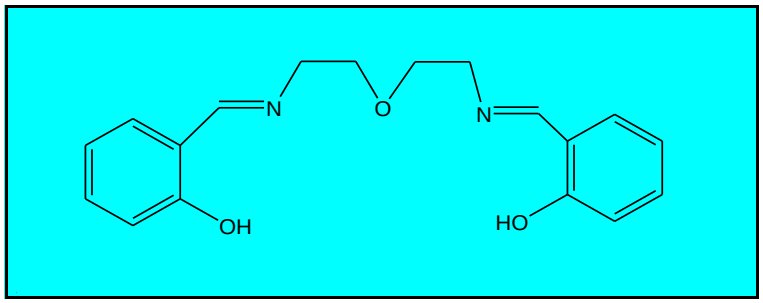

Figure 5: The structure of bis(*N*-salicylidene)-3-oxapentane-1,5-diamine.

Molecular nanomagnets that display slow magnetic relaxation are of considerable interest due to their potential applications in molecular-based magnetism [68]. Among the organic ligands employed in the construction of rare-earth molecular nanomagnets and metal-organic frameworks are pyridine-*N*-oxide-carbohydrazide Schiff base ligands [69]. The combination of pyridine-*N*-oxide (PNO) with hydrazide Schiff base skeletons enhances the coordination ability of the resulting ligands to the lanthanides, thereby changing the magnetic anisotropy of rare-earth ions. PNO groups can act as bridging ligands, thus leading to complexes with interesting topologies. An example of a PNO derivative is *N*'-(2-hydroxybenzylidene)pyridine-*N*-oxide-carbohydrazide (HL) which has been complexed to Dy(III) in the presence of triethylamine to yield

the dysprosium chain complex, $[Dy(L)(H_2O)_4]Cl_2 \cdot 2H_2O$. The Schiff base ligand acted in a tetradentate fashion, coordinating *via* one PNO oxygen atom, one carbonyl oxygen atom, one phenoxide oxygen atom and one imino nitrogen atom (Figure 6) [70].

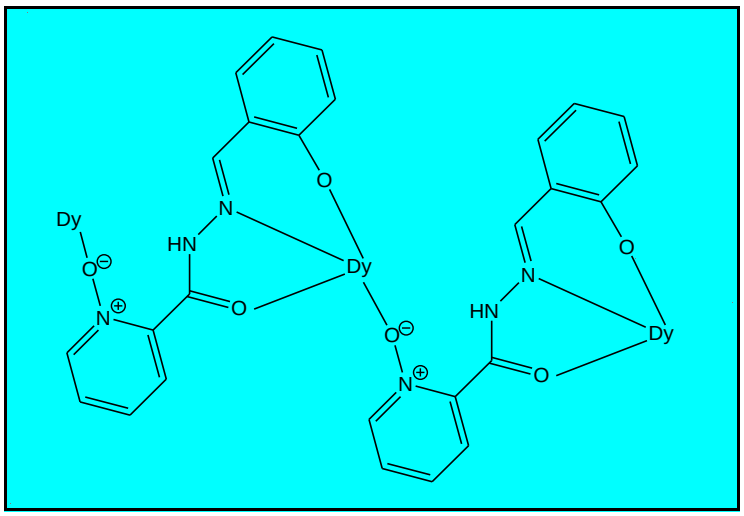

Figure 6: The coordination mode of the PNO derived Schiff base in $[Dy(L)(H_2O)_4]Cl_2 \cdot 2H_2O$.

1.2.9 Lanthanide and transition metal complexes with Thiosemicarbazones

Thiosemicarbazones (TSCs) are Lewis bases containing the thiosemicarbazide radical (= N-NH-C(S)-NH_2) [71]. TSCs are of increasing interest in chemistry due to their significant biological and pharmacological properties, such as antibacterial, antiviral, antineoplastic (antitumour) and antimalarial activities. Biological activities observed also include fungicidal and anti-inflammatory properties [71-73]. The derivatives and their metal complexes are also widely applied in many catalytic processes such as Suzuki-Miyaura cross-couplings, oxidation, hydrogenation and olefin cyclopropanations, as well as analytical reagents in the analysis of trace metals in pharmaceutical and biological samples [74].

The chemical nature of the moiety attached to the C=S carbon in the thiosemicarbazone derivative is responsible for various biological and medicinal

properties [73]. An example of an antibacterial TSC is *p*-acetamidobenzaldehyde thiosemicarbazone (commercially available as thiacetazone) (Figure 7) which has been widely used for the treatment of tuberculosis in Africa and South America [71]. However, the rise of multidrug resistance (MDR) in *Mycobacterium tuberculosis* (MTB) has made treatment difficult. Therefore, there is a need to develop new therapeutic drugs for the effective treatment of tuberculosis and to overcome MDR TB [75].

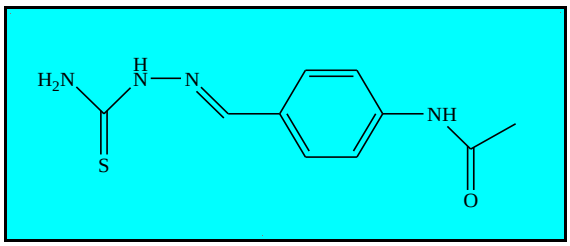

Figure 7: Structure of thiacetazone.

The therapeutic properties of thiosemicarbazones are partly due to their ability to chelate metal ions such as iron, thus depriving cells from essential nutrients and leading to cell death [74]. This feature makes these compounds powerful inhibitors of the iron-requiring enzyme ribonucleotide reductase, an enzyme which plays an essential role in DNA synthesis and repair [76,77].

Agarwal "*et al*" reported the ten-coordinate complex derived from 4[*N*(4´-nitrobenzalidene)amino] antipyrine thiosemicarbazone (4´-NO_2BAAPTS) and pyridine as a secondary ligand in which the metal is in the +3 oxidation state (Figure 8) [78].

Research on the biological properties of these compounds and their transition metal complexes revealed that the biologically active TSC molecules are planar and give rise to a tridentate system by acting as *N*,*N*,*S*- or *O*,*N*,*S*-donor ligands [15,71]. There is a wide variation in the bonding modes and stereochemistry with five-membered chelate rings formed from a *N*,*S*-bidentate system [79].

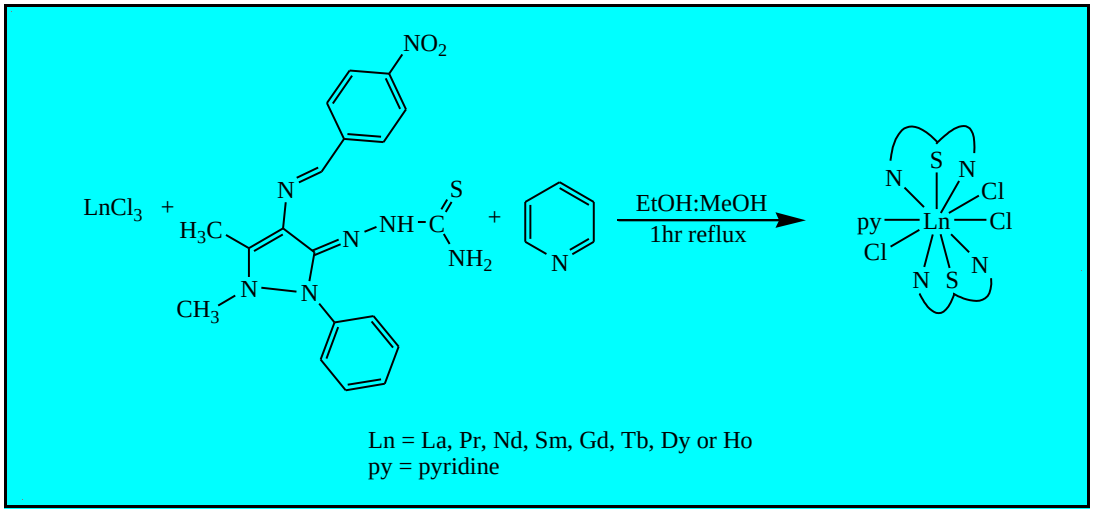

Figure 8: Ln(III) chloride reaction with 4´-NO_2BAAPTS and pyridine to give complexes with the general structure, [Ln(4´-NO_2BAAPTS)$_2$(py)Cl_3].

1.3 Applications of the Lanthanides

1.3.1 Luminescence

Lanthanide ions have long lifetimes and line-like emission bands in the visible region, thus imparting luminescence to the ions. The latter are thus commonly used as luminescent species in non-molecular solids [80]. These ions have a large number of electronic levels [14!/n!(14-n)!] (where n = number of *f* electrons) and are luminescent in the UV to the near-infrared (NIR) range. However, Lu^{3+} does not luminesce due to its completely filled sub-shell. The highly located excited states is the reason for the non-luminescence of Gd^{3+} [81-83].

A possible way to overcome the weak emissions of the Ln(III) ions is complexation of the metals to organic molecules. Excitation in the ligand region results in metal-centered luminescence, a process called the "antenna effect" or "sensitisation luminescence" [84]. The organic ligand absorbs energy and part of this energy is transferred to the metal ion excited states, thus giving intense luminescence of the ion. Therefore, addition of chelating agents or encapsulation of the lanthanide results in longer emission lifetimes and higher quantum yields [84,85].

The luminescent properties of the lanthanide ions make them very useful in biological systems. Their applications include the use as luminescent probes of biologically-relevant molecules and the monitoring of cellular functions *in vivo*, to the interpretation of structure and function of enzymes and proteins, and hence interest for medical analysis and diagnosis [49,85]. The emission of Tb(III) and Eu(III) ions in solution is enhanced through energy transfer by single-stranded oligonucleotides. These ions are able to bind to single-stranded DNA regions, making them ideal candidates for selective detection of base mismatches or mutations as well as investigating the interactions of DNA and RNA with drugs, enzymes and proteins [85].

1.3.2 Magnetic Resonance Imaging contrast agents

Even though the rare-earths are not biologically essential elements, they are biologically active and have important applications in medicine. Medical applications include the use in magnetic resonance imaging (MRI), a technique used for the monitoring of organ functions (Gd is currently the most useful in this regard) [28]. The first gadolinium based contrast agent was the nine-coordinate Gd(III)–DTPA complex (DTPA = diethylenetriamine pentaacetic acid) which was approved for clinical use in 1988 under the trademark Magnevist® (Figure 9) [86,87].

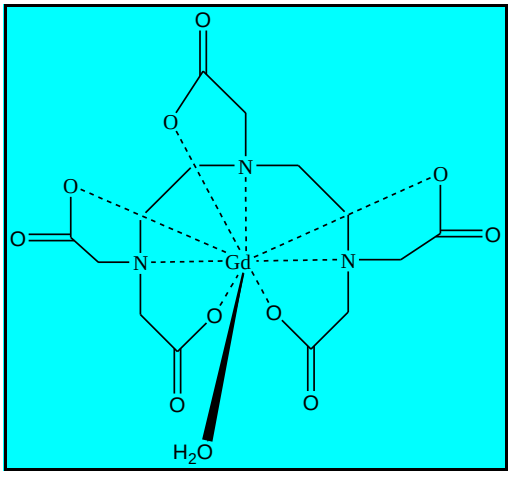

Figure 9: Structure of the nine-coordinate Gd(III)–DTPA complex, Magnevist®.

For MRI, it is ensured that the lanthanide is in a form where it may be easily excreted from the body to overcome toxicity. The lanthanide must also have strong coordination with the ligand so that insignificant amounts of the aqua ion may be released [28]. The advantage of MRI in medicinal diagnostics as an imaging technique over radio-diagnostic methods such as X-ray Computer Tomography or Positron Emission Tomography is that there is no use of harmful high-energy radiation [88].

What makes the Gd(III) ion a highly effective and easily traceable MRI contrast agent is the high magnetic moment (7.9 BM) resulting from seven unpaired *f*-electrons as well as a totally symmetric electronic state ($^8S_{7/2}$ ground state), which gives longer electronic relaxation times (10^{-8} – 10^{-9} s) than other Ln(III) ions [87,89]. For clinical utilisation, Gd(III) must be coordinated in a highly stable complex and exhibit a long-term resistance to a transmetallation or transchelation loss of the Gd(III) ion. This is a way of preventing significant toxicity of the aqua-ion (free form). An example of a contrast agent based on Gd(III) is the Gd–DOTA complex (DOTA = 1,4,7,10-tetraazacyclododecane-1,4,7,10-tetraacetic acid), marketed as Dotarem® by Guerbet (Figure 10) [87,90].

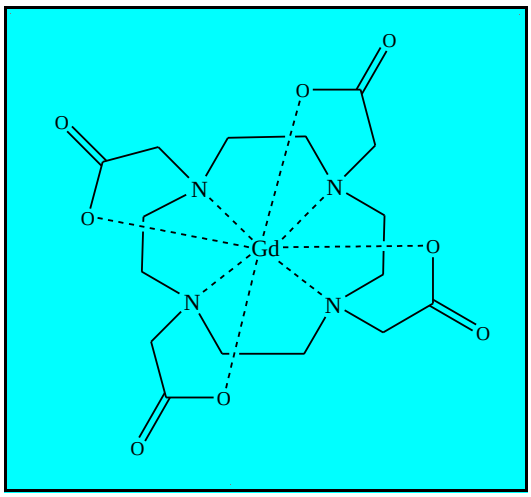

Figure 10: The eight coordinate Gd–DOTA complex, Dotarem®.

1.3.3 Catalysis

When in the form of coordination complexes, stable 4*f* configurations of the lanthanides exist in the +3, +4 (Ce, Tb) or +2 (Eu, Yb) oxidation states. These forms are strongly electropositive, thus making these ions hard Lewis acids with a strong affinity for oxygen-donor ligands. With the exception of SmI_2 and Ce(IV) salts, the metals are not utilised in redox chemistry due to the stability of these oxidation states [25,26,34,91].

Lanthanide complexes typically have little or no covalent character due to the nature of the 4*f* orbitals. These orbitals are buried inside the atom and are shielded from the atom's environment by the 4*d* and 5*p* electrons, and thus little effective overlap exists between the metal's orbitals and the binding ligand [25,34]. Therefore, complexes are held together by weaker electrostatic forces. As a result, the complex is not confined to a single geometry, enabling rapid intramolecular and intermolecular ligand exchange to occur [26,34,92].

These unique electronic features enable these metals to occupy an important position amongst catalysts in organic synthesis and therefore are widely used in industry. Previous research revealed that some trivalent lanthanide complexes are utilised in various transformations involving unsaturated substrates, such as hydroamination, hydrosilylation, polymerisation, hydrogenation, hydrophosphination, hydroboration, hydrothiolation and hydroalkoxylation [92-96]. Hard Lewis acids can polarise bonds on coordination and this modifies the electrophilicity of compounds, thus coordination compounds can bind and dissociate rapidly. This results in very high turnover rates, which leads to excellent yields [92].

An example of the catalytic activity of rare-earths is illustrated by the hydrophosphination reaction in Figure 11. Ytterbium(II) complexes catalyse the hydrophosphination reaction between styrene and Ph_2PH or $PhPH_2$. This reaction is regioselective, giving exclusively the anti-Markovnikov monoaddition product [92].

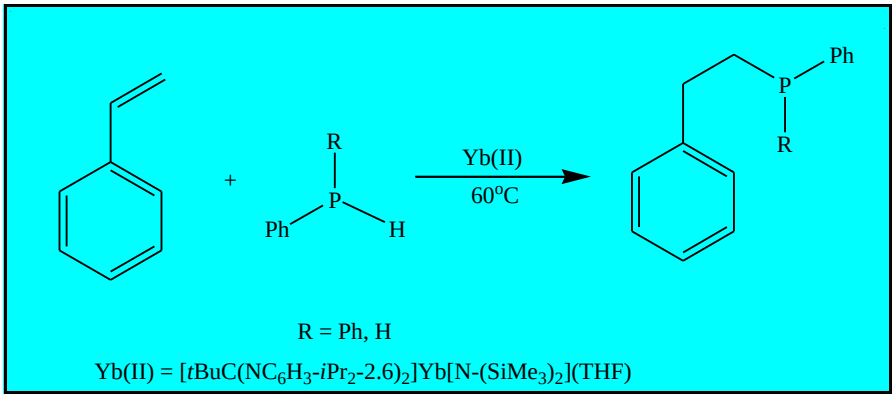

Figure 11: Hydrophosphination reaction catalysed by Yb(II) complexes.

1.3.4 NMR lanthanide shift reagents

Paramagnetic ions of cobalt and nickel were first applied as NMR shift reagents. However, severe line broadening was a big drawback in their use. It was in 1969 when Hinckley discovered the use of paramagnetic lanthanide ions without significant line broadening [97]. The observed NMR shifts occurred through interactions between the nuclear spins and the spin of the unpaired electrons of the paramagnetic Ln ions. Even though through-bond Fermi contact interactions contribute in some cases to shifts, action of shift reagents is mainly ascribed to through-space dipolar interactions. Proton shifts can be negative or positive, and are reliant on the sign of the $(3\cos^2\theta - 1)$ term, where θ is the angle made by the radius (r) vector from the metal atom to the resonating nucleus with the principal axis [98,99].

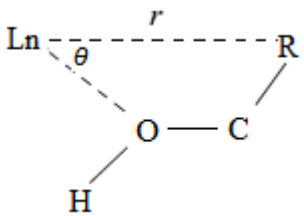

Paramagnetic lanthanide ions are applied in this regard since they simplify complicated spectra by allowing separation of overlapping signals, and enable integration of signals which are expected to be overlapped. An example of a shift reagent that was discovered to be efficient in causing isotropic shifts in functional

organic molecules such as ketones, esters, amines and alcohols is the complex, tris(dipivaloylmethanato)europium(III), $Eu(dpm)_3$ [99].

Lanthanide complexes are also applied as optically active NMR shift reagents for the direct determination of enantiomeric compositions. Examples are tris(3-heptafluorobutyryl-d-camphorato)praseodymium(III), $Pr(hfbc)_3$, tris(3-trifluoroacetyl-d-camphorato)praseodymium(III), $Pr(facam)_3$, and the corresponding europium analogs, $Eu(hfbc)_3$ and $Eu(facam)_3$. Enantiomers that respond to lanthanide NMR shift reagents normally show nonequivalence in NMR spectra in the presence of these optically active chelates that exhibit very good solubility in nonpolar solvents. These *β*-diketone chelates have been successfully used to induce significant downfield shifts in the NMR spectra of 2-butanol and 2-phenyl-2-butanol [100,101].

1.3.5 Biological activity

Lanthanide ions have similar ionic radii to calcium and tend to have a strong affinity for Ca^{2+} ion binding sites on biological molecules such as proteins. This makes it possible for Ln^{3+} ions to act as either Ca^{2+} inhibitors or probes of calcium sites [28,102]. For example, Ln^{3+} ions are useful as biochemical probes to investigate calcium transport in mitochondria, even though Ln^{3+} is unable to gain entry into intracellular organelles. They achieve this purpose by acting on the exterior face of the calcium channel [103].

Since lanthanides have a higher charge, they can replace Ca^{2+} in bone, a property exploited in the treatment of hypophosphatemia. Fosrenol, $[La_2(CO_3)_3]$, is the therapeutic agent employed for this overload illness that arises in patients with renal disease [28]. The fact that Ln(III) compounds do not cross the intestinal membranes enable their utility in the treatment of this illness. $La_2(CO_3)_3$ dissolves in stomach acid to release species that bind with PO_4^{3-}. As a result, excess La(III) and insoluble $LaPO_4$ are excreted efficiently [28,104].

1.3.6 Therapeutic applications

A few radioactive lanthanide complexes have been applied successfully in the diagnosis and treatment of cancer. However, a number of these lanthanide-based anti-cancer agents needed high doses and this resulted in significant toxicity [105,106]. Research showed that Ln^{3+} induces transformation of malignant tumours *in vitro*. For example, it has been shown that La^{3+} and Tb^{3+} enhance malignant transformation of tetradecanoylphorbol acetate (TPA)-sensitive as well as TPA-resistant preneoplastic mouse JB6 epidermal cells [107]. Coumarins and their complexes with La^{3+}, Ce^{3+} and Nd^{3+} were found to show activity against various cancer cell lines [11,108].

1.3.7 Other uses

Coordination polymers of rare-earth complexes are of great impotance in high technology devices because of their remarkable and unique optical and magnetic properties. These are utilised in applications such as hard-disk drives, telecommunications, security inks and counterfeiting tags, optical glasses and lasers, lighting and displays and biosciences [30]. Fluorescence and phosphorescence of Gd(III) and Lu(III) porphyrins suggested the utilisation of these complexes in the intraratiometric luminescence intensity-based oxygen sensing [109]. There is an increasing use of Lu(III) compounds, such as lutetium texaphyrin, as photosensitisers in photodynamic therapy and photoangioplasty [110]. Some lutetium compounds are used as deoxidisers in stainless steel production, in rechargeable batteries and in superconductors.

Even though the lanthanides are biologically non-essential elements, they have been found recently to produce beneficial effects in plants or microalgae by alleviating the effects of metal ion deficiency [111]. These metals have proved useful in the metallurgical industry in chemical alloying to improve the properties of Mg alloys. It has been shown that addition of La, Ce or Gd led to an increase in strength of Mg alloys, as well as reduction in the texture strength of the basal plane, thus leading to improved ductility of Mg alloys [112]. The reduction in the texture strength has also

increased the formability of Mg sheets and improved the mechanical properties of Mg alloys [112-114]. Alloying with the Lns has been reported to improve creep resistance and corrosion resistance [115,116].

1.4 References

[1] J.A. Lybarger, R.F. Spengler and C.T. DeRosa, *Agency for Toxic Substances and Disease Registry*, (1993), p. 61.

[2] S.H. van Rijt and P.J. Sadler, *Drug Discovery Today*, **14** (2009) 23-24.

[3] R.J. Palmer, J.L. Butenhoff and J.B. Stevens, *Environ Res.*, **43** (1987**)** 142.

[4] T.L. Fuller and R.G. Canada, *Cancer Chemother. Pharmacol.*, **44** (1999) 249.

[5] S.C. Srivastava, Criteria for the selection of radionuclides for targeting nuclear antigens for cancer radioimmunotherapy. *Cancer Biother. Radiopharm.*, **11** (1996) 43–44.

[6] H. Chong, D.E. Milenic, K. Garmestani, E.D. Brady, H. Arora, C. Pfiester and M.W. Brechbiel, *Nucl. Med. and Biol.*, **33** (2006) 459.

[7] D. Nayak and S. Lahiri, *J. Radioanalyt. and Nucl. Chem.*, **242:2** (1999) 425-428.

[8] D.V. Rao, P.N. Goodwin and F.L. Khalil, *J. Nucl. Med.*, **15** (1974) 1008.

[9] V.W. Yam and K.K. Lo, *Coord. Chem. Rev.*, **184** (1999) 158.

[10] S.H. van Rijt and P.J. Sadler, *Drug Discovery Today*, **14** (2009) 1089.

[11] I. Kostova, *Curr. Med. Chem. – Anti-Cancer Agents*, **5** (2005) 591.

[12] I. Kostova, N. Trendafilova and G. Momekov, *Journal of Trace Elements in Medicine and Biology*, **22** (2008) 100-111.

[13] A. Chaubey and S.N. Pandeya, *Asian J. Pharm. Clin. Res.*, **4:**4 (2011) 5-6.

[14] K.A. Ali, M.M. Abd-Elzaher and K. Mahmoud, *Int. J. Med. Chem.*, **2013** (2013) 1.

[15] N.C. Kasuga, K. Sekino, C. Koumo, N. Shimada, M. Ishikawa and K. Nomiya, *J. Inorg. Biochem.*, **84** (2001) 55-65.

[16] N.C. Kasuga, K. Sekino, M. Ishikawa, A. Honda, M. Yokoyama, S. Nakano, N. Shimada, C. Koumo and K. Nomiya, *J. Inorg. Biochem.*, **96** (2003) 298.

[17] A.A.A. Abu-Hussen, *J. Coord. Chem.*, **59** (2006) 157.

[18] M.S. Karthikeyan, D.J. Parsad, B. Poojary, K.S. Bhat, B.S. Holla and N.S. Kumari, *Bioorg. Med. Chem.*, **14** (2006) 7482.

[19] P. Panneerselvam, R.R. Nair, G. Vijayalakshmi, E.H. Subramanian and S.K. Sridhar, *Eur. J. Med. Chem.*, **40** (2005) 225.

[20] D. Sriram, P. Yogeeswari, R. Thirumurugan and R.K. Pavana. Discovery of new antitubercular oxazolyl thiosemicarbazones, *J. Med. Chem.*, **49** (2006) 3448-3449.

[21] M.D. Mashkovskii, *Lekarstvennye sredstva* (Drugs), Moscow: Novaya Volna, 2008.

[22] G. Pelosi, *The Open Crystallography Journal*, **3** (2010) 16.

[23] R.A. Finch, M. Liu, S.P. Grill, W.C. Rose, R. Loomis, K.M. Vasquez, Y. Cheng and A.C. Sartorelli, *Biochem. Pharm.*, **59** (2000) 983.

[24] T. Moeller, *The Chemistry of the Lanthanides*, **26** (1973) 10.

[25] S. Cotton (1991) – *Lanthanides and Actinides*. MacMillan Education Ltd, London.

[26] J.C. Bailar (1973) – *Comprehensive Inorganic Chemistry – Lanthanides and Transition Metal Compounds*, **Vol 4**. Pergamon Press, London.

[27] S. Cotton, *Lanthanide and Actinide Chemistry*, John Wiley & Sons: West Sussex, 2006, 35-56.

[28] S.A. Cotton and J.M. Harrowfield, *Lanthanides: Biological Activity and Medical Applications,* (2012).

[29] R.C. Mehrotra, P.N. Kapoor and J.M. Batwara, *Coord. Chem. Rev.*, **31** (1980) 67.

[30] J.-C.G. Bunzli, *J. Coord. Chem.*, **67** (2014) Nos. 23-24, 3706.

[31] T. Akaska, Z. Bian, K.W. Chan, Z. Chen, S. Gao, H. Hu, C. Huang, J. Jiang, S. Jiang, F. Li, X. Lu, Y. Lu, S. Nagase, Q. Shen, B. Wang, E. Wand, K. Wang, R. Wang, X. Wang, W. Wong, H. Xu, H. Yang, Y. Yao, X. Zhang and Z. Zheng. *Rare-Earth Metal Coordination Chemistry. Fundamentals and Applications*; John Wiley & Sons: Singapore, (2010) 6.

[32] C.H. Evans, *Trends in Biochemical Sciences*, **1976** (1983) 1–5.

[33] L. Armelao, S. Quici, F. Barigelletti, G. Accorsi, G. Bottaro, M. Cavazzini and E. Tondello, *Coord. Chem. Rev.*, **254** (2010) 487-489.

[34] C. Huang (2010) – *Rare-Earth Coordination Chemistry – Fundamentals and Applications*. John Wiley & Sons, Asia. pp1-39.

[35] G.W. Beall, W.O. Milligan and H.A. Wolcott, *J. Inorg. Nucl. Chem.,* **39** (1977) 65.

[36] P.B. Hitchcock, M.F. Lappert, R.G. Smith, R.A. Bartlett and P.P. Power, *J. Chem. Soc., Chem. Commun.*, (1988) 1007.

[37] A. Ruiz-Martinez and S. Alvarez, *Chem. Eur. J.,* **15** (2009) 7470.

[38] S.A. Cotton, *C. R. Chimie*, **8** (2005) 129–130.

[39] P.A. Cox (2004) – *Inorganic Chemistry 2nd Ed*. BIOS Publishers, U.K.

[40] N.N. Greenwood and A. Earnshaw (1984) – *Chemistry of the Elements*. Pergamon Press, U.K.

[41] F.A. Hart, M.B. Hursthouse, K.M.A. Malik and S. Moorhouse, *J. Chem. Soc., Chem. Commun.*, (1978) 549.

[42] P. Di Bernardo, A. Melchior, M. Tolazzi and P. Luigi Zanonato, *Coord. Chem. Rev.* **256** (2012) 328.

[43] D.F. Shriver and P.W. Atkins (1999) – *Inorganic Chemistry, 3rd Ed*. Oxford University Press, U.K.

[44] S.P. Fricker, *Chem. Soc. Rev.*, **35** (2006) 524.

[45] J.D. Lee (1991) – *Concise Inorganic Chemistry*, Chapman & Hall, London.

[46] A. de Bettencourt-Dias, P.S. Barber and S.A. Bauer, *J. Am. Chem. Soc.*, **134** (2012) 6987.

[47] J.-C.G. Bunzli, B. Klein, G. Chapuis and K.J. Schenk, *Inorg. Chem.,* **21** (1982) 808-809.

[48] J.W. O'Laughlin, *Handbook on the Physics and Chemistry of Rare-Earths*; K.A. Gschneidner, Jr., E. LeRoy, Eds.; *Elsevier,* **4** (1979) 341.

[49] J.-C.G. Bunzli, In *Rare-Earths*, (R. Saez Puche and P. Caro, eds.), Editorial Complutense, Madrid, (1998) 223.

[50] C. Brouca-Cabarrecq, J. Dexpert-Ghys, A. Fernandes, J. Jaud and J.C. Trombe, *Inorg. Chim. Acta*, **361** (2008) 2909.

[51] T.K. Prasad, S. Sailaja and M.V. Rajasekharan, *Polyhedron*, **24** (2005) 1487.

[52] T.K. Prasad and M.V. Rajasekharan, *Polyhedron*, **26** (2007) 1364.

[53] L. Ma, O.R. Evans, B.M. Foxman and W. Lin, *Inorg. Chem.*, **38** (1999) 5837.

[54] R. Murugavel, K. Baheti and G. Anantharaman, *Inorg. Chem.*, **40** (2001) 6870.

[55] C.K. Schaver and O.P. Anderson, *J. Chem. Soc., Dalton Trans.*, (1989) 185.

[56] G.A. van Albada, S. Gorter and J. Reedijk, *Polyhedron*, **18** (1999) 1821.

[57] B.-L. An, M.-L. Gong, M.-X. Li and J.-M. Zhang, *J. Mol. Struct.*, **687** (2004) 1-4.

[58] Z. Hussain, E. Yousif, A. Ahmed and A. Altaie, *Org. and Med. Chem. Lett.*, **4** (2014) 1.

[59] S. Naiya, H.-S. Wang, M.G.B. Drew, Y. Song and A. Ghosh, *Dalton Trans.*, **40** (2011) 2744.

[60] M.A. Neelakantan, M. Esakkiammal, S.S. Mariappan, J. Dharmaraja and T. Jeyakumar, *Indian J. Pharm. Sci*., **72** (2010) 216.

[61] K.C. Gupta and A.K. Sutar, *Coord. Chem. Rev*., **252** (2008) 1420–1421.

[62] G. Kenneth, K.B. Jean and A.H. Lisa, *Polyhedron*, **8** (1989) 113.

[63] M.M.H. Khalil, M.M. Aboaly and R.M. Ramadan, *Spectrochim. Acta*, **61** (2005) 157.

[64] Y. Elerman, M. Kabak and A. Elmali, *Z. Naturforsch*. **B 57** (2002) 651.

[65] X. Wang, Y. Du, L. Fan, H. Liu and Y. Hu, *Poly. Bull.*, **55** (2005) 105.

[66] E. Canpolat and M. Kaya, *J. Coord. Chem*. **57** (2004) 1217.

[67] H. Wu, G. Pan, Y. Bai, Y. Zhang, H. Wang, F. Shi, X. Wang and J. Kong, J. Photochem. and Photobio. B: Biology, **135** (2014) 33-35.

[68] D.N. Woodruff, R.E.P. Winpenny and R.A. Layfield, *Chem. Rev.*, 113 (2013) 5110.

[69] H.L. Sun, X.L. Wang, L. Jia, W. Cao, K.Z. Wang and M. Du, *Cryst. Eng. Comm.*, **14** (2012) 512.

[70] Q. Chen, Y.-S. Meng, Y.-Q. Zhang, S.-D. Jiang, H.-L. Sun and S. Gao, *Chem. Comm.*, **50** (2014) 10434.

[71] M.A. Affan, M.A. Salam, F.B. Ahmad, J. Ismail, M.B. Shamsuddin and H.M. Ali, *Inorg. Chim. Acta*, **366** (2001) 227-228.

[72] R.K. Agarwal, L. Singh and D.K. Sharma, *Bioinorg. Chem. and Appl.*, (2005) 1-3.

[73] N.C. Saha, R. Pradhan, M. Das, N. Khatun, D. Mitra, A. Samanta, A.M.Z. Slawin, A.D. Jana, J. Klanke and E. Rentschler, *J. Coord. Chem.*, **67** (2014) 286-287.

[74] M. Bakir, R. Conry and D. Thomas, *J. Coord. Chem.*, **2** (2014).

[75] F.R. Pavan, P.I. da S. Maia, S.R.A. Leite, V.M. Deflon, A.A. Batista, D.N. Sato, S.G. Franzblan and C.Q.F. Leite, *Eur. J. Med. Chem.*, **45** (2010) 1898.

[76] T. Rosu, E. Pahontu, S. Pasculescu, R. Georgescu, N. Stanica, A. Curaj, A. Popescu and M. Leabu, *Eur. J. Med. Chem*., **45** (2010) 1627.

[77] E.A. Enyedy, M.F. Primik, C.R. Kowol, V.B. Arion, T. Kiss and B.K. Keppler, *Dalton Trans.*, **40** (2011) 5895.

[78] R.K. Agarwal, A.A. Khan, P. Singh and V. Kumar, *J. Appl. Chem. Res.*, **11** (2009) 62-63.

[79] F. Zunino, G. Savi and A. Pasini, *Cancer Chemoth. Pharm.*, **18** (1986) 180.

[80] N. Sabbatini, M. Guardigli, I. Manet, R. Ungaro, A. Casnati, R. Ziessel, G. Ulrich, Z. Asfari and J-M. Lehn, *Pure & Appl. Chem.*, **67** (1995) 135-136.

[81] R. Lyszczek and L. Mazur, *Polyhedron*, **41** (2012) 7.

[82] S.V. Eliseeva and J.-C.G. Bunzli, *Chem. Soc. Rev.*, **39** (2010) 189.

[83] G. de Oliveira, A. Machado, G.W. Gomes, J.H.S.K. Monteiro, M.R. Davolos, U. Abram and A. Jagst, *Polyhedron*, **30** (2011) 851.

[84] T.V. Balashova, A.P. Pushkarev, V.A. Ilichev, M.A. Lopatin, M.A. Katkova, E.V. Baranov, G.K. Fukin and M.N. Bochkarev, *Polyhedron*, **50** (2013) 112-113.

[85] C. Turro, P.K.-L. Fu and P.M. Bradley, *Lanthanide Ions as Luminescent Probes of Proteins and Nucleic Acids*, Columbus, USA.

[86] H.J. Weinmann, R.C. Brasch, W.R Press and G.E. Wesbey, *Am. J. Roentgenol.*, **142** (1984) 619-624.

[87] P. Hermann, J. Kotek, V. Kubicek and I. Lukes, *Dalton Trans.*, (2008) 3027–3028.

[88] S. Ogawa, T.M. Lee, A.S. Nayak and P. Glynn, *Magn. Reson. Med*., **14** (1990) 68.

[89] M.T. Vlaardingerbroek, and J.A. den Boer, *Magnetic Resonance Imaging. Theory and Practice*, Springer Verlag, (Germany), 1996.

[90] W.P. Cacheris, S.C. Quay and S.M. Rocklage, *Magnetic Resonance Imaging*, **8** (1990) 467.

[91] L. Li, F. Yuan, T. Li, Y. Zhou and M. Zhang, *Inorg. Chim. Acta*, **397** (2013) 69.

[92] I.V. Basalov, S.C. Rosca, D.M. Lyubov, A.N. Selikhov, G.K. Fukin, Y. Sarazin, J-F. Carpentier and A.A. Trifonov, *Inorg. Chem.*, **53** (2014) 1654-1655.

[93] Z. Hou and Y. Wakatsuki, *Coord. Chem. Rev.*, **231** (2002) 1−2.

[94] G. Jeske, H. Lauke, H. Mauermann, P.N. Swepston, H. Schumann and T. Marks, *J. Am. Chem. Soc.*, **107** (1985) 8091.

[95] G. A. Molander and J. A. Romero, *Chem. Rev.*, **102** (2002) 2161−2162.

[96] C. J. Weiss and T. J. Marks, *Dalton Trans.*, **39** (2010) 6576.

[97] C. C. Hinckley, *J. Amer. Chem. Soc.*, **91** (1969) 5160.

[98] A.F. Cockerill, G.L.O. Davies, R.C. Harden and D.M. Rackham, *Chem. Rev.*, **73** (1973).

[99] W.D. Horrocks and J.P. Sipe, *J. Am. Chem. Soc.*, **93** (1971).

[100] H.L. Goering, J.N. Eikenberry, G.S. Koermer and C.J. Lattimer, *J. Am. Chem. Soc.*, **96** (1974).

[101] L.M. Sweeting, D.C. Crans and G.M. Whitesides, *J. Org. Chem.*, **52** (1987).

[102] S.P. Fricker. The therapeutic applications of lanthanides, *Chem. Soc. Rev.*, 2006**.**

[103] E.W. Yeung, S.I. Head and D.G. Allen, *J. Physiol*., **552** (2003) 449.

[104] E. Pidcock and G. R. Moore, *J. Biol. Inorg. Chem.*, **6** (2001) 479.

[105] R. Lewin, K. G. Stern, D. M. Ekstein, L. Woidowsky and D. Laszlo, *J. Natl. Cancer Inst.*, **14** (1953) 45.

[106] J. Luo, *J. Bethune Medical Univ.*, **17** (1991) 137.

[107] B. M. Smith, T. D. Gindhart, and N.H. Colburn, *Carcinogenesis (London)*, **7** (1986) 1949.

[108] I. Manolov, I. Kostova, T. Netzeva, S. Konstantinov and M. Karaivanova, *Arch Pharm. (Weinheim)*, **333** (2000) 93.

[109] B. Kalota and M. Tsvirko, *Chem. Phys. Lett.*, **634** (2015) 188-189.

[110] R. Zare-Dorabei, M.R. Ganjali, H.R. Rahimi, H. Farahani and P. Norouzi, *Curr. Chem. Lett.*, **2** (2013) 125.

[111] F. Goecke, C.G. Jerez, V. Zachleder, F.L. Figueroa, K. Bisova, T. Rezanka and M. Vitova, *Frontiers in Microbiology*, **6** (2015) Article 2 .

[112] E. Ayman, U. Junko and K. Katsuyoshi, *Acta Materialia*, **59** (2011) 273-274.

[113] I.A. Anyanwu, Y. Gokan, A. Suzuki, S. Kamado, Y. Kojima, S. Takeda S, et al. *Mater. Sci. Eng.*, **380** (2004) 93.

[114] N. Balasubramani, M. Suresh, A. Srinivasan, U.T.S. Pillai and B.C. Pai, *J. Mater. Sci.*, **42** (2007) 8374.

[115] T. Takenaka, T. Ono, Y. Narazaki, Y. Naka and M. Kawakami, *Electrochim Acta*, **53** (2007) 117.

[116] W. Liu, F. Cao, L. Chang, Z. Zhang and J. Zhang, *Corrosion Sci.*, **51** (2009) 1334.

CHAPTER 2

Experimental

2.1 Chemicals

The lanthanide salts and organic compounds were sourced from the chemical companies listed in Tables 1 and 2 below, in the given purities and used without further purification.

Table 1: Lanthanide salts used in the study.

	Company	**Purity (%)**
$La(NO_3)_3 \cdot 6H_2O$	Sigma Aldrich	≥99.0
$Ce(NO_3)_3 \cdot 6H_2O$	Sigma Aldrich	99.9
$Pr(NO_3)_3 \cdot 6H_2O$	Sigma Aldrich	99.9
$PrCl_3 \cdot 6H_2O$	Sigma Aldrich	99.9
$Nd(NO_3)_3 \cdot 6H_2O$	Sigma Aldrich	99.9
$SmCl_3 \cdot 6H_2O$	Sigma Aldrich	≥99.0
$Gd(NO_3)_3 \cdot 6H_2O$	Sigma Aldrich	99.9
$Tb(NO_3)_3 \cdot 5H_2O$	Sigma Aldrich	99.9
$Ho(NO_3)_3 \cdot 6H_2O$	Sigma Aldrich	99.9
$Er(NO_3)_3 \cdot 6H_2O$	Sigma Aldrich	99.9

Potassium hydroxide (≥85% purity) and hydrazine hydrate (≥98.0% purity) used in the synthesis of *S*-methyldithiocarbazate were sourced from Merck and used as supplied. The solvents used (methanol, ethanol, acetone, acetonitrile and diethyl

ether) were obtained from Merck and DMF from BDH Laboratory supplies. Analytical grade solvents were dried over 3 Å molecular sieves prior to use.

Deuterated DMSO used for ^{1}H and ^{13}C NMR spectroscopy was purchased from Merck.

Table 2: Organic compounds used.

	Supplier	**Purity (%)**
2,6-pyridinedimethanol	Sigma Aldrich	98.0
o-vanillin	Sigma Aldrich	99.0
2-amino-2-methyl-1-propanol	Sigma Aldrich	≥95
Carbon disulfide	Sigma Aldrich	≥99.0
Methyl iodide	Sigma Aldrich	≥99.0
Salicylaldehyde	Sigma Aldrich	98.0
Diethylamine	Sigma Aldrich	≥99.5
4-(4-bromophenyl)-3-thiosemicarbazide	Fluorochem	-

2.2 Instrumentation

The melting points of organic compounds and complexes were determined using a Stuart® Melting Point Apparatus SMP30, measuring and recording the temperatures of crystalline samples held within capillary tubes.

The micro-analyses for carbon, hydrogen, nitrogen and sulfur were carried out using a Vario Elementary ELIII Microcube CHNS analyser.

Conductivity measurements were performed at room temperature using HANNA instruments (HI) 2300 EC/TDS/NaCl Meter.

The UV-Vis spectra were carried out on a PerkinElmer Lambda 35 UV/Vis spectrophotometer, and processing done using *UV WinLab* software.

The thermogravimetry (TG), differential scanning calorimetry (DSC) and derivative thermogravimetry (DTG) were carried out at a heating rate of 10 °C/min under nitrogen on a TA 2050 Thermogravimetric Analyser.

NMR spectra were recorded at room temperature using a Bruker AvanceIII 400 Nuclear Magnetic Resonance (NMR) Spectrometer and acquisition done using *TopSpin 3.0* software. Analysis of spectra was performed using *ACD/Labs* software.

The infrared spectra were obtained from a Bruker Tensor 27 FT-IR spectrophotometer, equipped with the Platinum ATR attachment. The samples were run neat on ATR and the recorded data was analysed using the *OPUS 6.5* software.

A Bruker Kappa Apex II X-ray Crystallography System was used for single crystal diffractometry at 200 K, using graphite monochromated Mo Kα radiation (λ = 0.71073 or 0.71069 Å). *APEX2* was used for data collection and *SAINT* software for data reduction and cell refinement [6]. The crystal structures were solved and refined with *SHELXS97* and *SHELXL97*, respectively [7,8]. Molecular graphics were obtained using *ORTEPIII* and *Mercury* software [9,10].

Lanthanide geometry analyses were performed by SHAPE 2.1 software. This program is based on the algorithm defined by Pinsky and Avnir for the calculation of continuous shape measures (CShM values) [11].

Electrochemical analyses were done using C3 Cell Stand for Bas Epsilon Version 1.30.64 system which consists of three electrodes: a platinum working electrode, a platinum auxiliary electrode and a pseudo silver/silver chloride Re-5 reference electrode. The redox behaviour of the lanthanide complexes was investigated using 0.10 M tetrabutylammonium perchlorate (TBAP) as supporting electrolyte. The oxygen in sample solutions was removed by aerating with nitrogen for 10 minutes before runs.

2.3 Synthesis of the ligands

2.3.1 Synthesis of 2-((*E*)-(1-hydroxy-2-methylpropan-2-ylimino)methyl)-6-methoxyphenol (H_2L_1)

The Schiff base ligand H_2L_1 (Figure 1) was prepared using the procedure described for related compounds [1-3]. H_2L_1 was synthesised by stirring a solution of *o*-vanillin (6.09 g, 40.0 mmol) and 2-amino-2-methyl-1-propanol (3.57 g, 40.0 mmol) in 30 mL methanol at reflux temperature for 2 hours. The resulting yellow solution was concentrated using a rotary evaporator. The yellow precipitate produced was filtered off, dried and used without further purification. Yield: 64.3%, m.p. = 117.2-119.5 ^{o}C. Anal. Calcd. for $C_{12}H_{17}NO_3$ (%): C, 64.56; H, 7.67; N, 6.27. Found: C, 64.13; H, 7.89; N, 6.26. UV-Vis (DMF, λ_{max} nm (ε, $M^{-1}cm^{-1}$)): 329 (26560), 420 (9170). IR (cm^{-1}): *v*(OH) 3675-3149(b), *v*(C-H) 3034-2805(m), *v*(C=N) 1635(s), *v*(C-N) 1229(s), *v*(C-O) 1170(s). ^{1}H NMR (DMSO-d_6, δ ppm): 8.20 (s, 1H, -CH=N-), 6.74 (d, 2H, Ar), 6.58 (t, 1H, Ar), 3.78 (s, 3H, -OCH_3), 3.51 (s, 1H, phenolic -OH), 3.37 (s, 2H, -CH_2-), 2.08 (s, 1H, alkyl -OH), 1.26 (s, 6H, -CH_3).

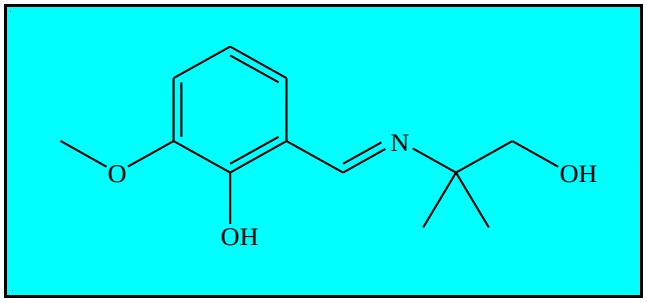

Figure 1: The structure of H_2L_1.

2.3.2 Synthesis of salicylaldehyde-*N*(4)-diethylthiosemicarbazone (H_2L_2)

The synthesis of H_2L_2 started with the preparation of *S*-methyldithiocarbazate [4]. Potassium hydroxide (22.80 g, 0.4000 mol) was dissolved in 90% ethanol (114 mL) and the solution was cooled in ice. Hydrazine hydrate (20.00 g, 0.4000 mol) was then added slowly with stirring to the above solution, followed by the dropwise addition of carbon disulfide (30.40 g, 0.4000 mol) with vigorous stirring. The temperature of the reaction mixture was kept below 6 ^oC during the addition of carbon disulfide. The resulting yellow oil was separated and dissolved in 40% ethanol (40 mL) and the solution cooled in ice. Methyl iodide (58.00 g, 0.4000 mol) was then slowly added with vigorous stirring. The white product formed was washed with water and dried in air. Recrystallisation of the crude *S*-methyldithiocarbazate was performed using ethanol. Yield = 35.5%; m.p = 80.2–81.5 ^oC.

H_2L_2 (Figure 2) was synthesised following the literature procedure [5]. An equimolar mixture of *S*-methyldithiocarbazate and salicylaldehyde were refluxed in dry ethanol for 24 hours. This conversion of salicylaldehyde into its *S*-methyldithiocarbazate derivative was followed by transamination of the derivative with diethylamine. H_2L_2 was obtained as an orange solid after recrystallisation from ethanol. Yield = 55.8%, m.p = 102.5-104.4 ^oC. Anal. Calcd for $C_{12}H_{17}N_3OS$ (%): C, 57.29; H, 6.76; N, 16.71; S, 12.73. Found: C, 57.33; H, 6.42; N, 16.73; S, 12.66. IR (cm^{-1}): *ν*(NH) 3114(m), *ν*(CH=N) 1604(s), *ν*(C=S) 760(s). ^1H NMR (DMSO-d_6, δ ppm): 11.74 (s, 1H, -NH), 11.11 (s, 1H, salicylaldehyde C-H), 8.55 (s, 1H, -OH), 7.74 (d, 1H, Ar), 7.68 (t, 1H, Ar), 7.37 (t, 2H, Ar), 4.34 (q, 4H, $-CH_2-$), 1.19 (t, 6H, $-CH_3$).

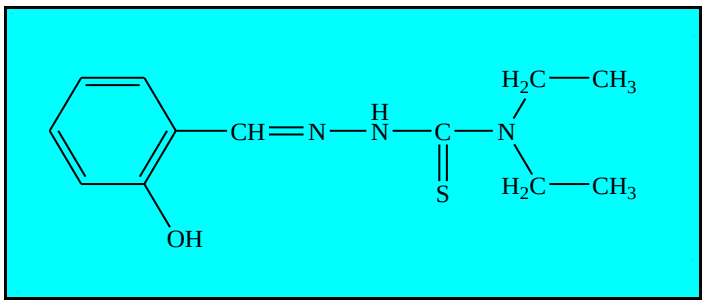

Figure 2: Structure of H_2L_2.

2.4 References

[1] A.O. Sobola, G.M. Watkins and B.Van Brecht, *S. Afr. J. Chem.*, **67** (2014) 45-46.

[2] X. Qin, Y. Ji, Y. Gao, L. Yan, S. Ding, Y. Wang and Z. Liu, *Z. Anorg. Allg. Chem.*, **640** (2014) 462-463.

[3] Y.F. Ji, R. Wang, S. Ding, C.F. Du, Z.L. Liu, *Inorg. Chem. Commun.* **16** (2012) 47–48.

[4] L.F. Audrieth, E.S. Scott and P.S. Kippur, *J. Org. Chem.*, **19** (1954) 733.

[5] N.C. Saha, R. Pradhan, M. Das, N. Khatun, D. Mitra, A. Samanta, A.M.Z. Slawin, A.D. Jana, J. Klanke and E. Rentschler, *J. Coord. Chem.*, **67** (2014) 286-287.

[6] APEX2, SADABS and SAINT (2010), Bruker AXS Inc., Madison, Wisconsin, USA.

[7] G.M. Sheldrick: A short history of *SHELX*. *Acta Crystallogr*., **A64** (2008) 112-122.

[8] A.L. Spek: Structure validation in chemical crystallography. *Acta Crystallogr.*, **D65** (2009) 148-155.

[9] L.J. Farrugia: *WinGX* and *ORTEP for Windows*: an update. *J. Appl. Crystallogr.*, **45** (2012) 849-854.

[10] C.F. Macrae, I.J. Bruno, J.A. Chisholm, P.R. Edgington, P. McCabe, E. Pidcock, L. Rodriguez-Monge, R. Taylor, J. van de Streek and P.A. Wood: *Mercury CSD 2.0* – new features for the visualization and investigation of crystal structures. *J. Appl. Crystallogr.*, **41** (2008) 466-470.

[11] M. Pinsky and D. Avnir, *Inorg. Chem.*, **37** (1998) 5575.

CHAPTER 3

Coordination of 2,6-pyridinedimethanol to Pr(III), Nd(III) and Er(III)

3.1 Introduction

The ligand 2,6-pyridinedimethanol (H_2pydm) is a potentially tridentate *O,N,O*-donor chelating or bridging ligand that can coordinate to metals in a neutral, monoanionic or dianionic form. High-energy O-H and C-H vibrations in the vicinity of the Ln(III) ion have radiationless decay which results in more efficient quenching of fluorescence of the lanthanide ion. To study luminescence, the syntheses and characterisations of Sm, Tb and Eu complexes with H_2pydm were investigated, and the X-ray crystal structure of the Sm(III) complex was obtained. The ORTEP plot of $[Sm(H_2pydm)_3](NO_3)_3$ shows that the nine-coordinate Sm ion has three neutral tridentate H_2pydm ligands, each with one nitrogen and two oxygen donor-atoms. The average Sm-N bond distance was found to be 2.5803 Å, and the Sm-O bond lengths lie in the range 2.422(10)-2.454(10) Å [1]. The structure of $[Sm(H_2pydm)_3](NO_3)_3$ is shown in Figure 1.

The reactions of H_2pydm with $Ln(NO_3)_3{\cdot}xH_2O$ (x = 5 or 6, Ln = Eu, Gd, Tb, Dy, Ho, Er or Yb) in the presence of triethylamine gave isostructural tetranuclear complexes with a zigzag configuration. The complexes have the general formula $[Ln_4(NO_3)_2(H_2pydm)_2(Hpydm)_6](NO_3)_4$, and contain bridges formed by the alkoxido arms of six $Hpydm^-$ groups (see Figure 2). In these complexes the Ln(III) moiety exhibits distorted eight-coordinate complexes, and were found to display interesting magnetic and optical properties. The potential applications of these Ln(III) clusters include single-molecular magnets (SMMs) through the use of anisotropic ions with

significant spin like Dy(III), Tb(III), Ho(III) and Er(III), or as molecular magnetic coolers as in the isotropic and high-spin Gd(III) ion [2].

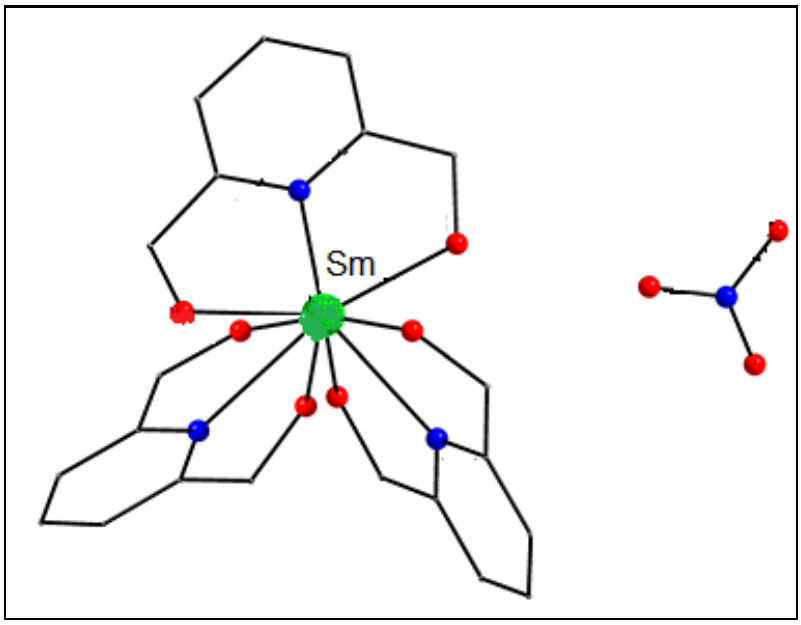

Figure 1: The structure of the $[Sm(H_2pydm)_3](NO_3)_3$ complex. The other two nitrate counter-ions are omitted for clarity.

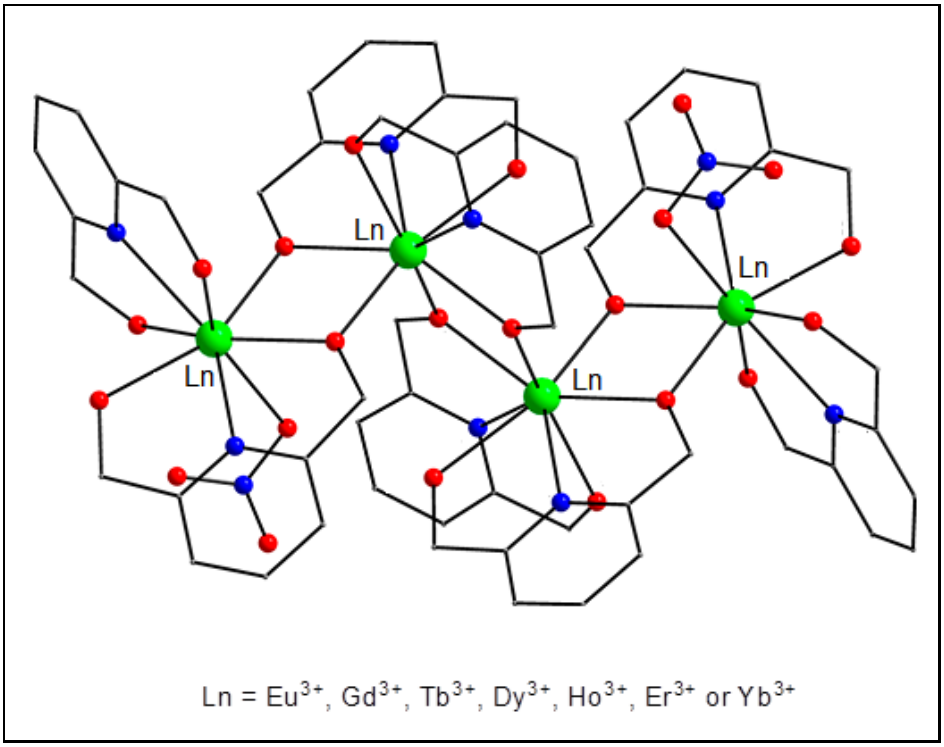

Figure 2: Homometallic 4*f* clusters of the ligand H_2pydm.

Previous studies on 2,6-pyridinedimethanol include complexes with transition metals such as V(V), Cu(II), Ni(II), Co(II) and Hg(II) [3-10]. Stable dioxovanadium(V) complexes of H_2pydm have been synthesised in water at room temperature, and their aqueous acid-base chemistry investigated in order to access their potential use as orally administered glucose-lowering drugs for type 2 diabetes. Stabilisation of the dioxovanadium(V) complexes was achieved through the use of the ligand in the dianionic 2,6-pyridinedimethanolato form (Figure 3) [11]. H_2pydm was also utilised in the synthesis of thermochromic Ni(II) complexes, with the structure shown in Figure 3. Thermochromic behaviour is chromotropism (colour change) induced by a temperature change. The colour change can be due to changes in coordination numbers between six (octahedral) and four (square-planar), or as a result of coordination structural changes between a tetrahedral and a square-planar geometry in the solid state. Changes from a square-planar to an octahedral structure is achieved through the coordination of solvent molecules, such as acetone and acetonitrile [3].

The ligand can act in a neutral tridentate fashion as in $[Co(H_2pydm)_2](F_3CCO_2)_2$, or as a neutral bidentate chelate through the pyridyl nitrogen atom and one hydroxyl oxygen in $[Mn(H_2pydm)_2Cl]Cl$ [10,12]. In $[Cu(H_2pydm)(Hpydm)](ClO_4)$ and $[Co(H_2pydm)(Hpydm)]Cl$, some of the ligands are bound to the metal centre as tridentate monoanionic donors while others are neutral [5,6]. It was also shown that in polynuclear complexes H_2pydm can act as a bridging ligand using the anionic oxygen of the hydroxyl group such as in $[Cu_2(H_2pydm)_2(Hpydm)_2](H_3CCO_2)_2$ [5]. The same bridging behaviour was observed in tetranuclear complexes of H_2pydm with heavy Lns [Eu(III) to Yb(III), except Tm(III)] [2]. The different binding modes of H_2pydm are illustrated in Figure 3.

There is thus much scope for further research into other possible topologies with the lighter lanthanides (La, Ce, Pr and Nd) in order to acquire more information about their coordination nature and spectral properties. In this chapter the reactions of H_2pydm with certain lanthanides were studied, and the complexes $[Ln(H_2pydm)_2(NO_3)_2](NO_3)$ (Ln = Pr or Nd), $[Er(H_2pydm)_3](NO_3)_3$ and $[Pr(H_2pydm)_3](Cl)_3$ were isolated. In all these complexes the ligand H_2pydm is

coordinated tridentately in its neutral form *via* the pyridyl nitrogen atom and two hydroxyl oxygen atoms.

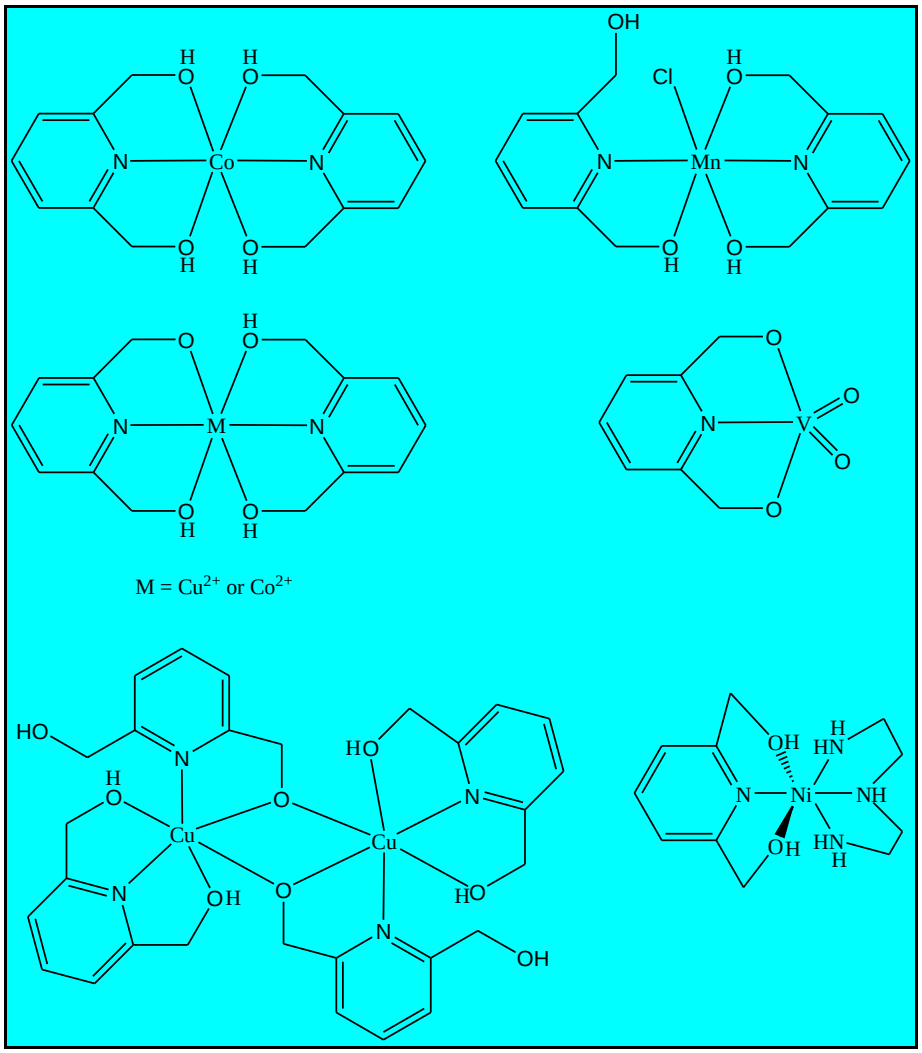

Figure 3: Different coordination modes of H_2pydm with transition metals. All counter-ions are omitted for clarity.

3.2 Synthesis of the complexes

3.2.1 Synthesis of $[Pr(H_2pydm)_2(NO_3)_2](NO_3)$ 1

$Pr(NO_3)_3{\cdot}6H_2O$ (0.213 g, 0.489 mmol) was added to a solution of H_2pydm (0.136 g, 0.977 mmol) in 20 mL methanol. After refluxing the reaction mixture for 1 hour at

70 ºC, the solution was filtered off and diethyl ether (15 mL) was allowed to diffuse slowly into the green solution at 4 ºC. Green X-ray quality crystals were obtained after 8 days (Scheme 1). Yield = 69.5%, m.p. = 199.0-201.8 ºC. Anal. Calcd. for $C_{14}H_{18}N_4O_{10}PrNO_3$ (%): C, 27.78; H, 2.99; N, 11.57. Found: C, 27.63; H, 2.31; N, 11.49. Conductivity (10^{-3} M, DMF): 153.8 $ohm^{-1}cm^2mol^{-1}$. UV-Vis (DMF, λ_{max} nm (ε, $M^{-1}cm^{-1}$)): 446.0 (310), 471.2 (130), 484.2 (110), 594.6 (70). IR (cm^{-1}): *v*(OH) 3418-3000(m), *v*(C-O) 1026(s), *v*(Pr-N_{py}) 1013(s), *v*(Pr-O) 418(s). ^{1}H NMR (DMSO-d_6, δ ppm): 7.78 (t, 1H, Ar), 7.32 (d, 2H, Ar), 5.26 (s, 2H, -OH), 4.50 (s, 4H, -CH_2-).

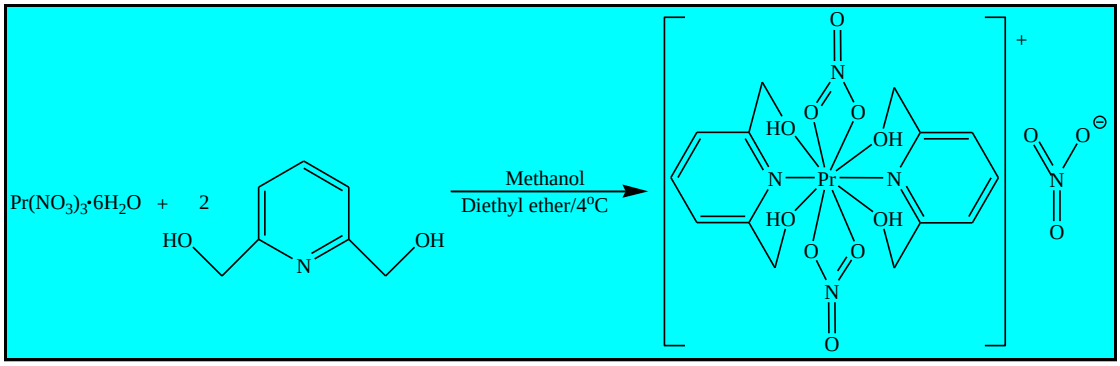

Scheme 1: Synthetic route for the formation of complex **1**.

3.2.2 Synthesis of $[Nd(H_2pydm)_2(NO_3)_2](NO_3)$ 2

$Nd(NO_3)_3·6H_2O$ (0.276 g, 0.630 mmol) was added to H_2pydm (0.175 g, 1.26 mmol) in a solution of 15 mL ethanol:acetonitrile (2:1, v/v). After refluxing the reaction mixture for 1 hour at 65 ºC, diethyl ether (15 mL) was allowed to diffuse slowly into the purple solution at 4 ºC. Purple crystals suitable for X-ray diffraction analysis were obtained after 7 days (Scheme 2). Yield = 31.1%, m.p. = 200.0-203.5 ºC. Anal. Calcd. for $C_{14}H_{18}N_4O_{10}NdNO_3$ (%): C, 27.63; H, 2.98; N, 11.51. Found: C, 27.37; H, 2.58; N, 11.47. Conductivity (10^{-3} M, DMF): 175.3 $ohm^{-1}cm^2mol^{-1}$. UV-Vis (DMF, λ_{max} nm (ε, $M^{-1}cm^{-1}$)): 511.4 (50), 524.2 (60), 582.4 (60), 735.5 (35), 748.0 (35), 799.2 (40), 866.5 (30). IR (cm^{-1}): *v*(OH) 3500-3000(m), *v*(C-O) 1026(s), *v*(Nd-N_{py}) 1013(s), *v*(Nd-O) 422(s). ^{1}H NMR (DMSO-d_6, δ ppm): 7.78 (t, 1H, Ar), 7.33 (d, 2H, Ar), 5.34 (s, 2H, -OH), 4.52 (s, 4H, -CH_2-).

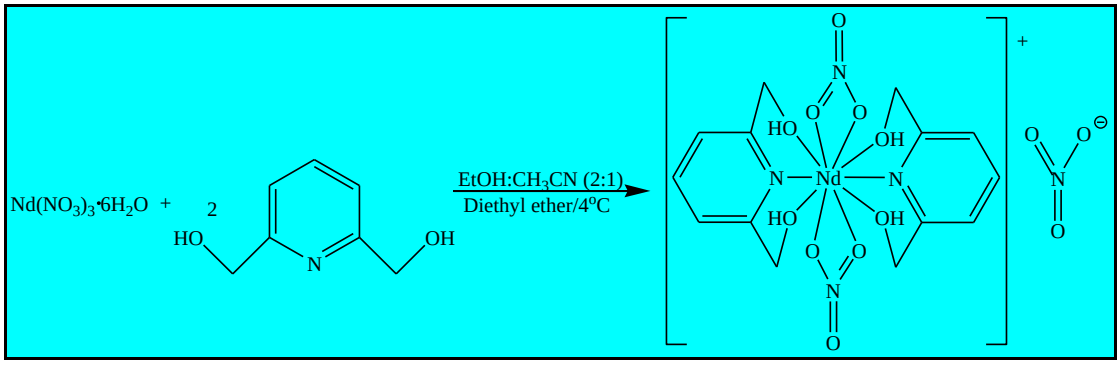

Scheme 2: Synthetic procedure of complex **2**.

3.2.3 Synthesis of $[Er(H_2pydm)_3](NO_3)_3$ 3

$Er(NO_3)_3{\cdot}6H_2O$ (0.282 g, 0.636 mmol) and H_2pydm (0.177 g, 1.27 mmol) dissolved in a 15 mL ethanol:methanol mixture (2:1, v/v) were refluxed for 1 hour, after which the pink solution was filtered off. The slow diffusion of diethyl ether (15 mL) into the pink solution at 4 °C over three days yielded pink crystals that were suitable for X-ray crystallographic studies (Scheme 3). Yield = 46.5%, m.p. = 160.0 °C. Anal. Calcd. for $C_{21}H_{27}ErN_3O_6$,3(NO_3) (%): C, 32.73; H, 3.53; N, 10.90. Found: C, 32.71; H, 3.45; N, 10.93. Conductivity (10^{-3} M, DMF): 138.6 $ohm^{-1}cm^2mol^{-1}$. UV-Vis (DMF, λ_{max} nm (ε, $M^{-1}cm^{-1}$)): 365 (310), 378 (410), 445 (40), 448 (40), 486 (45), 521 (110), 540 (30), 651 (40), 974 (30). IR (cm^{-1}): *v*(C-O) 1036(s), *v*(Er-N_{py}) 1016(s), *v*(Er-O) 423(s). ^{1}H NMR (DMSO-d_6, δ ppm): 7.74 (1H, Ar), 7.27 (2H, Ar), 5.40 (2H, -OH), 4.60 (4H, -CH_2-).

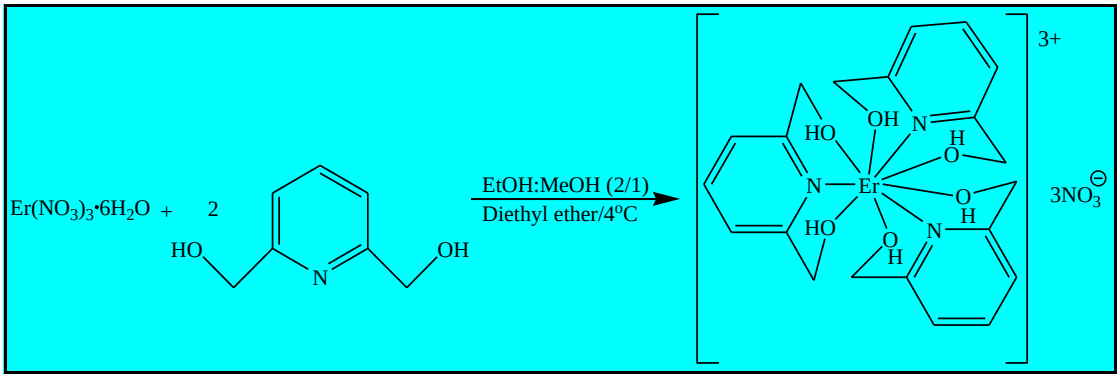

Scheme 3: Synthetic route for complex **3**.

3.2.4 Synthesis of $[Pr(H_2pydm)_3](Cl)_3$ 4

$PrCl_3 \cdot 6H_2O$ (0.230 g, 0.647 mmol) and H_2pydm (0.180 g, 1.29 mmol) were dissolved in dry methanol (15 mL) and the green solution obtained was refluxed for 1 hour. Diethyl ether (15 mL) was allowed to diffuse slowly into the solution at 4 ^oC. The green precipitate which formed after 4 days was recrystallised from a 10 mL DMF:methanol solution (1:1, v/v) under vapour diffusion conditions using diethyl ether. Green X-ray quality crystals were obtained after 10 days (Scheme 4). Yield = 33.7%, m.p. = 210.0 ^oC. Anal. Calcd. for $C_{21}H_{27}N_3O_6PrC_3H_7NOCl_3$ (%): C, 39.07; H, 4.65; N, 7.59. Found: C, 39.33; H, 4.39; N, 7.98. Conductivity (10^{-3} M, DMF): 90.0 $ohm^{-1}cm^2mol^{-1}$. UV-Vis (DMF, λ_{max} nm (ε, $M^{-1}cm^{-1}$)): 447 (45), 470 (25), 484 (30), 596 (20). IR (cm^{-1}): *v*(C-O) 1036(s), *v*(Pr-N_{py}) 1016(s), *v*(Pr-O) 426(s). ^1H NMR (DMSO-d_6, δ ppm): 7.78 (t, 1H, Ar), 7.32 (d, 2H, Ar), 5.33 (s, 2H, -OH), 4.52 (s, 4H, $-CH_2-$).

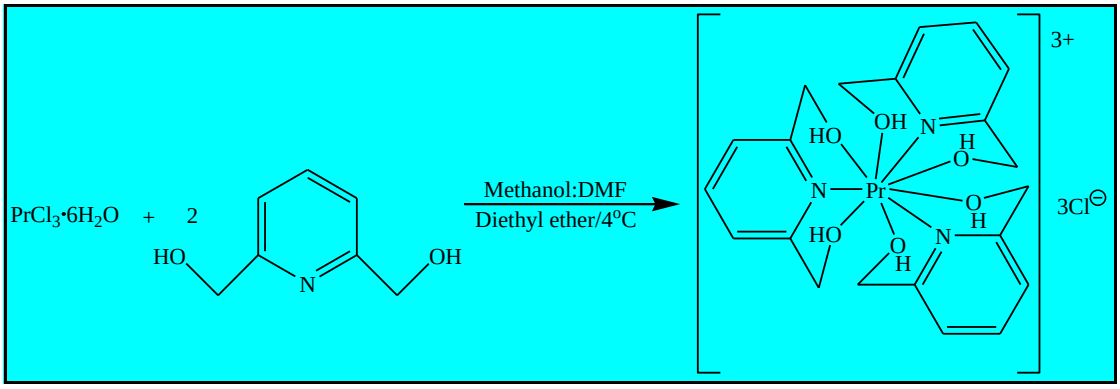

Scheme 4: Synthetic route for the formation of complex **4**.

3.3 Results and discussion

Complexes **1-4** are stable in air and dissolve in DMF, methanol, DMSO and water, while being partially soluble in ethanol (soluble in hot ethanol). They are insoluble in acetonitrile, dichloromethane, chloroform, acetone and diethyl ether.

Molar conductances of 10^{-3} M DMF solutions of the rare-earth complexes, measured at room temperature, were found to lie in the range 90.0-175.3 $ohm^{-1}cm^2mol^{-1}$. From

these high values it can be inferred that complexes **1** and **2** are 1:1 electrolytes while **3** and **4** are 1:3 electrolytes, and hence, ionic in nature. Elemental analyses results are in agreement with the complex formulations.

Reactions in non-aqueous media have been attempted utilising other lanthanide chlorides as starting materials. Unfortunately, precipitates were formed on cooling the reaction solution to room temperature. The complications arising in the synthetic methods could be a result of hydrogen chloride produced in the reactions that often causes side reactions [13].

3.3.1 Infrared spectroscopy

In the IR spectrum of the free ligand, the strong, sharp band at 3350 cm^{-1} is attributed to the *v*(OH). Upon complexation with Pr(III) (**1**) and Nd(III) (**2**) this band becomes broader and is shifted towards the lower frequency region, clearly indicating the coordination of the metal through the hydroxyl oxygen atom (Figure 4a). In complexes **1** and **2** this OH stretching frequency is observed in the 3418-3000 cm^{-1} and 3500-3000 cm^{-1} region, respectively (See Figure 4a). Band broadening can be attributed to the presence of an extensive system of hydrogen bonding in the complexes as well as the nature of the interaction between the oxygen atom of H_2pydm and the Ln(III) ions [14,15]. The shorter the Ln-O bond, the stronger it is and the broader the peak. Thus a broader band is observed for Nd(III) than Pr(III).

The numerous bands appearing in the ~2970-2800 cm^{-1} range of the free H_2pydm are assigned to contributions from the stretching vibrations of the C-H groups. These bands almost disappear in the complexes. A strong band observed at 1051 cm^{-1} in the ligand is due to the C-O frequency, which is shifted to lower energy appearing at 1026 cm^{-1} in the IR spectra of **1** and **2**. This shift in stretching frequency is further evidence that the oxygen of the C-O group is coordinated to the Ln(III) ions in the complexes.

The absorption bands due to the coordinated nitrate groups are observed at 1498 cm^{-1} (ν_4) and 1295 cm^{-1} (ν_1). The frequency separation ($\Delta\nu = \nu_4-\nu_1$) between the symmetric

and asymmetric stretching of this nitrate group is 203 cm^{-1}, an indication of the bidentate coordination of the nitrates with strong covalency [16,17].

Adjacent and almost obscured by the ν(C-O) band in the spectra of complexes are bands at ~1013 cm^{-1} assigned to the ν(Ln-N_{py}). The new bands appearing in the spectra of the complexes at 418 and 422 cm^{-1} are assigned to contributions from the Ln-O vibrations in **1** and **2**, respectively [18].

The high degree in similarity in the IR spectra of **3** and **4** is an indication of similar structures (Figure 4b). The strong C-O stretch at 1051 cm^{-1} in the free ligand is shifted to lower frequency in the spectra of **3** and **4**, appearing at 1036 cm^{-1}. This shift of about 15 cm^{-1} indicates coordination through the oxygen atom of the C-O group. A change in the shape of the OH peak is also observed upon coordination. Adjacent to the ν(C-O) bands of **3** and **4** are bands appearing at about 1016 cm^{-1} which are due to the ν(Ln-N_{py}). The Ln-O stretches appear as medium intensity bands at ~423 and 426 cm^{-1} for **3** and **4**, respectively [18].

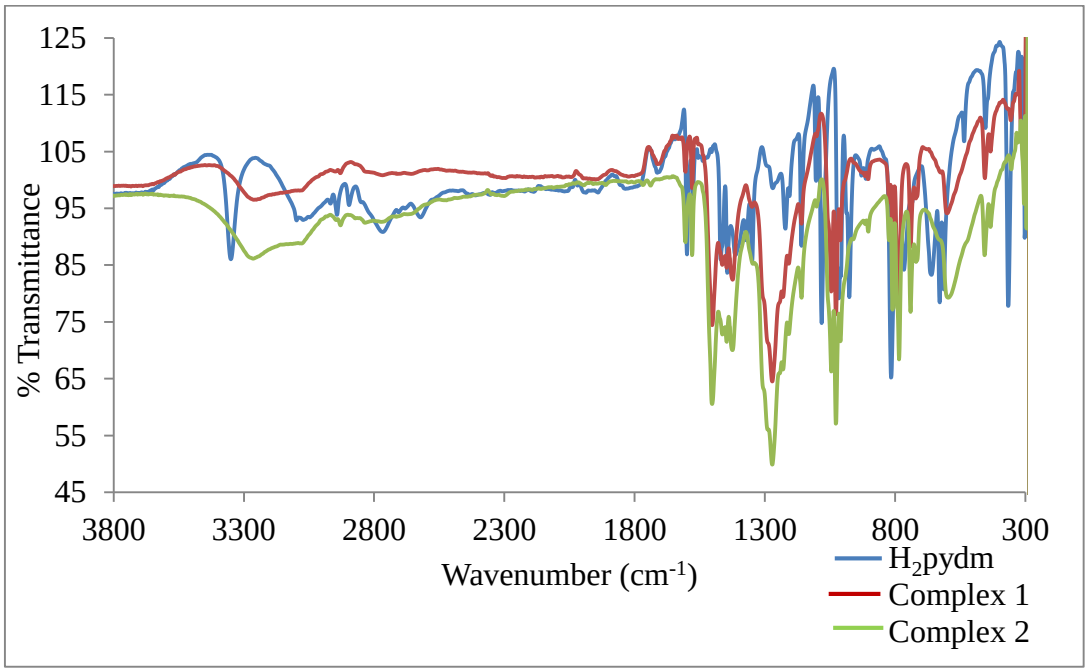

Figure 4a: Overlay IR spectra of H_2pydm, **1** and **2**.

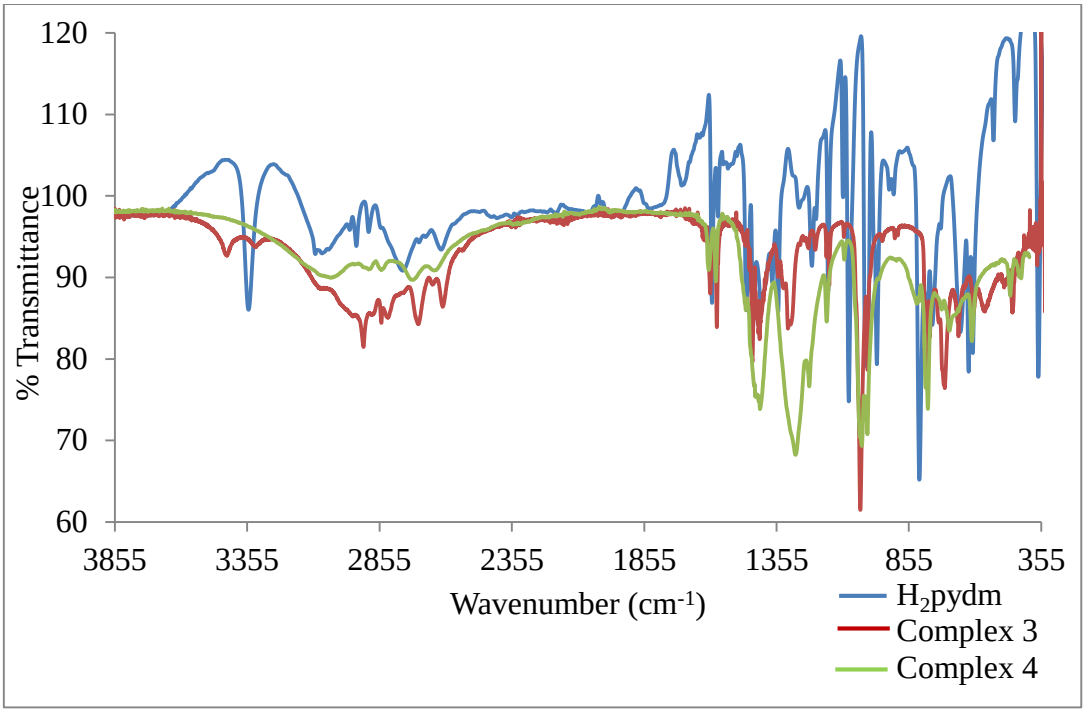

Figure 4b: IR spectra of H_2pydm and complexes **3** and **4**.

3.3.2 NMR analysis

In the ^{1}H NMR spectrum of the free ligand shown in Figure 5a, singlets are observed at 4.53 ppm for the methylene protons and 5.37 ppm for the hydroxyl protons. A doublet occurring at 7.33 ppm is due to the resonance of H_c, while H_d gives a triplet signal at 7.78 ppm.

The spectra of the complexes are shown in Figures 5b-5e. In the ^{1}H NMR spectra of the complexes in DMSO-d_6, all the proton peaks of the H_2pydm are retained. This suggests that the ligand coordinated to the metal ions in its neutral form with no deprotonation occurring. Complexes **1**, **2** and **4** gave reliable ^{1}H NMR spectra that show a great deal of similarity to that of the free ligand. However, the hydroxyl group proton signals are shifted slightly to higher field in **1** and **2** and to a lower field in **3** and **4**. The downfield shift of the –OH proton singlet signal is due to deshielding of the -OH protons. Formation of the Er-O and Pr-O bonds in **3** and **4** lead to a decrease in electron density around the –OH protons which causes the hydroxyl hydrogens to resonate at lower field. In the spectrum of complex **3,** the peaks are broader as is

expected for the paramagnetic Er(III) ion when compared to that of the free ligand. This may be due to significant electron delocalisation between the Er(III) ion and the ligands [19]. Surprisingly, the paramagnetic Nd(III) ion in **2** exhibits no line broadening in its ^{1}H NMR spectrum.

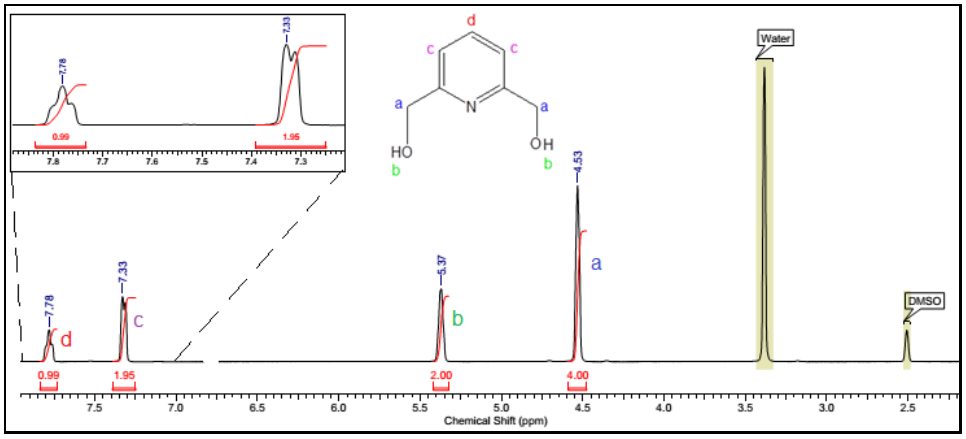

Figure 5a: ^{1}H NMR spectrum of the free H_2pydm.

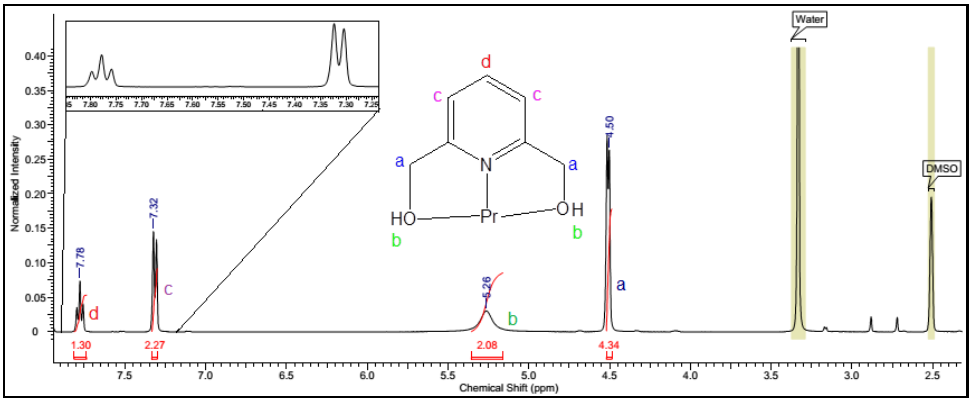

Figure 5b: ^{1}H NMR spectrum of complex **1**.

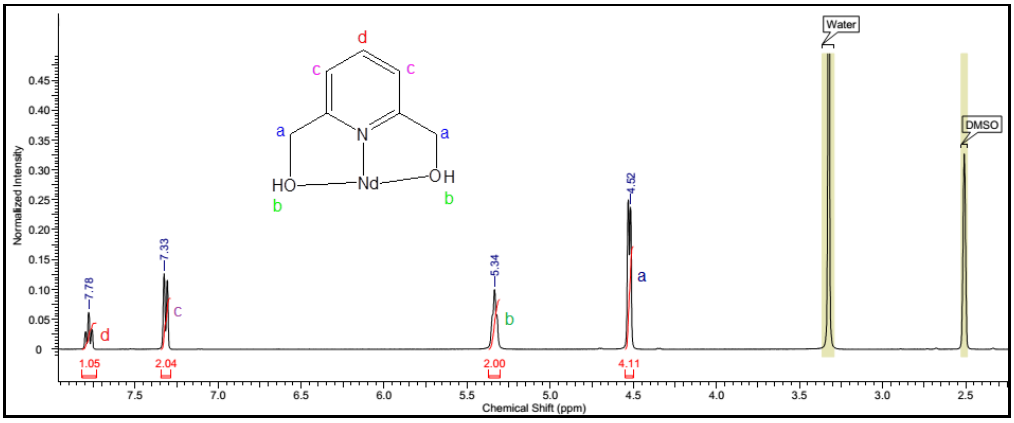

Figure 5c: ^{1}H NMR spectrum of complex **2**.

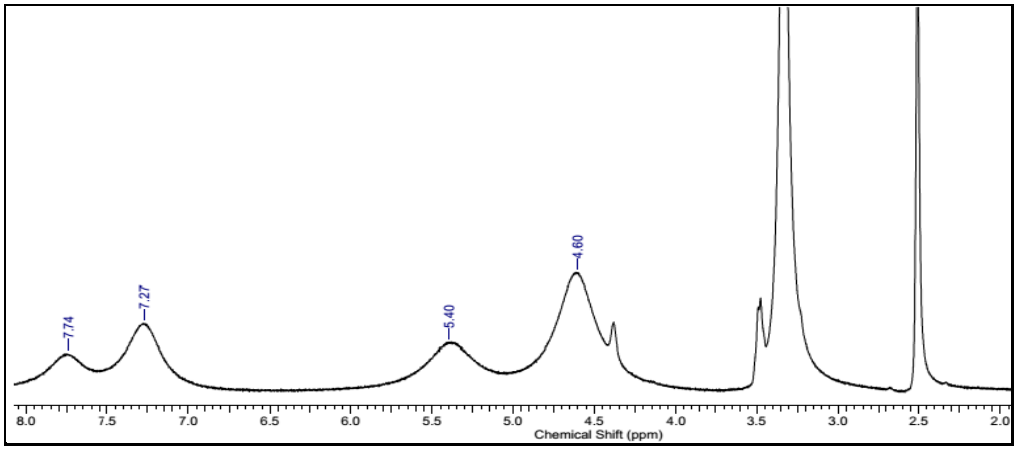

Figure 5d: ^{1}H NMR spectrum of complex **3**.

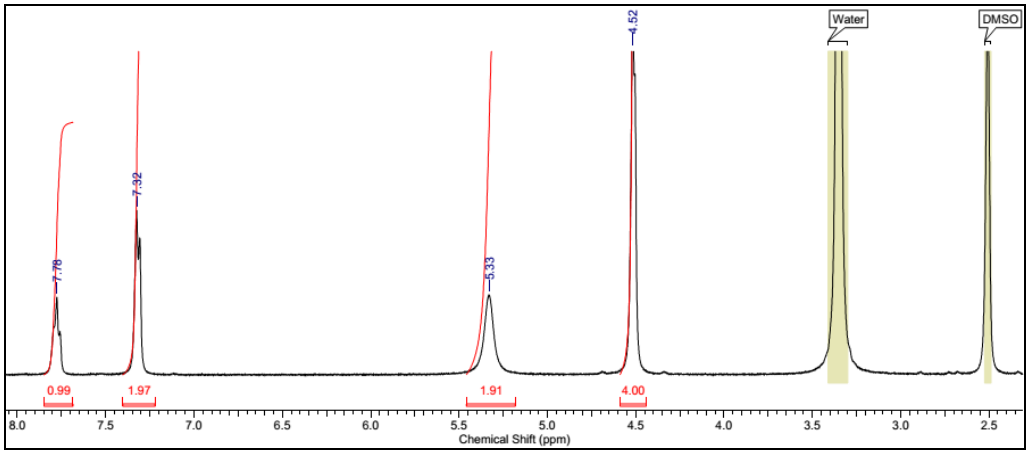

Figure 5e: ^{1}H NMR spectrum of complex **4**.

3.3.3 UV-Vis-NIR spectroscopy

No peaks were observed for the ligand in the ultraviolet and visible range. The absorbance peaks of dissolved $[Pr(H_2pydm)_2(NO_3)_2](NO_3)$ at 446, 471.2, 484.2 and 594.6 nm are due to transitions from the ground level of $^{3}H_4$ to the excited J-levels of the 4*f*-configuration ($^{3}P_2$, $^{3}P_1$, $^{3}P_0$ and $^{1}D_2$) [20]. These correspond to the Pr(III) ion *f-f* transitions for complex **4** at 447, 470, 484 and 596 nm. The seven absorption bands of the Nd(III) complex in the visible and near infrared region appear due to transitions from the ground level of $^{4}I_{9/4}$ to the excited J-levels $^{4}D_{3/2}$, $^{4}G_{9/2}$, $^{4}G_{7/2}$, $^{4}G_{5/2}$, $^{4}S_{3/2}$, $^{4}F_{7/2}$ and $^{2}H_{9/2}$. Five peaks are found in the visible region, with maxima at 511.4, 524.2, 582.4, 735.5 and 748 nm, with very weak bands observed at 511.4 and 735.5 nm. In

the NIR region, peaks are observed at 799.2 and 866.5 nm [20]. The absorption spectra of complexes **1**-**4** are given in Figure 6a and assignments of these weak and narrow peaks (due to Laporte-forbidden *f-f* transitions) are listed in Table 1a [21-23].

Metal-ligand interactions in the complexes were evaluated on the basis of bonding parameters β (nephelauxetic ratio), δ (Sinha's parameter), $b^{1/2}$ (covalent factor) and η (covalency angular overlap parameter). The values of these parameters were calculated using Equations 1-4 below [22,24]:

$$\beta = \sum_{n=1}^{n} \left(v_{complex}/v_{aquo}\right) \quad \ldots 1$$

where $v_{complex}$ and v_{aquo} are the wavenumbers of the *f-f* transitions in the UV-vis-NIR spectra of the lanthanide complex (Figure 6a) and free Ln(III) ion in DMF (Figure 6b), respectively.

$$\delta = \frac{(1-\beta)}{\beta} \text{x} 100 \quad \ldots 2$$

$$b^{1/2} = \sqrt{\frac{1-\beta}{2}} \quad \ldots 3$$

$$\eta = \frac{1-\sqrt{\beta}}{\sqrt{\beta}} \quad \ldots 4$$

For the free Pr(III) ion in DMF, the wavenumbers were obtained by considering the peaks with maxima at 443, 470, 484 and 597 nm, while for Nd(III) the peaks are positioned at 514, 525, 583, 741, 751, 803 and 868 nm. The Er(III) ion peak maxima are located at 366, 378, 445, 452, 490, 521, 543 and 655 nm (Figure 6b). Bonding parameters obtained after calculations are shown in Table 1b.

Pr(III) complexes **1** and **4** gave identical bonding parameter values. The nephelauxetic ratios are less than one and the Sinha's parameters and covalent factors are positive values, thereby suggesting some covalent character in the Pr-ligand bonds. Therefore, there is more electron density delocalisation in the Pr(III) complexes leading to

increasing bond covalency. For **2** and **3** the β values are greater than one and the negative δ values indicate that the interactions between Nd(III) [or Er(III)] and the ligands are basically electrostatic (more ionic) and there is an insignificant role of the 4*f* orbitals in bonding [22,25]. It is interesting to note that with increasing atomic number from Pr(III) to Er(III), the magnitudes of β, δ and η decrease, thus indicating a decrease in the extent of the covalent character of the Ln-ligand bond. A decrease in covalent character of the Ln-ligand bonds in the heavier lanthanide complexes is consistent with the observations made previously [25,26].

Table 1a: Absorption bands for complexes **1**-**4**.

λ (nm)	**Assignment**		**λ (nm)**	**Assignment**
Complex **1**			Complex **3**	
446.0	$^3H_4 \rightarrow {}^3P_2$		365	$^4I_{15/2} \rightarrow (^4G_{9/2}, {}^2K_{15/2}, {}^2G_{7/2})$
471.2	$^3H_4 \rightarrow {}^3P_1$		378	$^4I_{15/2} \rightarrow {}^4G_{11/2}$
484.2	$^3H_4 \rightarrow {}^3P_0$		445	$^4I_{15/2} \rightarrow {}^4F_{5/2}$
594.6	$^3H_4 \rightarrow {}^1D_2$		448	$^4I_{15/2} \rightarrow {}^4F_{3/2}$
			486	$^4I_{15/2} \rightarrow {}^4F_{7/2}$
Complex **2**			521	$^4I_{15/2} \rightarrow {}^2H_{11/2}$
511.4	$^4I_{9/2} \rightarrow {}^4D_{3/2}$		540	$^4I_{15/2} \rightarrow {}^4S_{3/2}$
524.2	$^4I_{9/2} \rightarrow {}^4G_{9/2}$		651	$^4I_{15/2} \rightarrow {}^4F_{9/2}$
582.4	$^4I_{9/2} \rightarrow {}^4G_{7/2}$		974	$^4I_{15/2} \rightarrow {}^4I_{11/2}$
735.5	$^4I_{9/2} \rightarrow {}^4G_{5/2}$			
748	$^4I_{9/2} \rightarrow {}^4S_{3/2}$		Complex **4**	
799.2	$^4I_{9/2} \rightarrow {}^4F_{7/2}$		447	$^3H_4 \rightarrow {}^3P_2$
866.5	$^4I_{9/2} \rightarrow {}^2H_{9/2}$		470	$^3H_4 \rightarrow {}^3P_1$
			484	$^3H_4 \rightarrow {}^3P_0$
			596	$^3H_4 \rightarrow {}^1D_2$

Table 1b: Bonding parameters for complexes **1-4**.

Complex	β	δ (%)	$b^{1/2}$	η
1	0.998	+0.20	0.032	0.0010
2	1.003	-0.30	-	-0.0015
3	1.004	-0.40	-	-0.0020
4	0.998	+0.20	0.032	0.0010

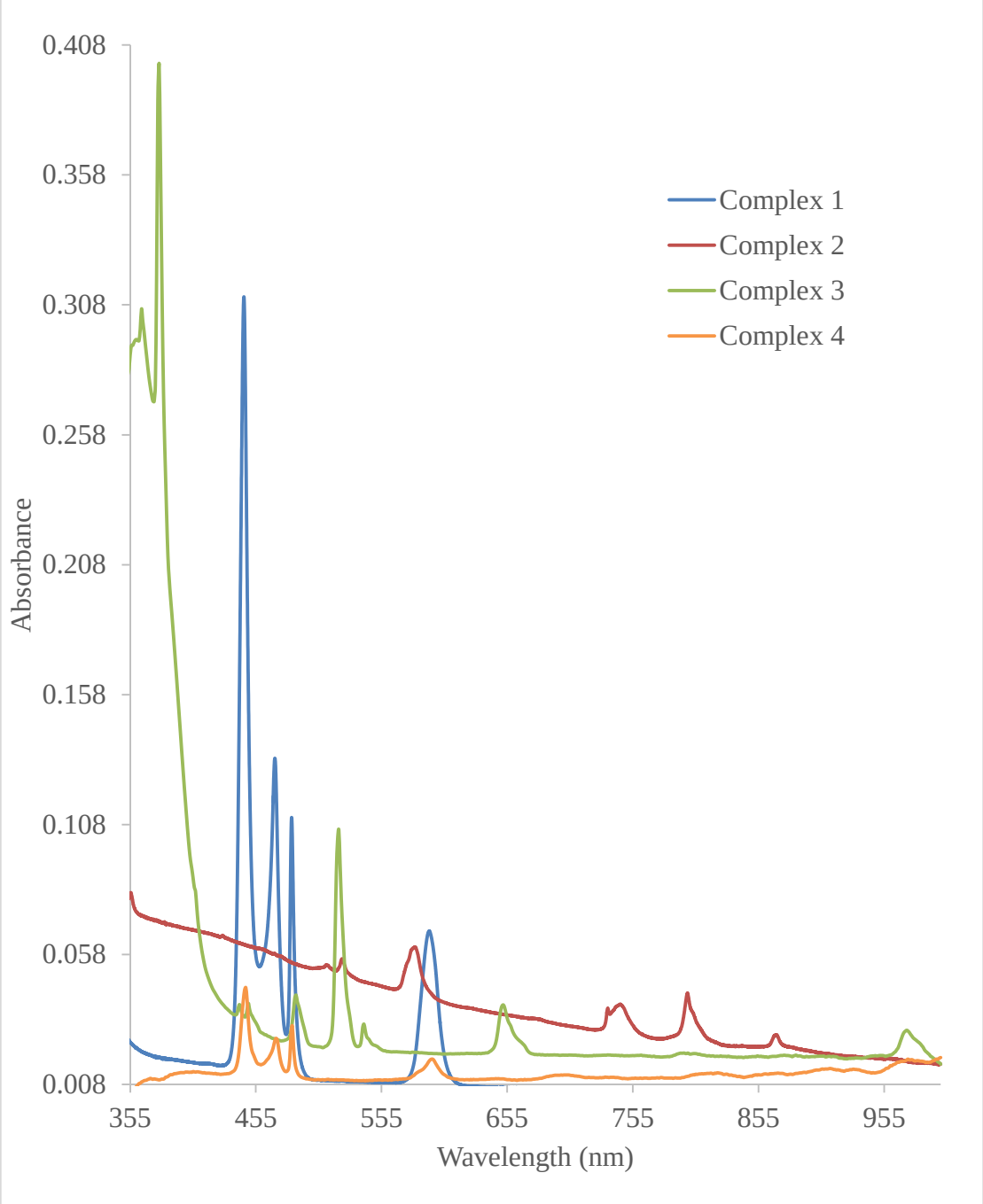

Figure 6a: UV-vis-NIR spectra of 10^{-3} M DMF solutions of complexes **1-4**.

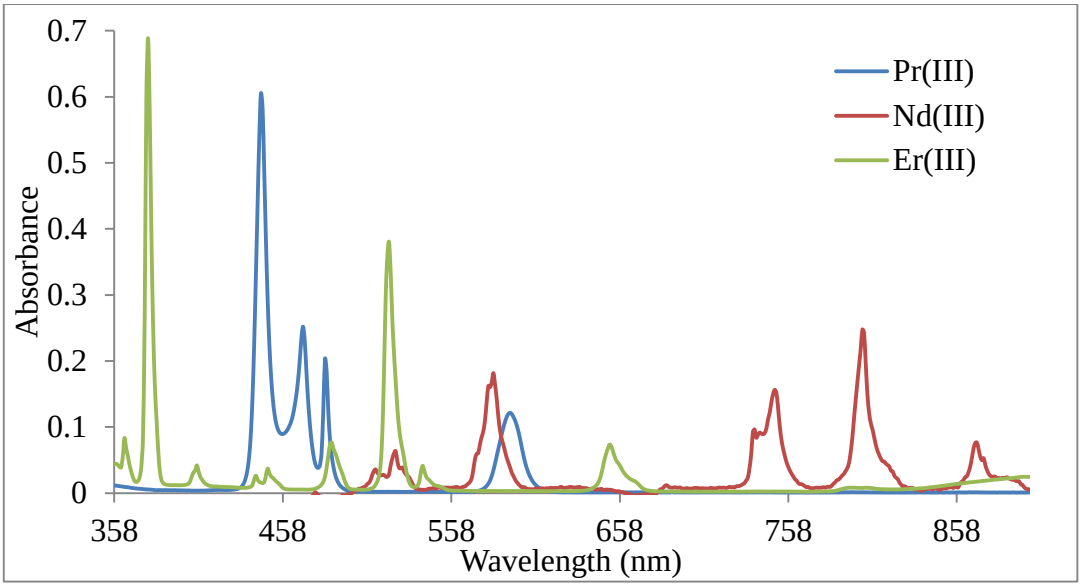

Figure 6b: UV-Vis spectra of free metal ions in DMF.

3.3.4 Shape analysis

Coordination geometries around the lanthanide centres were analysed using SHAPE 2.1 software. The ideal Johnson geometries (JBCCU-10, JBCSAPR-10, JMBIC-10, JATDI-10 and JSPC-10) were not considered in this geometry analysis since they are normally used in describing the structures of clusters or polynuclear complexes with metal-metal bonds or metal-bridging ligand-metal sequences [27]. The coordination polyhedrons of the complexes are shown in Figures 7a-7d.

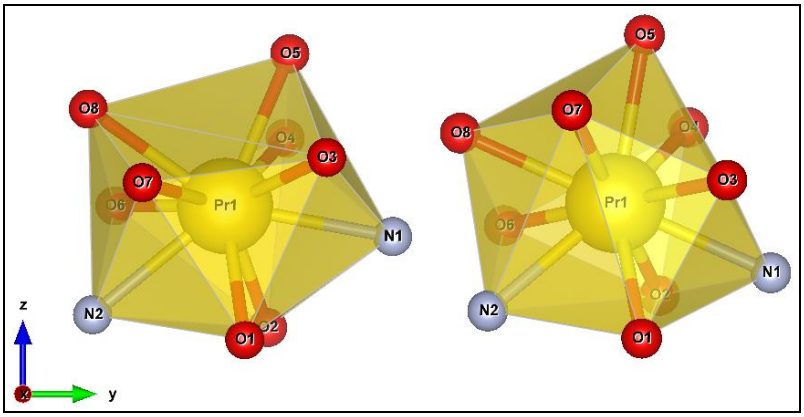

Figure 7a: Tetradecahedron (TD-10) coordination polyhedron of complex **1** (left) and the ideal TD-10 (right).

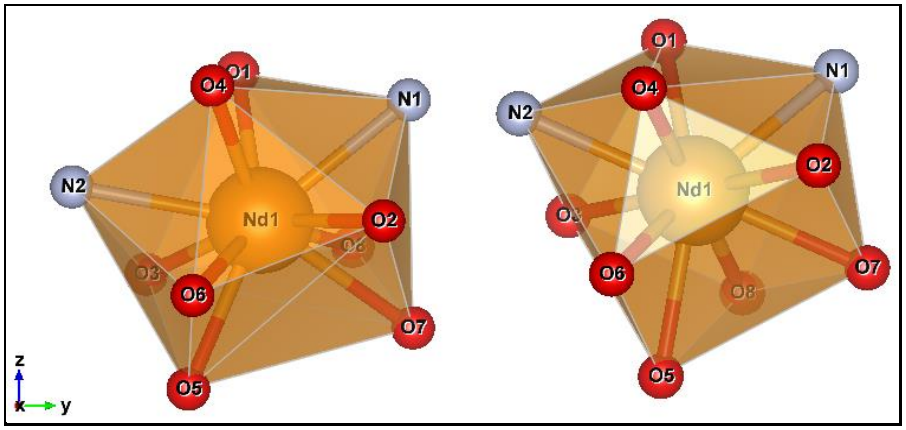

Figure 7b: Coordination sphere of the ten-coordinate Nd(III) complex (left) and the ideal TD-10 geometry (right).

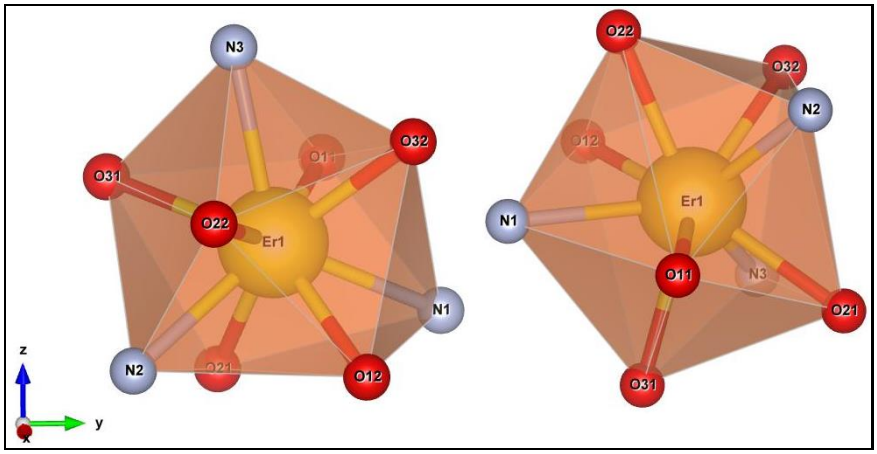

Figure 7c: Coordination sphere of the nine-coordinate Er(III) (left) and the ideal spherical tricapped trigonal prism (TCTPR-9) shape (right).

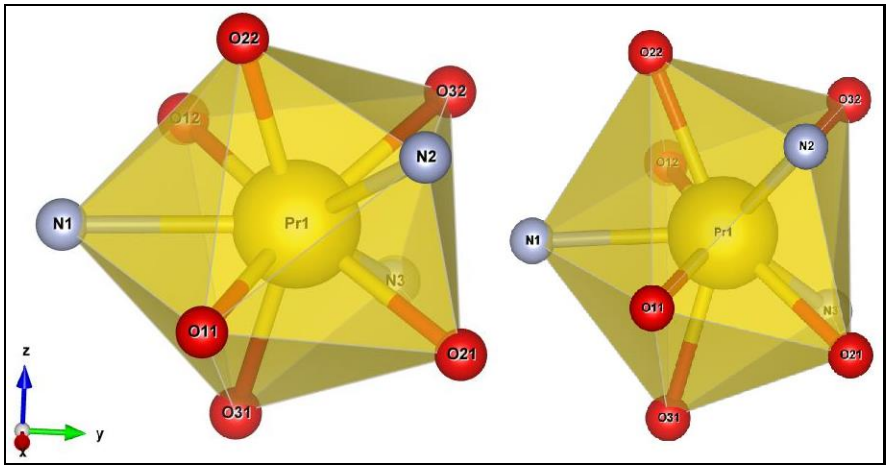

Figure 7d: View along the x-axis of the TCTPR coordination polyhedron of the nine-coordinate Pr(III) (left) and ideal TCTPR (right).

Table 2: CShM values for lanthanide complexes with H_2pydm.

Complexes **1** and **2**								
	DP-10	EPY-10	OBPY-10	PPR-10	PAPR-10	SDD-10	TD-10	HD-10
Pr(III)	34.3713	23.1993	15.4308	9.6967	12.8621	6.7868	**5.9458**	8.9408
Nd(III)	34.4359	23.2392	15.4181	9.6846	12.8901	6.7569	**5.9099**	8.9547
Complexes **3** and **4**								
	EP-9	OPY-9	HBPY-9	CCU-9	CSAPR-9	TCTPR-9	HH-9	MFF-9
Er(III)	34.6786	23.3385	18.1757	8.4938	1.3991	**1.1102**	12.2885	1.9216
Pr(III)	32.8360	24.3160	17.8101	8.4187	2.0490	**1.7203**	12.2185	2.5975

With reference to Table 2 above, it is noticed that the tetradecahedron (TD-10) geometry best describes the molecular geometries of **1** and **2** since it produced the smallest continuous shape measure (CShM) values. The Pr(III) complex shows slightly higher distortion (higher CShM value) from the ideal TD-10 compared to the Nd(III) complex. The complexes thus show D_{2d} symmetry and possess 22 edges and layers in the ratio 2:6:2, and 12_3+2_4 faces (twelve triangles and two squares) [27,28].

The calculations show that the nine-coordinate complexes **3** and **4** exhibit a spherical tricapped trigonal prism (TCTPR-9) geometry (D_{3h}), and the deviation parameters are 1.1102 and 1.7203, respectively. This is a moderate deviation from an ideal D_{3h} symmetry. The CShM values of these complexes lie between 0.1 and 3, which is considered significant but still correspond to a small distortion from an ideal geometry [2,29].

Ten-coordinate complexes gave higher deviation parameters compared to nine-coordinate complexes. This is because distortions from the reference shape are attributed to the flexibility and the higher coordination numbers of the lanthanide ion. As a result, it is difficult to control the local geometries around the Ln(III) centres [30]. Complex **3** gave the smallest deviation from ideal shape due to stronger coordination that results in less flexibility as well as less steric repulsion due to its lower coordination number. Full names of geometries are listed in Table 5.

3.3.5 Crystal data

Single-crystal X-ray diffraction analyses provided insight into the structure of the lanthanide nitrate complexes with H_2pydm. The ORTEP plots with the atom-labelling scheme for the $[Ln(H_2pydm)_2(NO_3)_2](NO_3)$ (Ln = Pr or Nd) complexes are shown in Figures 8a and 8b, respectively. In both complexes, the H_2pydm ligand coordinates to the Ln(III) ion in its neutral form as a tridentate *O,N,O*-donor ligand through the pyridyl nitrogen and the two hydroxyl oxygen atoms. Two tridentate H_2pydm ligands and two bidentate nitrates are coordinated to the metal centre, thus giving ten-coordinate complexes. The crystal structures consist of a $[Ln(H_2pydm)_2(NO_3)_2]^+$ cation and one NO_3^- anion, in which the metals are in +3 oxidation states.

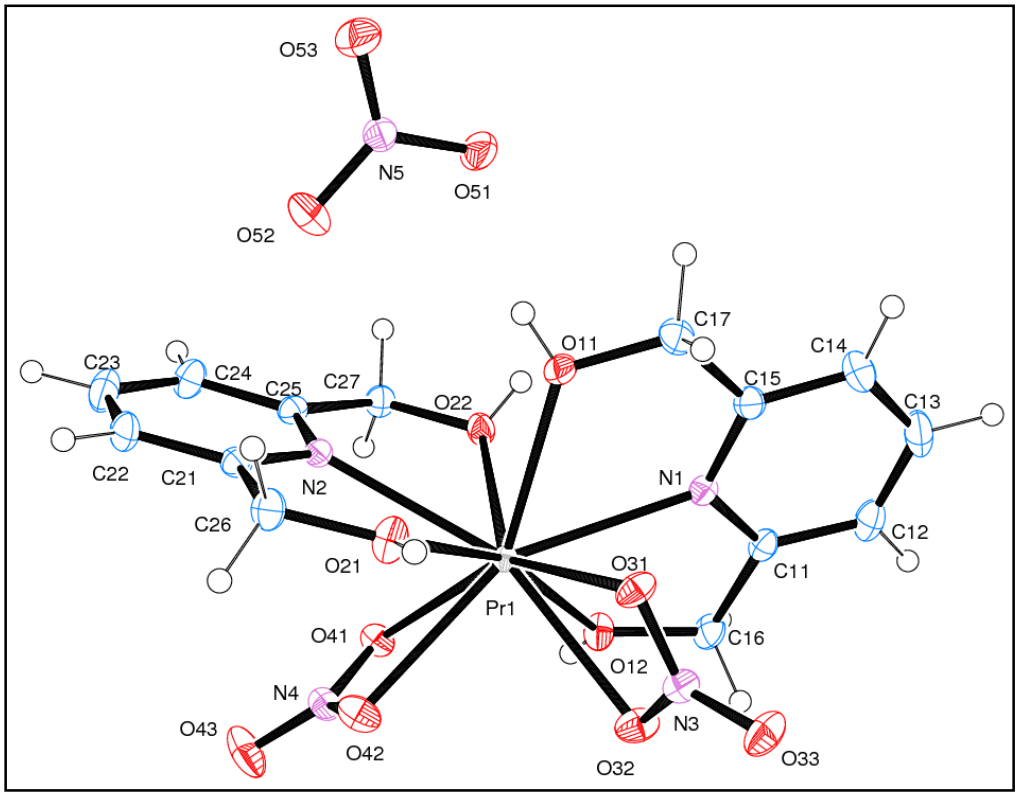

Figure 8a: ORTEP view of complex **1** showing 50% probability displacement ellipsoids and the atom-labelling.

Selected bond lengths and angles in **1** and **2** are given in Tables 3a and 3b, respectively. The Pr-$O_{nitrate}$ bond lengths are in the range of 2.5540(12)–2.6383(11) Å, while the Pr-O_{pydm} bond lengths are relatively shorter, in the range 2.4677(12)-

2.4938(13) Å. The same trends are observed in complex **2**, where the Nd-O_{pydm} bond lengths are shorter than the Nd-$O_{nitrate}$ bonds. The average Ln(III)-N bond lengths for complexes **1** and **2** are 2.5916 and 2.5827 Å, respectively. Thus, the effect of the lanthanide contraction is evidenced by the decrease in Ln-N bond lengths from Pr to Nd. The O-Ln-O nitrate bite angles are larger in complex **2** (average = 49.31°) than in complex **1** (average = 49.19°). In both **1** and **2**, the coordinated nitrate oxygen atoms (O_c) have longer N-O_c bond lengths [1.2591(18)-1.2881(19) Å] than the free (uncoordinated) N-O [1.211(2)-1.217(2) Å], and the O_c-N-O_c angles [115.82(14)-116.22(13)°] are comparatively smaller than the ideal 120° of the isolated nitrate anion [31].

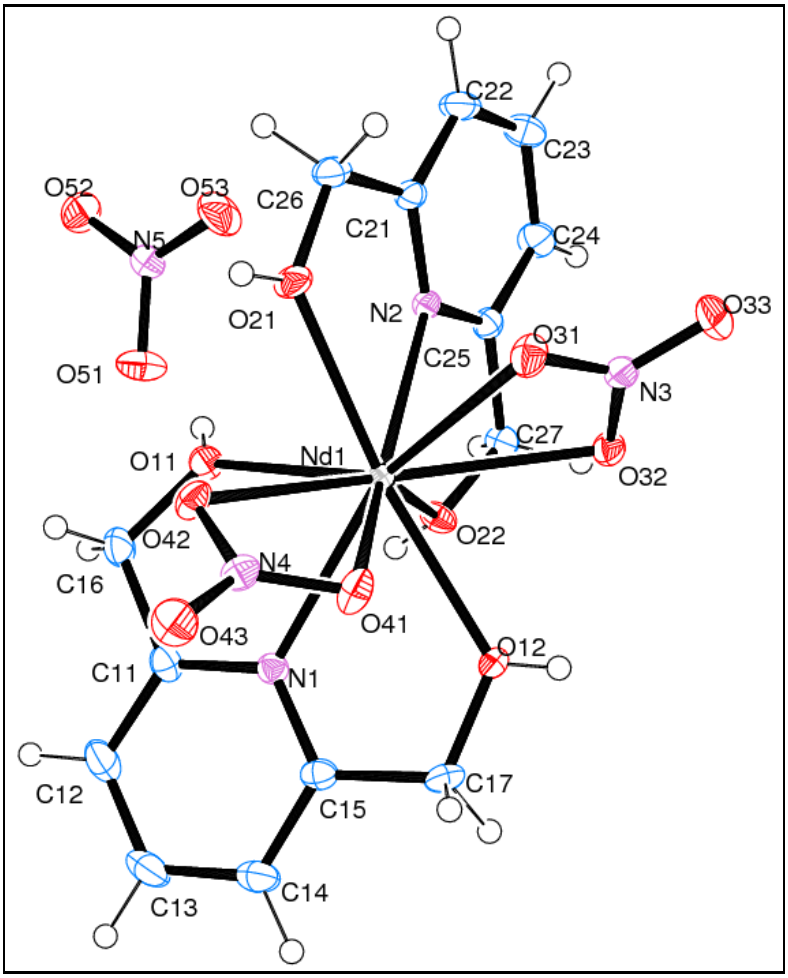

Figure 8b: ORTEP view of complex **2** (50% probability ellipsoids).

Table 3a: Selected bond lengths and angles in complex **1**.

Bond lengths (Å)		**Bond angles (°)**	
Pr1-O11	2.4889(12)	O11-Pr1-N1	62.64(4)
Pr1-O12	2.4677(12)	O12-Pr1-N1	61.87(4)
Pr1-O21	2.4938(13)	O11-Pr1-O12	120.20(4)
Pr1-O22	2.4708(12)	O21-Pr1-N2	61.64(4)
Pr1-O31	2.5836(12)	O22-Pr1-N2	63.19(4)
Pr1-O32	2.5940(13)	O21-Pr1-O22	120.54(4)
Pr1-O41	2.6383(11)	O31-Pr1-O32	49.38(4)
Pr1-O42	2.5540(12)	O41-Pr1-O42	49.04(4)
Pr1-N1	2.5966(13)		
Pr1-N2	2.5865(14)		

Table 3b: Selected bond lengths and angles in complex **2**.

Bond lengths (Å)		**Bond angles (°)**	
Nd1-O11	2.4796(14)	O11-Nd1-N1	62.77(5)
Nd1-O21	2.4890(14)	O12-Nd1-N1	62.04(4)
Nd1-O22	2.4631(12)	O11-Nd1-O12	120.48(4)
Nd1-O31	2.5452(13)	O21-Nd1-N2	61.68(4)
Nd1-O32	2.6315(12)	O22-Nd1-N2	63.38(4)
Nd1-O42	2.5753(13)	O21-Nd1-O22	120.78(5)
Nd1-N1	2.5885(15)	O31-Nd1-O32	49.16(4)
Nd1-N2	2.5769(15)	O41-Nd1-O42	49.46(4)

Plots of the structures showing hydrogen bonding networks in **1** and **2** are given in Figures 8c and 8d, and hydrogen bond parameters are listed in Tables 3c and 3d. In complexes **1** and **2**, the hydrogen atoms of the hydroxyl groups of the H_2pydm ligands

are involved in hydrogen bonds of the O-H···O type. These occur between the hydroxyl hydrogen atoms and the coordinated nitrate oxygen atoms, as well as with the negatively charged oxygen atom of the nitrate counter-anion. Additionally, the methylene hydrogen atoms of H_2pydm also form weak C-H···O interactions with the oxygen atoms of the coordinated and uncoordinated nitrates. Thus, crystal packing is determined by the hydrogen bonding as well as weak C-H···O contacts.

Table 3c: Hydrogen bond geometry (Å, °) in complex **1**.

D*-H···*A	***D*-H**	**H···*A***	***D*···*A***	***D*-H···*A***
O(11)-H(11A)···O(51)	0.80(2)	1.97(2)	2.7308(18)	161(2)
O(12)-H(12A)···O(31)	0.80(2)	1.98(2)	2.7604(16)	167(2)
O(21)-H(21A)···O(41)	0.79(2)	2.00(2)	2.7688(17)	166(2)
O(22)-H(22A)···O(51)	0.79(2)	1.92(2)	2.7018(17)	169(2)
C(13)-H(13)···O(53)	0.9500	2.5000	3.356(3)	149.00
C(16)-H(16B)···O(42)	0.9900	2.4700	3.420(2)	161.00
C(22)-H(22)···O(42)	0.9500	2.4900	3.409(2)	163.00

D = donor, *A* = acceptor

Table 3d: Hydrogen bond parameters (Å, °) in complex **2**.

D*-H···*A	***D*-H**	**H···*A***	***D*···*A***	***D*-H···*A***
O(11)-H(11A)···O(51)	0.74(2)	2.03(2)	2.7320(19)	160(2)
O(12)-H(12A)···O(42)	0.76(3)	2.02(3)	2.7637(18)	168(2)
O(21)-H(21A)···O(32)	0.74(2)	2.05(2)	2.7724(18)	165(2)
O(22)-H(22A)···O(51)	0.77(2)	1.94(2)	2.7035(17)	170(3)
C(13)-H(13)···O(52)	0.9500	2.5000	3.356(3)	149.00
C(17)-H(17A)···O(31)	0.9900	2.4700	3.422(2)	162.00
C(22)-H(22)···O(31)	0.9500	2.5000	3.415(2)	163.00

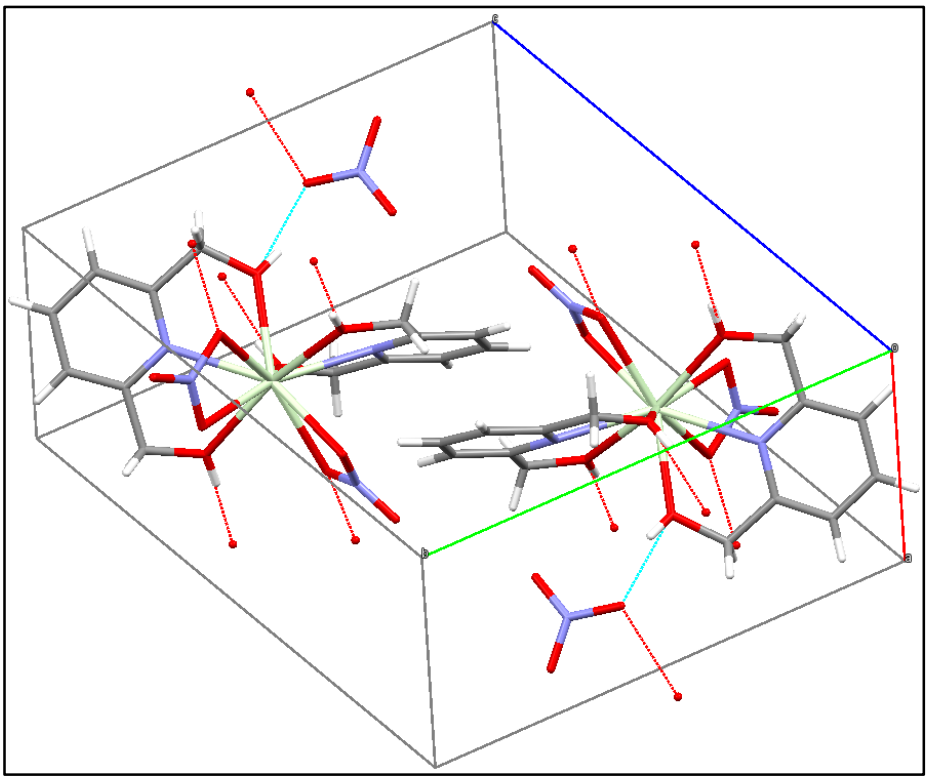

Figure 8c: Hydrogen bonding in complex **1** (*Mercury 3.6*)

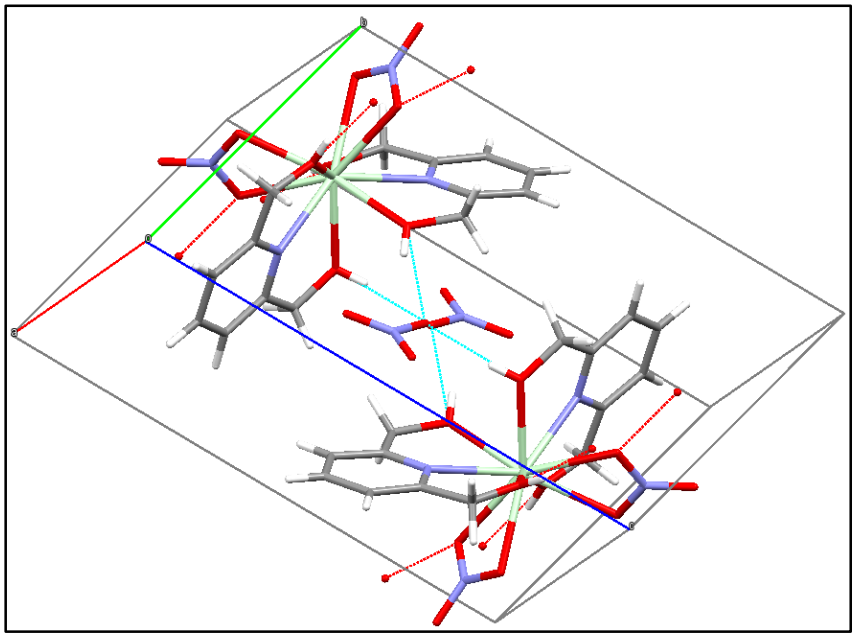

Figure 8d: Hydrogen bonding in complex **2**.

The ORTEP plots with atom-labelling for **3** and **4** are depicted in Figures 8e and 8f, respectively. As with complexes **1** and **2**, H_2pydm serves as a tridentate ligand in

complexes **3** and **4** using all three available donor sites. The resulting nine-coordinate Ln(III) ions are bound to three H_2pydm ligands, with bond distances Pr-O 2.455(2)-2.478(2), Pr-N 2.6355(19)-2.642(2) Å, Er-O 2.3510(16)-2.3804(17) and Er-N 2.491(2)-2.522(2) Å, respectively. A lower coordination number in **3** was achieved because of the small ionic radius of the Er(III) ion whereas a higher coordination number in **1** relative to **4** is attributed to stronger coordination of the more electronegative NO_3^- compared to the Cl^- ion [32,33]. Thus, substitution of the chlorides from the coordination sphere is easier than that of the nitrates.

For **1** and **2** the bond lengths are relatively longer than the corresponding distances reported previously for $[Sm(H_2pydm)_3](NO_3)_3$ [ranges of 2.422(10)-2.454(10) Å for Sm-O and 2.571(11)-2.590(11) Å for Sm-N bonds] while those for complex **3** are shorter than for the Pr(III), Nd(III) and Sm(III) complexes [1]. The average Ln-O bond distance in **4** is shorter than in **1** and **2**, while the mean Ln-N bond length in **4** is longer than the corresponding bonds observed in **1** and **2**. The trends in Ln-N bond lengths are consistent with a predominantly electrostatic character of the Ln-ligand bonds. The presence of the two coordinated nitrate counter-ions in the coordination spheres of **1** and **2** lead to an increase in the electron donation towards the vacant *d*-orbitals and a decrease in the total atomic charge of cations. The result is shortening of metal-nitrogen bond lengths [34]. Therefore, by changing the coordination sphere of the complexes, the Ln-ligand bond distances are altered due to the effect of counter-ions.

The H_2pydm ligands are neutral, therefore complexes **3** and **4** contain three nitrate and three chloride counter-anions, respectively. These results are in agreement with previous observations that small bite angle ligands such as nitrate preferentially bind to larger lanthanide ions as confirmed by the binding of two nitrates in complexes **1** and **2** and their substitution in complex **3** [35]. Both structures consists of $[Ln(H_2pydm)_3]^{3+}$ cations, with three NO_3^- and three chlorides as counter-ions for **3** and **4**, respectively .

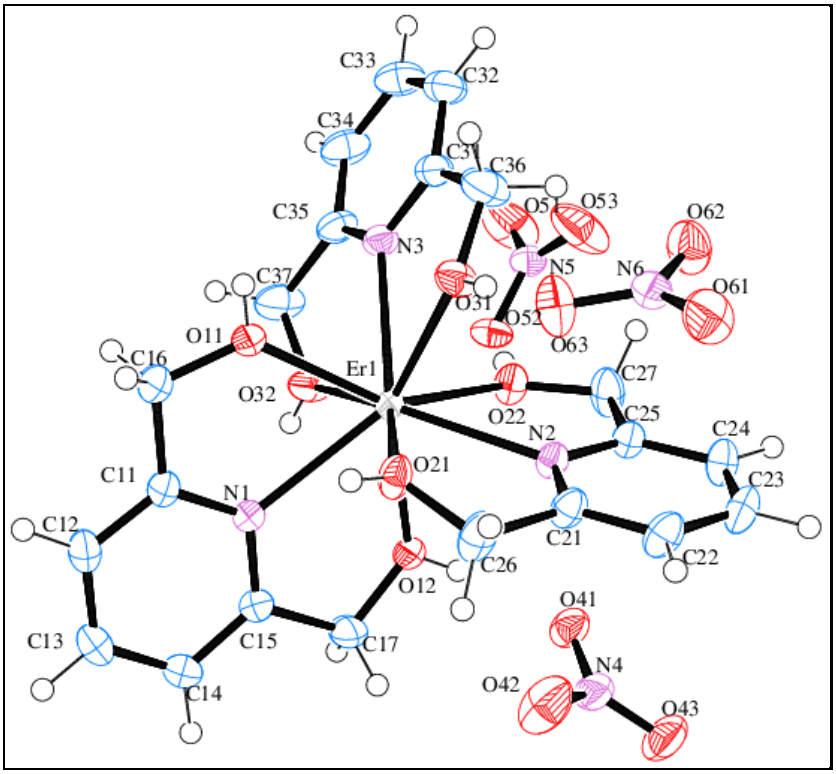

Figure 8e: ORTEP view of complex **3** showing 50% probability displacement ellipsoids and the atom-labelling scheme.

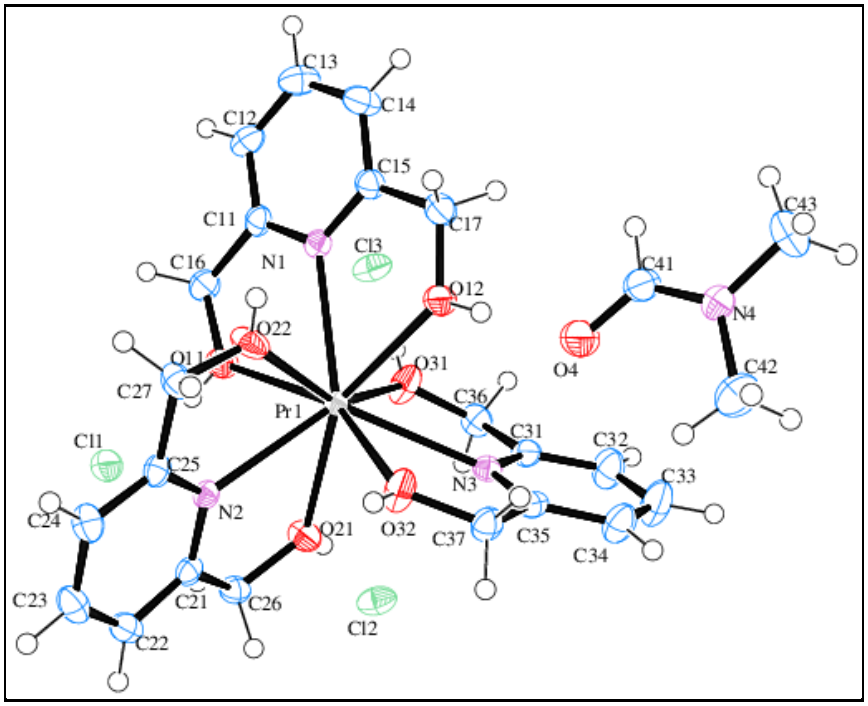

Figure 8f: Molecular structure of complex **4** with displacement ellipsoids drawn at the 50% probability level.

Selected bond lengths and angles for **3** and **4** are listed in Tables 3e and 3f. The O-Ln-O bite angles of H_2pydm decrease in the order Er(III) > $Pr(III)_{complex\ 4}$ > Nd(III) > $Pr(III)_{complex\ 1}$. Larger bite angles in nine-coordinate complexes are an indication of lower congestion than in ten-coordinate complexes where there is increased steric crowding around the metal centre [36]. A correlation also exists between ligand bite angles and bond distances. The shorter the Ln-O bond length, the greater the ligand bite angle. The Ln-O and Ln-N bond distances for complexes **1**-**4** are normal and comparable to those of related lanthanide compounds found in the literature [1,2,37]. An example is triammoniumtris(pyridine-2,6-dicarboxylato-*O,N,O'*)neodymiate(III) heptahydrate in which the Nd-N_{py} bond lengths are in the range 2.554(3)-2.570(3) Å, and Ln-O bond distances are comparable to the Sm-O bond lengths in $[Sm(H_2pydm)_3](NO_3)_3$ which were found to lie in the range of 2.422(10) to 2.454(10) Å [1,38].

Table 3e: Selected bond lengths and angles in complex **3**.

Bond lengths (Å)		**Bond angles (°)**	
Er1-O11	2.3510(16)	O11-Er1-O12	127.83(6)
Er1-O12	2.3553(17)	O11-Er1-N1	64.07(7)
Er1-O21	2.3804(17)	O12-Er1-N1	63.84(7)
Er1-O22	2.3560(16)	O21-Er1-O22	128.60(6)
Er1-O31	2.3649(18)	O21-Er1-N2	64.76(7)
Er1-O32	2.3550(19)	O22-Er1-N2	63.84(7)
Er1-N1	2.518(2)	O31-Er1-O32	126.65(6)
Er1-N2	2.491(2)	O31-Er1-N3	62.87(7)
Er1-N3	2.522(2)	O32-Er1-N3	63.99(7)

Table 3f: Selected bond lengths and angles in complex **4**.

Bond lengths (Å)		**Bond angles (°)**	
Pr1-O11	2.478(2)	O11-Pr1-O12	123.71(6)
Pr1-O12	2.469(2)	O11-Pr1-N1	62.07(7)
Pr1-O21	2.466(2)	O12-Pr1-N1	61.64(6)
Pr1-O22	2.455(2)	O21-Pr1-O22	123.48(7)
Pr1-O31	2.473(2)	O21-Pr1-N2	61.95(6)
Pr1-O32	2.465(2)	O22-Pr1-N2	61.56(6)
Pr1-N1	2.6374(19)	O31-Pr1-O32	123.13(7)
Pr1-N2	2.6355(19)	O31-Pr1-N3	61.89(6)
Pr1-N3	2.642(2)	O32-Pr1-N3	61.30(7)

Details of the hydrogen bonding network in **3** and **4** are given in Figures 8g and 8h as well as Tables 3g and 3h. In complex **3**, hydrogen bonds of the type O-H···O assist in stabilisation of the crystal structure. These exist between hydrogens of the hydroxyl group of H_2pydm as donors and oxygens of the uncoordinated nitrates as acceptors, with H···O contacts in the range 1.84(3)-2.59(3) Å. In addition to these are C-H···O interactions that occur between the C-H moieties of the pyridyl rings and the oxygen atoms of the uncoordinated nitrates, as well as between the methylene hydrogen atoms of H_2pydm and the oxygen atoms of the uncoordinated nitrates.

In the crystal structure of **4**, hydrogen bonds of the O-H···Cl and O-H···O type are observed. These exist between the hydroxyl groups of H_2pydm with the chloride counter-anions and the oxygen atom of the uncoordinated DMF molecule. The hydrogen bond distance between the hydroxyl hydrogen atom and the DMF oxygen atom (H12A···O4 = 1.79(3) Å) is relatively shorter, and thus stronger, compared to the bonds between the hydrogen atom of the hydroxyl group and the chlorides (H···Cl = 2.13(3)–2.26(3) Å). In addition, C-H···Cl and C-H···O contacts also exist. The former are supported by the hydrogen atoms of the methylene group of H_2pydm and the

=CH- group of DMF to the chloride anion, while weak intramolecular C-H···O interactions occur in DMF.

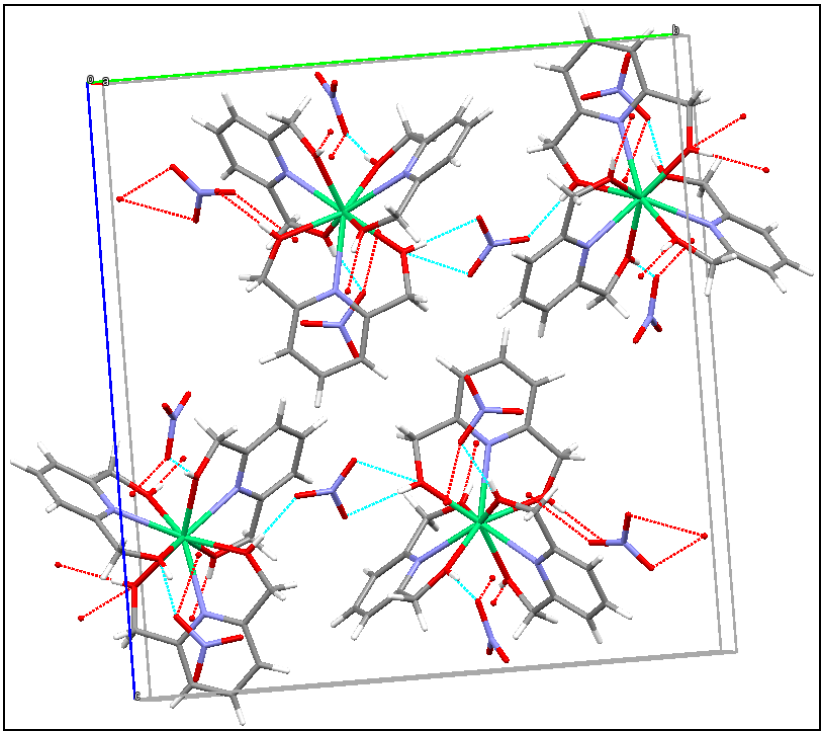

Figure 8g: Hydrogen bonding in complex **3** forming a 2D network.

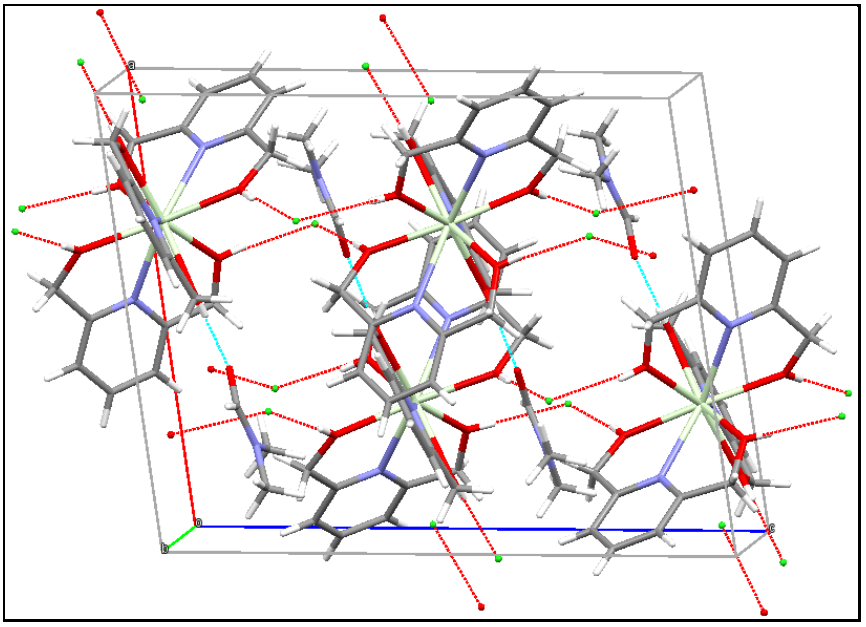

Figure 8h: Crystal packing in complex **4** showing hydrogen bonding.

Table 3g: Hydrogen bond geometry (Å, °) for complex **3**.

D*-H···*A	***D*-H**	**H···*A***	***D*···*A***	***D*-H···*A***
O(31)-H(31A)···O(63)	0.76(3)	1.84(3)	2.602(3)	178(4)
O(12)-H(12A)···O(42)	0.76(3)	2.59(3)	3.083(3)	125(3)
C(13)-H(13)···O(53)	0.9500	2.5200	3.328(4)	143.00
C(16)-H(16A)···O(61)	0.9900	2.4100	3.219(4)	138.00

Table 3h: Hydrogen bond parameters (Å, °) for complex **4**.

D*-H···*A	***D*-H**	**H···*A***	***D*···*A***	***D*-H···*A***
O(11)-H(11)···Cl(1)	0.84(3)	2.13(3)	2.961(2)	170(3)
O(12)-H(12A)···O(4)	0.79(3)	1.79(3)	2.570(3)	177(4)
O(21)-H(21)···Cl(2)	0.74(3)	2.26(3)	2.977(2)	166(3)
O(22)-H(22A)···Cl(2)	0.73(3)	2.24(3)	2.968(2)	172(3)
O(31)-H(31)···Cl(3)	0.79(3)	2.17(3)	2.951(2)	174(3)
O(32)-H(32A)···Cl(3)	0.78(3)	2.20(3)	2.968(2)	170(3)
C(26)-H(26B)···Cl(1)	0.9900	2.7600	3.579(3)	140.00
C(36)-H(36B)···Cl(2)	0.9900	2.7800	3.626(3)	143.00
C(37)-H(37B)···O(4)	0.9900	2.5700	3.151(3)	118.00
C(41)-H(41)···Cl(3)	0.9500	2.6600	3.556(3)	157.00
C(42)-H(42A)···O(4)	0.9800	2.3400	2.759(4)	105.00

To get insight into a correlation between atomic number and Ln-O and Ln-N bond lengths, the previously reported $[Sm(H_2pydm)_3](NO_3)_3$ complex can be considered [1]. The average Ln-O and Ln-N bond distances for this complex were found to be 2.434 and 2.580 Å, respectively.

Figure 8i illustrates the influence of the lanthanide contraction: there is a decrease in the Ln-O and Ln-N bond lengths upon going from Pr to Er, with a more linear decrease observed for the Ln-N bonds, and a rapid decrease in Ln-O bond lengths. Due to the lanthanide contraction, it is expected that as the ionic radius decreases, the

Ln-N and Ln-O bonds will contract uniformly within the coordination sphere [36]. It is also observed that the Ln-O bond lengths are shorter than their Ln-N counterparts as is expected for a hard oxygen-donor coordinated to a lanthanide ion.

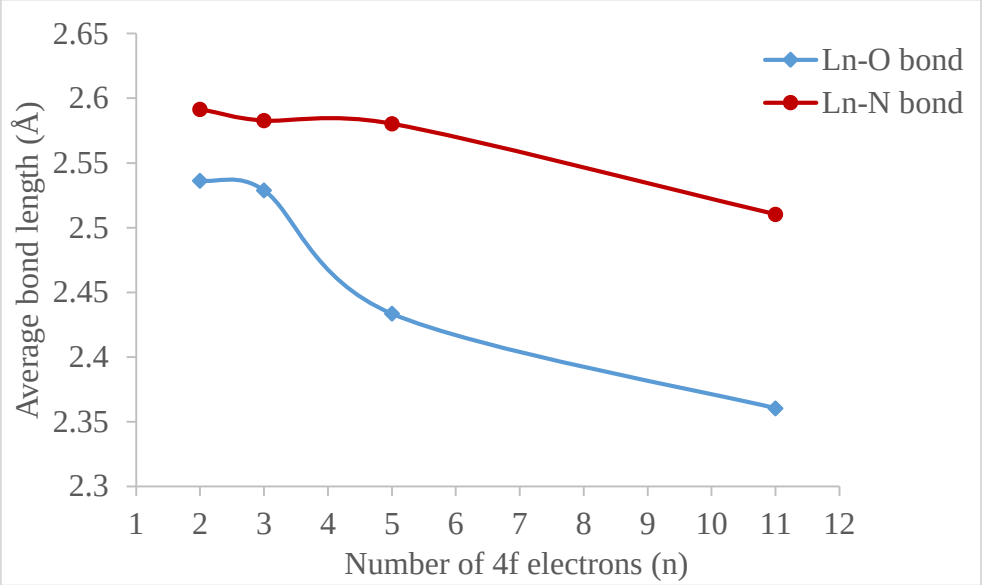

Figure 8i: Graph of average Ln-O and Ln-N bond distances *versus* the number of 4*f* electrons (*n*) for the coordinating oxygen and nitrogen atoms in Pr(III), Nd(III), Sm(III) and Er(III) nitrate complexes.

3.3.6 Thermal analysis

According to the TG (thermogravimetric analysis) curve given in Figure 9a **1** decomposes *via* three stages. The first weight loss of 51.95% (calculated value = 46.00%) from 180-205 ºC corresponds to the release of two coordinated H_2pydm molecules. The second and third weight losses of about 17.19% were observed between 409 ºC and 513 ºC, which may be due to the release of two nitrate molecules to give a thermally stable oxide. The TG curve is supported by the DTG (differential thermogravimetric analysis) curve showing a peak at 205 ºC, and two peaks that are not clearly visible between 409-513 ºC.

The heat flow curve shows three peaks, thus confirming a three-stage decomposition process.

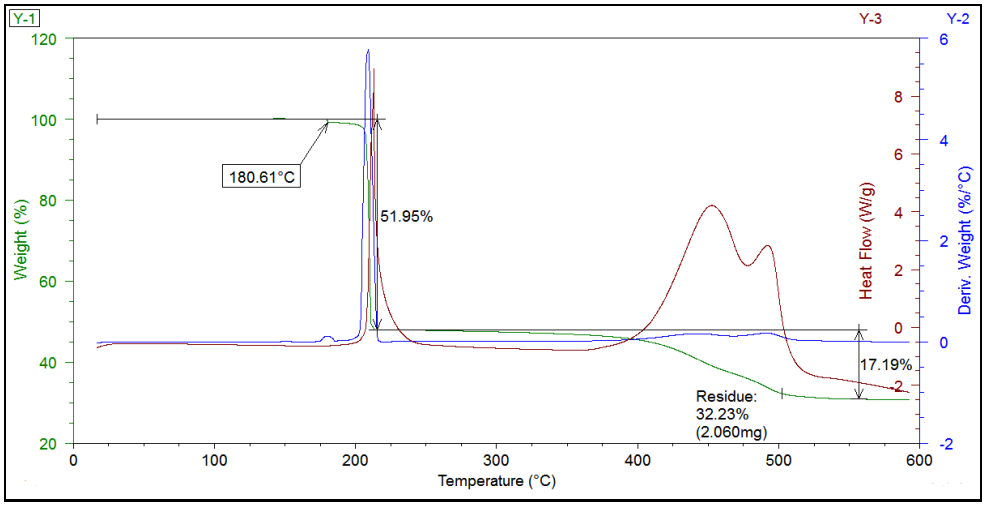

Figure 9a: TG-DTG and DTA curves of $[Pr(H_2pydm)_2(NO_3)_2](NO_3)$ (**1**).

From the TG and DTA (differential thermal analysis) curves of the Nd(III) complex in Figure 9b, it is seen that a multi-step decomposition pathway is followed. Thermogravimetric analysis indicates that the complex is stable up to 202.73 ^oC but at higher temperatures, mass loss occurs as evidenced by the irregular pattern of the curves. The first mass loss of 51.33% (calculated value = 45.77%) is assigned to the loss of two H_2pydm molecules. Mass loss starts at a slightly higher temperature than the Pr(III)-pydm complex (180.61 ^oC), hence the Nd(III) complex is more stable. A less rapid percentage mass loss is observed from 418 ^oC (the point at which decomposition of the two nitrates starts).

According to the heat flow curve, the complex decomposes *via* four stages, as shown by the four peaks with maxima at 212 ^oC, 462 ^oC, 520 ^oC and 584 ^oC. The first peak is associated with the initial step of decomposition in TG.

The investigated complexes **3** and **4** decompose in different ways as shown in Figures 9c and 9d, respectively. The recorded TG curve of complex **3** shows a plateau up to 154.07 ^oC, thus showing stability up to this point. As the temperature is increased, the first stage of mass loss occurs in a narrow temperature range (154.07-164.00 ^oC), followed by a weight loss of 24.06% in a wider temperature range. The two stages of decomposition are accompanied with the two peaks on the DTG curve with maxima at

157 and 192 °C, and each step could be attributed to the loss of one H_2pydm molecule (calculated value = 18.86%).

Figure 9d shows the thermal analysis of complex **4** carried out from room temperature to 320 °C. The first mass loss between 130 °C and 220 °C corresponds to the loss of DMF solvent molecules [39]. Thermal degradation continued through an additional step as also evidenced by one peak on the DTG curve at 269.24 °C. The second mass loss is attributed to the loss of two coordinated H_2pydm ligands from the complex. The mass losses calculated from the TG curve, *viz.* 6.54% and 43.99%, deviate slightly from the theoretical values of 9.91% and 37.72%.

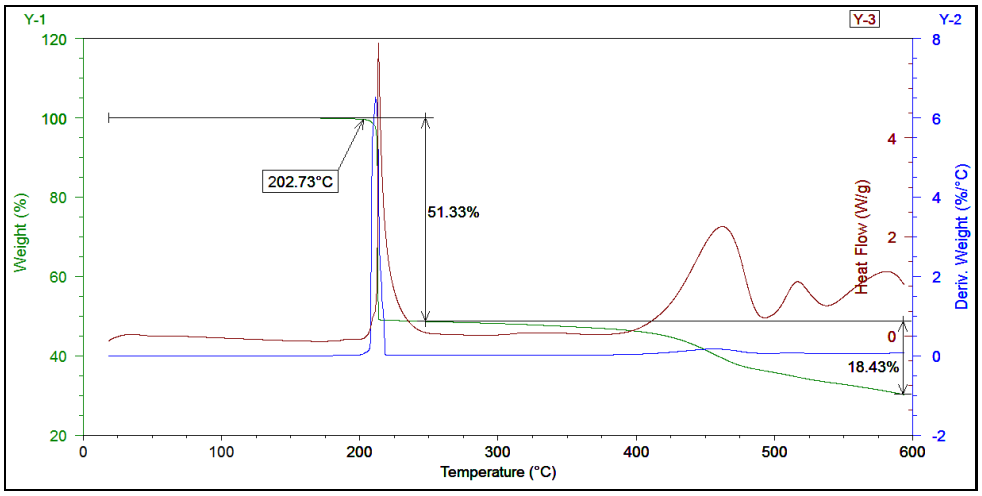

Figure 9b: TG-DTG and DTA curves of $[Nd(H_2pydm)_2(NO_3)_2](NO_3)$ (**2**).

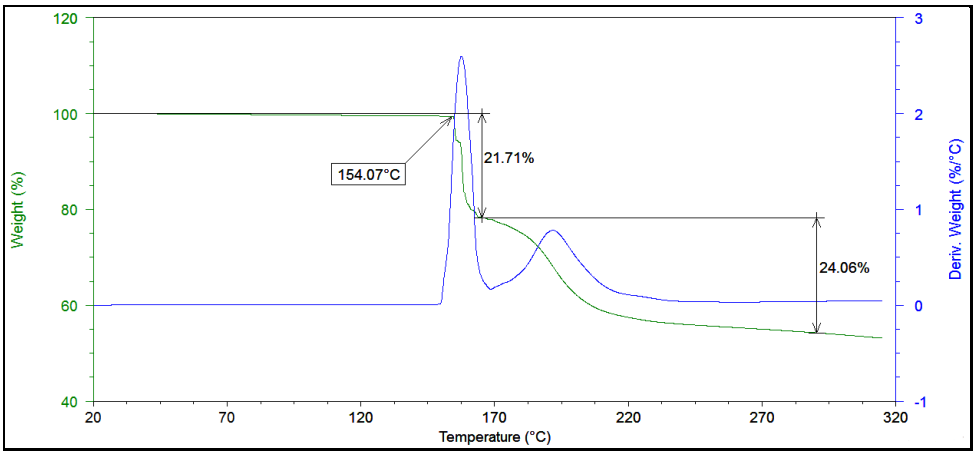

Figure 9c: TG-DTG curves of $[Er(H_2pydm)_3](NO_3)_3$ from room temperature to 320 °C.

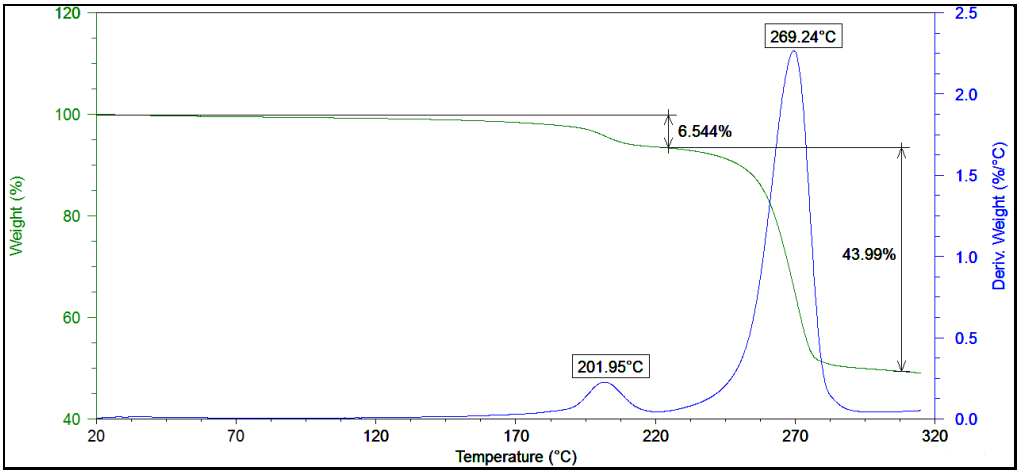

Figure 9d: TG-DTG curves of complex **4** from room temperature to 320 ^{o}C.

3.3.7 Cyclic voltammetry

The redox behaviour of the Ln(III) complexes has been investigated by cyclic voltammetry using 0.10 M tetrabutylammonium perchlorate (TBAP) as supporting electrolyte at a scanning rate of 200 mVs^{-1}. The plots in Figures 10a-10c give the cathodic peak potentials (E_p^c) at approximately -1.086, -1.158 and -1.364 V *versus* Ag/Ag^+ for complexes **1**, **2** and **4**, respectively. This is due to the reduction of Ln(III) to Ln(II) for the Pr(III) and Nd(III) complexes [40,41]. For the Er(III) complex, the peak potential shifts to -2.203 V.

There is a less energetic difference between electron configurations $4f^{n-1}6s^25d^1$ and $4f^n6s^25d^0$, and for this reason the lanthanides are likely to form meta-stable or stable divalent states. Formation of the +2 oxidation state occurs especially in non-oxidising environments or some particular organic solvents; Nd is one of the lanthanides that has been investigated and found to show this behaviour. Stabilisation of the +2 oxidation state is ascribed to the lowering of the energy of a *d*-orbital resulting from crystal-field splitting in the ligand-field and the contribution of *d*-electrons in chemical bonding [41,42]. It can therefore be concluded that the voltammetric behaviour of these complexes is similar since the site and shape of the peaks are analogous. The active centre is Ln(III) and the electrochemical process is assigned to the one-electron reduction process.

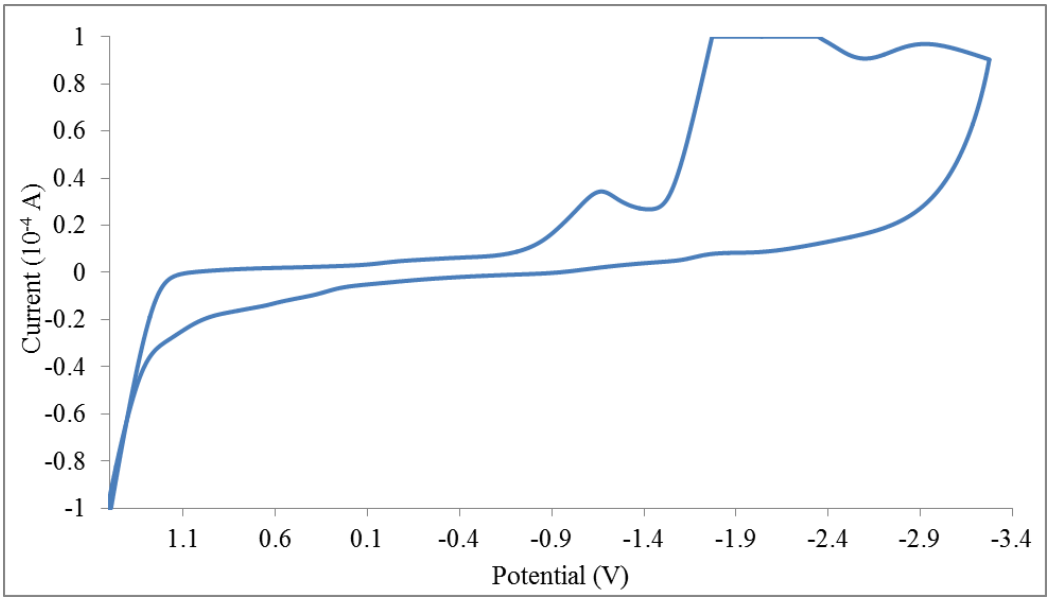

Figure 10a: Cyclic voltammogram of a DMF solution of complex **1** (8.26 mM).

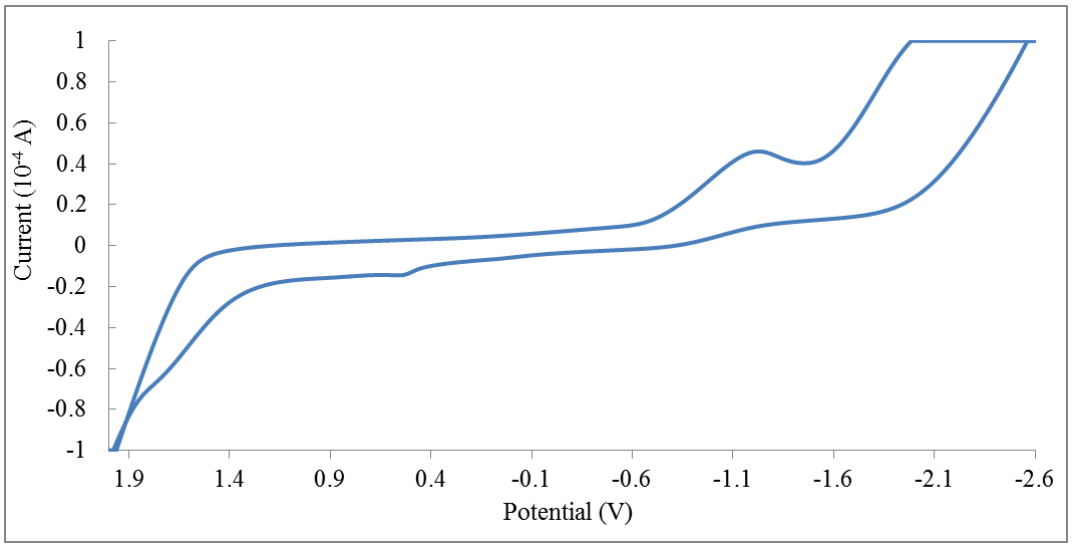

Figure 10b: Cyclic voltammogram of a methanolic solution of complex **2** (8.22 mM).

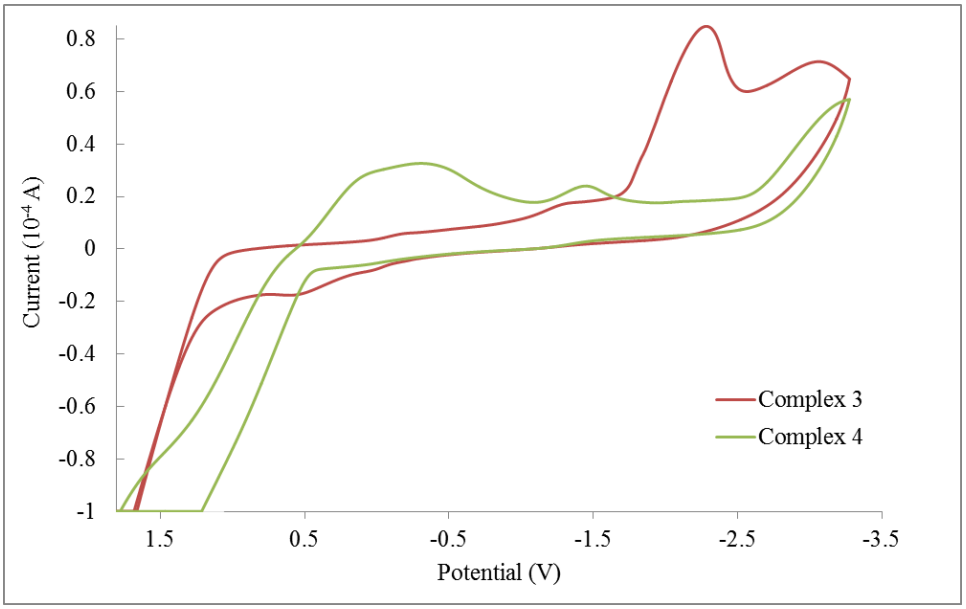

Figure 10c: Cyclic voltammetry curves of DMF solutions of complexes **3** (3.25 mM) and **4** (3.39 mM).

3.4 Conclusion

Conductivity measurements of $[Ln(H_2pydm)_2(NO_3)_2](NO_3)$ (Ln = Pr or Nd), $[Er(H_2pydm)_3](NO_3)_3$ and $[Pr(pydm)_3](Cl)_3$ in dimethylformamide indicate the ionic nature of these species. Hence it is confirmed that not all three nitrate groups and chlorides are present inside the coordination sphere.

The ligand H_2pydm has proved to be a neutral *O,N,O*-donor chelate for complexation of the light lanthanides Pr and Nd, and the heavier lanthanide Er. The investigation of the coordination behaviour of H_2pydm with the chloro- and nitro-derivatives of the metal using different solvent systems led to the isolation of four crystalline complexes containing nitrate or chloride counter-ions. Complexes **1** and **2** are ten-coordinate while complexes **3** and **4** are nine-coordinate. Complex **4** has one DMF molecule per formula unit that is not involved in metal coordination but plays a role in hydrogen bonding in the complex. Complexes **1** and **2** displays a novel configuration while complexes **3** and **4** exhibit the same coordination mode as the previously isolated Sm(III) complex. Nevertheless, no previous studies on H_2pydm were performed with $LnCl_3 \cdot xH_2O$.

3.5 Crystallographic data

Table 4a: Crystal and structure refinement data for complexes **1** and **2**.

Formula	$C_{14}H_{18}N_4O_{10}PrNO_3$	$C_{14}H_{18}N_4O_{10}NdNO_3$
M_r (g.mol^{-1})	605.24	608.57
Crystal system	Triclinic	Triclinic
Space group	P-1	P-1
a, *b*, *c* [Å]	6.7623(3), 11.6893(5), 14.3589(6)	6.7588(3), 11.6829(6), 14.3513(6)
α, β, γ (°)	67.850(1), 89.772(1), 75.237(1)	67.897(2), 89.721(2), 75.225(2)
V (Å^3)	1011.16(8)	1009.95(8)
Z	2	2
ρ (mg.m^{-3})	1.988	2.001
μ (mm^{-1})	2.491	2.652
F(000)	600	602
Crystal size (mm)	0.08 × 0.24 × 0.43	0.07 × 0.15 × 0.53
Temperature (K)	200	200
Mo *Kα* radiation, λ (Å)	0.71073	0.71073
θ (min-max) (°)	2.0, 28.4	2.0, 28.3
Data set	-9≤*h*≤8; -15≤*k*≤15; -19≤*l*≤19	-9≤*h*≤9; -15≤*k*≤15; -19≤*l*≤19
Tot., Unique data, R_{int}	27384, 5032, 0.021	26976, 5016, 0.022
Observed [I>2σ(I)] reflections	4846	4825
$N_{reflections}$, $N_{parameters}$	5032, 314	5016, 314
$R[F^2>2\sigma(F^2)]$, $wR(F^2)$, *S*	0.0142, 0.0319, 1.08	0.0144, 0.0345, 1.07
$\Delta\rho_{min}$, $\Delta\rho_{max}$ (e.Å^{-3})	-0.42, 0.36	-0.43, 0.44

Table 4b: Crystal and structure refinement data for complex **3**.

Formula	$C_{21}H_{27}ErN_3O_6$, 3(NO_3)
M_r (g.mol^{-1})	770.75
Crystal system	Monoclinic
Space group	$P2_1/n$
a, *b*, *c* [Å]	7.5534(3), 18.8042(7), 19.7720(8)
α, β, γ (°)	90, 93.949(1), 90
V (Å^3)	2801.66(19)
Z	4
ρ (mg.m^{-3})	1.827
μ (mm^{-1})	3.079
F(000)	1532
Crystal size (mm)	0.14 × 0.41 × 0.69
Temperature (K)	200
Mo *Kα* radiation, λ (Å)	0.71073
θ (min-max) (°)	1.5, 28.3
Data set	$-7 \leq h \leq 10$; $-25 \leq k \leq 23$; $-26 \leq l \leq 26$
Tot., Unique data, R_{int}	25949, 6944, 0.017
Observed [I>2σ(I)] reflections	6408
$N_{reflections}$, $N_{parameters}$	6944, 412
$R[F^2>2\sigma(F^2)]$, $wR(F^2)$, *S*	0.0210, 0.0473, 1.13
$\Delta\rho_{min}$, $\Delta\rho_{max}$ (e.Å^{-3})	-0.58, 1.55

Table 4c: Crystal and structure refinement data for complex **4**.

Formula	$C_{21}H_{27}N_3O_6PrC_3H_7NOCl_3$
M_r (g.mol^{-1})	737.81
Crystal system	Monoclinic
Space group	$P2_1/c$
a, *b*, *c* [Å]	12.7645 (3), 14.5898(3), 15.8367(4)
α, β, γ (°)	90, 98.680(1), 90
V (Å^3)	2915.51(12)
Z	4
ρ (mg.m^{-3})	1.681
μ (mm^{-1})	1.994
F(000)	1488
Crystal size (mm)	0.09 × 0.16 × 0.34
Temperature (K)	200
Mo *Kα* radiation, λ (Å)	0.71073
θ (min-max) (°)	1.9, 28.3
Data set	-16≤*h*≤17; -19≤*k*≤12; -20≤*l*≤21
Tot., Unique data, R_{int}	28378, 7240, 0.038
Observed [I>2σ(I)] reflections	5435
$N_{reflections}$, $N_{parameters}$	7240, 378
$R[F^2>2\sigma(F^2)]$, $wR(F^2)$, *S*	0.0282, 0.0554, 1.00
$\Delta\rho_{min}$, $\Delta\rho_{max}$ (e.Å^{-3})	-0.39, 0.53

Table 5: Abbreviations used in SHAPE analyses.

DP-10	Decagon
EPY-10	Enneagonal pyramid
OBPY-10	Octagonal bipyramid
PPR-10	Pentagonal prism
PAPR-10	Pentagonal antiprism
SDD-10	Staggered dodecahedron
TD-10	Tetradecahedron
HD-10	Hexadecahedron
EP-9	Enneagon
OPY-9	Octagonal pyramid
HBPY-9	Heptagonal bipyramid
CCU-9	Spherical-relaxed capped cube
CSAPR-9	Spherical capped square antiprism
TCTPR-9	Spherical tricapped trigonal prism
HH-9	Hula-hoop
MFF-9	Muffin

3.6 References

[1] D.R. van Staveren, G.A. van Albada, S. Gorter, J.G. Haasnoot and J. Reedijk, *Inorg. Chim. Acta*, **300-302** (2000) 1104.

[2] D.I. Alexandropoulos, L. Cunha-Silva, L. Pham, V. Bekiari, G. Christou and T.C. Stamatatos. *Inorg. Chem.*, **53** (2014) 3220-3221.

[3] T. Hamaguchi and I. Ando. *Inorg. Chim. Acta*, **427** (2015) 144-145.

[4] V.T. Yilmaz, S. Guney, O. Andac and W.T. Harrison, *J. Coord. Chem.*, **56** (2003) No. 1, pp. 21–32.

[5] S. Winter, W. Seichter and E. Weber, *Z. Anorg. Allg. Chem.*, **630** (2004) 434.

[6] S. Winter, W. Seichter and E. Weber, *J. Coord. Chem.*, **57** (2004) 997.

[7] G.C. Vlahopoulou, D.I. Alexandropoulos, C.P. Raptopoulou, S.P. Perlepes, A. Escuer and T.C. Stamatatos, *Polyhedron* , **28** (2009) 3235.

[8] I. Ucar, O. Tamer, B. Sariboga and O. Buyukgungor, *Solid State Sciences*, **15** (2013) 7.

[9] N. Farfan and H. Hopfl, *Heteroat. Chem.*, **9** (1998) 377.

[10] A. Klein, S. Elmas and K. Butsch, *Eur. J. Inorg. Chem.*, (2009) 2271.

[11] R.J. Fites, A.T. Yeager, T.L. Sarvela, W.A. Howard, G. Zhu and K. Pang, *Inorg. Chim. Acta*, **359** (2006) 248.

[12] S. Onaka, L. Hong, M. Ito, T. Sunahara, H. Imai and K. Inoue, *J. Coord. Chem.*, **58** (2005) 1523.

[13] R.C. Mehrotra, P.N. Kapoor and J.M. Batwara, *Coord. Chem. Rev.*, **31** (1980) 69.

[14] X. Hua, Q. Pan, L. Yu, J. Xue, L. Yang, Y. Xu, G. Zhao, W. Li, Z. Wang, J. Wu, K. Liu and J. Chen, *J. Mol. Struct.*, **998** (2011) 225-232.

[15] Y. Su, L. Yang, X. Jin, S. Weng and J. Wu, *J. Mol. Struct.*, **616** (2002) 221-230.

[16] N.F. Curtis and Y.M. Curtis, *Inorg. Chem.*, **4** (1964) 804.

[17] P. Yan, W. Sun, G. Li, C. Nei, T. Gao and Z. Yue, *J. Coord. Chem.*, **60** (2007) 1973.

[18] K. Raja, A. Suseelamma and K.H. Reddy, *J. Iran Chem. Soc.*, **12** (2015) 1480.

[19] M.D. Regulacio, N. Tomson and S.L. Stoll, *Chem. Mater.*, **17** (2005) 3114.

[20] X. Chen, G.S. Goff, B.L. Scott, M.T. Janicke and W. Runde, *Inorg. Chem.*, **52** (2013) 3223.

[21] N. Guskos, J. Majszczyk, J. Typek, G. Zolnierkiewicz, E. Tomaszewicz and K. Aidinis, *Rev. Adv. Mater. Sci.*, **23** (2010) 98-99.

[22] K.A. Thiakou, V. Nastopoulos, A. Terzis, C.P. Raptopoulou and S.P. Perlepes, *Polyhedron*, **25** (2006) 547.

[23] P. Martin-Ramos, M. Ramos-Silva, F. Lahoz, I.R. Martin, P. Chamorro-Posada, M.E.S. Eusebio, V. Lavin and J. Martin-Gil, *J. Photochem. and Photobio. A*: Chemistry, **292** (2014) 21.

[24] M. Vyas, G. Chawla and H. K. Pandey, *Int. J. Chem. Sci.*, **8** (2010) 2758.

[25] P. Pitchaimani, K. Mun Lo and K.P. Elango, *J. Coord. Chem.* **68** (2015) 2174.

[26] M.D. Regulacio, M.H. Pablico, J.A. Vasquez, P.N. Myers, S. Gentry, M. Prushan, S. Tam-Chang and S.L. Stoll, *Inorg. Chem.*, **47** (2008) 1517.

[27] A. Ruiz-Martnez and S. Alvarez, *Chem. Eur. J.*, **15** (2009) 7471.

[28] X. Wang, M. Zhu, J. Wang and L. Li, *Dalton Trans*., **44** (2015) 13890-13896.

[29] M. Llunell, D. Casanova, J. Cirera, P. Alemany and S. Alvarez, *SHAPE: Program for the Stereochemical Analysis of Molecular Fragments by Means of Continuous Shape Measures and Associated Tools, User's Manual Version 2.1*, 2013.

[30] K. Liu, H. Li, X. Zhang, W. Shi and P. Cheng, *Inorg. Chem.*, **54** (2015) 10224–10231.

[31] A.K. Boudalis, V. Nastopoulos, C.P. Raptopoulou, A. Terzis and S.P. Perlepes, *Z. Naturforsch*, **60b** (2005) 366.

[32] J.-H. Xue, X.-H. Hua, L.-M. Yang, W.-H. Li, Y.-Z. Xu, G.-Z. Zhao, G.-H. Zhang, K.-X. Liu, J.-E. Chen and J.-G. Wu, *Cryst. Eng. Comm.*, **16** (2014) 7720.

[33] L. Armelao, S. Quici, F. Barigelletti, G. Accorsi, G. Bottaro, M. Cavazzini and E. Tondello, *Coord. Chem. Rev.*, **254** (2010) 489.

[34] D. Guillaumont, *J. Mol. Struct.: THEOCHEM*, **771** (2006) 109–110.

[35] R.D. Hancock and A.E. Martell, *Chem. Rev.*, **89** (1989) 1875.

[36] S.A. Cotton, O.E. Noy, F. Liesener and P.R. Raithby, *Inorg. Chim. Acta*, **344** (2003) 39-40.

[37] W. Bell, P.I. Coupar, G. Ferguson and C. Glidewell, *Acta Cryst.*, **C52** (1996) 2522-2523.

[38] Z. RzalzynSka, W. Brzyska, R. Mrozek, W. Ozga and T. Glowiak, *J. Coord. Chem.*, **43** (1998) 325.

[39] B. Cristovao and Z. Hnatejko, *J. Mol. Struct.*, **1088** (2015) 52.

[40] L. Chou and C.L. Hussey, *Inorg. Chem.*, **53** (2014) 5754.

[41] H. Yamana, B.G. Park, O. Shirai, T. Fujii, A. Uehara and H. Moriyama, *Journal of Alloys and Compounds*, **408–412** (2006) 66–67.

[42] N.B. Mikheev, L.N. Auerman, I.A. Rumer, A.N. Kamenskaya and M.Z. Kazakevich, *Russian Chem. Rev.*, **61** (1992) 990.

CHAPTER 4

Nd(III), Gd(III) and Ho(III) complexes with an *o*-vanillin derived Schiff base ligand

4.1 Introduction

Schiff base metal complexes that have been prepared and screened for antimicrobial activity include those of ligands derived from 2-hydroxy-3-methoxybenzaldehyde (*o*-vanillin) and *ortho*-substituted anilines. Studies on copper(II) complexes of these ligands revealed that the ligands are bidentate, coordinating *via* the imine nitrogen atom and the phenolic oxygen atom in a planar configuration. The antimicrobial studies performed on these compounds revealed higher activity for the *o*-vanillin derivatives compared to the salicylaldehyde-based ligands. In the example outlined in Figure 1, the synthesis of a Cu(II) Schiff base complex synthesised from the condensation of *o*-vanillin and 2-chloroaniline is illustrated [1].

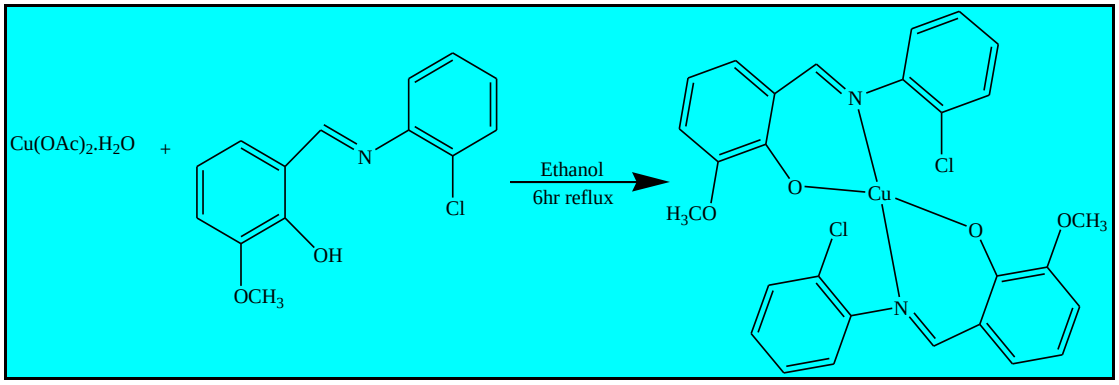

Figure 1: Synthesis of a Cu(II) complex from the *o*-vanillin derivative.

The reactions of the Schiff base ligand, 2-((*E*)-(1-hydroxy-2-methylpropan-2-ylimino)methyl)-6-methoxyphenol (H_2L_1, Figure 2) with the Ln(III) starting

materials, $Gd(NO_3)_3 \cdot 6H_2O$, $Ho(NO_3)_3 \cdot 6H_2O$ and $Nd(NO_3)_3 \cdot 6H_2O$ are reported in this chapter.

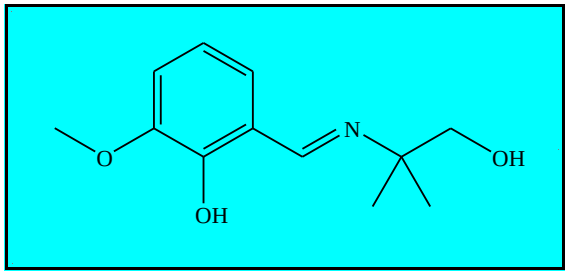

Figure 2: The structure of H_2L_1.

A zinc complex with H_2L_1 has previously been synthesised and characterised and its luminescent and magnetic behaviour has been evaluated. The crystal structure revealed that the monodeprotonated ligand acts in a tetradentate mode in the trinuclear Zn(II) complex, coordinating through the phenolate oxygen, the hydroxyl oxygen, the alkoxyl oxygen and the imino nitrogen. Bridging occurred in the complex through the phenolate oxygen atoms that interconnected the three Zn(II) ions (Figure 3) [2]. Each metal centre is hexacoordinated and exhibit significant distortion from octahedral geometry.

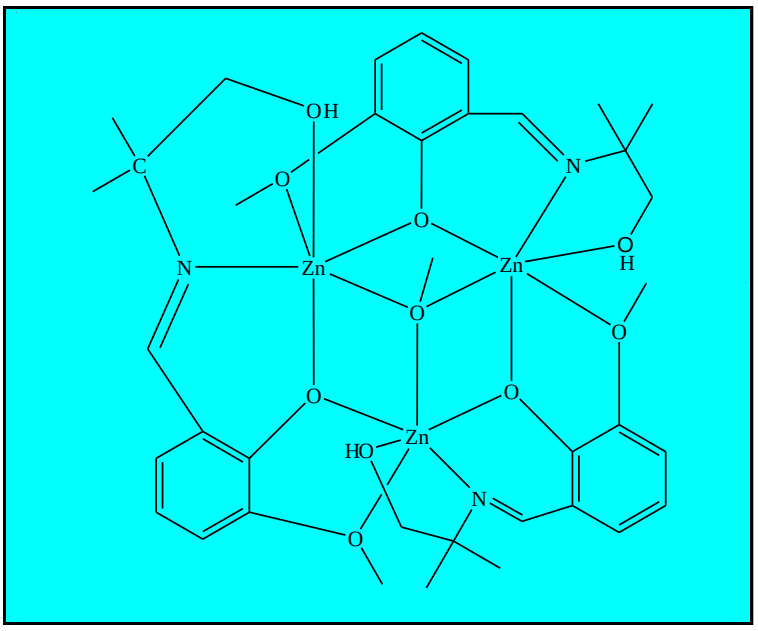

Figure 3: Structure of the trinuclear Zn(II) complex. The two perchlorate counter-ions are omitted for clarity.

4.2 Synthesis of the complexes

4.2.1 Synthesis of $Gd(H_2L_1)_2(NO_3)_3$ 1

To a 15 mL methanolic solution of H_2L_1 (0.345 g, 1.55 mmol) was added $Gd(NO_3)_3{\cdot}6H_2O$ (0.246 g, 0.545 mmol). The resulting mixture was stirred continuously for 30 minutes at room temperature, followed by filtration of the yellow solution to dispose of undissolved material. Yellow single crystals suitable for X-ray crystallography were grown within 3 days under vapour diffusion using diethyl ether. Yield = 35.9%, m.p. = 251.6-255.5 ^oC. Anal. Calcd. for $C_{24}H_{34}GdN_5O_{15}$ (%): C, 36.50; H, 4.34; N, 8.87. Found: C, 36.19; H, 4.09; N, 8.84. Conductivity (10^{-3} M, DMF): 124.9 $ohm^{-1}cm^2mol^{-1}$. UV-Vis (DMF, λ_{max} nm (ε, $M^{-1}cm^{-1}$)): 329 (4280), 420 (1490). IR (cm^{-1}): *ν*(N-H) 3495(w), $\nu_4(NO_3^-)$ 1550(s), $\nu_1(NO_3^-)$ 1299(m), $\nu_6(NO_3^-)$ 817(m), *ν*(Gd-O) 418(m).

4.2.2 Synthesis of $Ho(H_2L_1)_2(NO_3)_3$ 2

A similar procedure to that of **1** was adopted. Single yellow X-ray quality crystals were obtained from the reaction of H_2L_1 (0.321 g, 1.44 mmol) and $Ho(NO_3)_3{\cdot}6H_2O$ (0.226 g, 0.512 mmol). Yield = 33.8%, m.p. = 230.1-232.2 ^oC. Anal. Calcd. for $C_{24}H_{34}HoN_5O_{15}$ (%): C, 36.15; H, 4.30; N, 8.78. Found: C, 36.14; H, 4.18; N, 8.71. Conductivity (10^{-3} M, DMF): 134.4 $ohm^{-1}cm^2mol^{-1}$. UV-Vis (DMF, λ_{max} nm (ε, $M^{-1}cm^{-1}$)): 298 (1530), 334 (1330). IR (cm^{-1}): *ν*(N-H) 3495(w), $\nu_4(NO_3^-)$ 1550(s), $\nu_1(NO_3^-)$ 1299(m), $\nu_6(NO_3^-)$ 817(m), *ν*(Ho-O) 418(m).

4.2.3 Synthesis of $Nd(H_2L_1)_2(NO_3)_3$ 3

To a 10 mL methanolic solution of H_2L_1 (0.316 g, 1.42 mmol) was added a 5 mL methanolic solution of $Nd(NO_3)_3{\cdot}6H_2O$ (0.235 g, 0.536 mmol). The resulting mixture was stirred for 30 minutes at room temperature. Diethyl ether was allowed to diffuse slowly into the brown solution at room temperature. Badly twinned brown crystals were grown within 3 days. All attempts to produce reproducible X-ray data were

unsuccessful. Yield: 37.9%, m.p. = 235.0-237.8 ºC. Anal. Calcd. for $C_{24}H_{34}NdN_5O_{15}$ (%): C, 37.11; H, 4.41; N, 9.02. Found: C, 37.14; H, 4.38; N, 9.12. Conductivity (10^{-3} M, DMF): 154.5 $ohm^{-1}cm^2mol^{-1}$. UV-Vis (DMF, λ_{max} nm (ε, $M^{-1}cm^{-1}$)): 298 (2350), 370 (1980). IR (cm^{-1}): *v*(N-H) 3495(w), $v_4(NO_3^-)$ 1550(s), $v_1(NO_3^-)$ 1299(m), $v_6(NO_3^-)$ 817(m), *v*(Nd-O) 418(m).

4.3 Results and discussion

The same experimental protocol was followed in the preparation of the three complexes. $Ln(H_2L_1)_2(NO_3)_3$ (Ln = Gd, Ho or Nd) was prepared from the reaction of $Ln(NO_3)_3{\cdot}6H_2O$ with H_2L_1 in a 1:3 molar ratio in methanol. Crystals were obtained by vapour diffusion using diethyl ether. The general reaction is illustrated by the equation:

$$Ln(NO_3)_3{\cdot}6H_2O + 3H_2L_1 \xrightarrow[Et_2O]{\text{Methanol}} Ln(H_2L_1)_2(NO_3)_3$$

Ln = Gd, Ho, Nd

The reactions of several lanthanide(III) chloride hydrates with H_2L_1 in various solvents resulted in the formation of yellow solutions. However, no crystals were isolated.

4.3.1 Infrared spectroscopy

An overlay of the IR spectra of H_2L_1 and the complexes is shown in Figure 4. The broad band appearing in the 3675-3149 cm^{-1} region of the free ligand can be attributed to the O-H stretching vibrations. This band is indicative of the presence of an extensive hydrogen bonding network [3]. In the 3034-2805 cm^{-1} range is a series of weak bands which results from the C-H stretching of the ligand, while the vibrational band at 1438 cm^{-1} can be assigned to the C-H bending modes. The *v*(C=N), *v*(C-N) and *v*(C-O) bands are observed at 1635, 1229 and 1170 cm^{-1}, respectively.

Complexes **1-3** have identical IR spectra, with characteristic bands having similar shifts upon complexation from that of the free ligand – an indication of similar coordination compounds. The replacement of the broad *v*(O-H) in the IR spectrum of the free ligand, and subsequent appearance of the peak at 3495 cm^{-1} upon complexation confirms the N-H vibration in the $C=N^{+}$-H moiety of the ligand. This band shows that the hydrogen atom is still involved in intramolecular hydrogen bonding with the phenolate oxygen atom and this is in accord with previous observations of other rare-earth complexes of zwitterionic Schiff base ligands [4,5]. This is also further proof of proton migration from the phenolic group to the azomethine nitrogen atom. The C-H bending mode stretch in the free ligand is shifted to a slightly lower energy on complexation with Gd(III), Ho(III) and Nd(III), *viz.* 1432 cm^{-1} in **1** and 1428 cm^{-1} in **2** and **3**. The bands observed at 1550, 1299 and 817 cm^{-1} are ascribed to the vibrations of the coordinated nitrate groups. The separation of the two highest frequency bands (v_4-v_1) is approximately 251 cm^{-1}, which indicates η^2-chelation of the nitrate groups [5,6]. Formation of the Ln-O bonds is further confirmed by the appearance of bands at 418 cm^{-1} which is attributed to the *v*(Ln-O) [7].

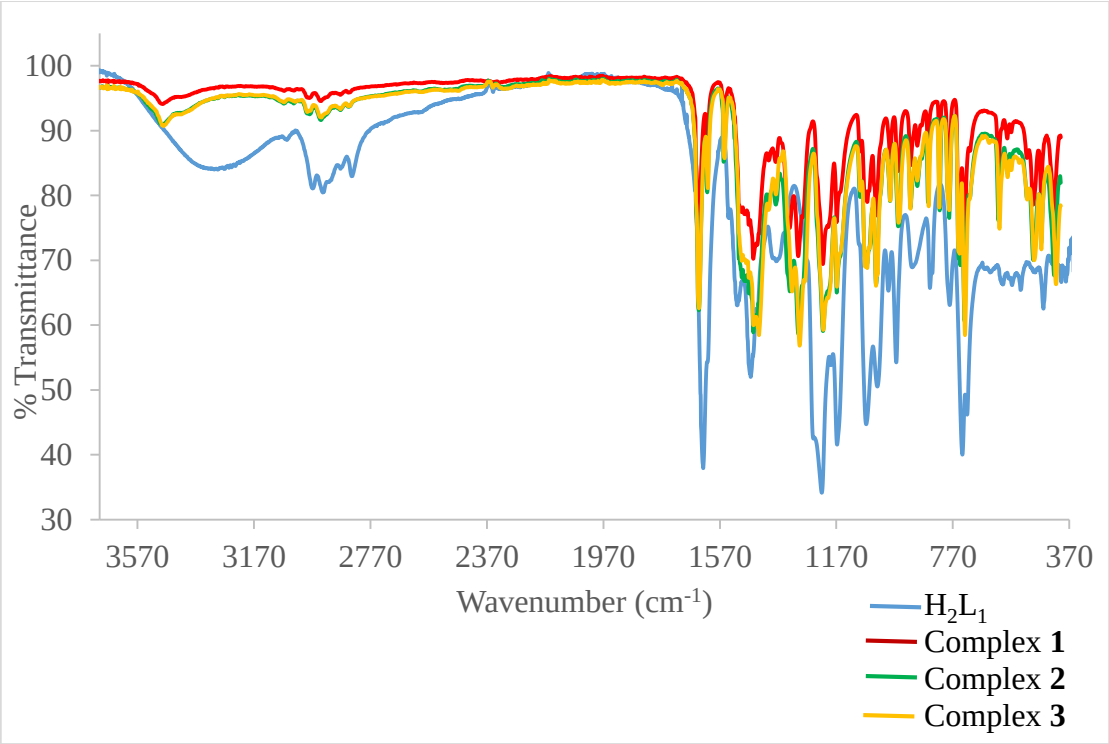

Figure 4: Overlay IR spectra of uncoordinated H_2L_1, **1**, **2** and **3**.

4.3.2 NMR analysis

The six proton singlet appearing at 1.26 ppm in the ^{1}H NMR spectrum of the free ligand (Figure 5a) is ascribed to the methyl protons, while the hydroxyl proton resonates at 2.08 ppm. The methylene protons and the phenolic proton singlet signals are found at 3.37 ppm and 3.51 ppm, respectively. A singlet observed at 3.78 ppm is due to the resonance of the methoxy protons while that at the highest chemical shift (δ = 8.20 ppm) arises from the resonance of the imino proton. The resonances of the aromatic protons are observed at δ = 6.58 ppm (triplet, 1H) and δ = 6.74 ppm (doublet, 2H).

Figures 5b-5d depicts the ^{1}H NMR spectra of **1**-**3** in DMSO-d_6. It is revealed that there is signal broadening in the spectra of complexes, with more intense broadening observed for the Gd(III) complex. These broader peaks were expected since the lanthanides under investigation are paramagnetic. Broadening of the signals is brought about by shortening of spin relaxation times [8].

When compared to the free H_2L_1, the resonances in the complexes show a downfield shift, with the greatest shift induced on the methoxy proton signals since they are located in the vicinity of the metal centre [9]. Upon coordination of the ligand to the metal, the formation of the Ln-O bonds results in a change in the environment of the protons. The presence of the lanthanide accounts for the decrease in the electron density and thus deshielding of these protons. As a result, the hydrogens resonate at lower field values. An insignificant shift is observed for the methyl protons relative to those of the free ligand. The detected chemical shifts are a result of the interactions of the relevant nuclear and electronic spins, with contributions mainly from through-space dipolar interactions than through-bond Fermi contact interactions [9-11]. Dipolar interactions are dependent on the position of the proton in space as well as on the magnetic anisotropy of the complex, whereas Fermi contact interactions are based on the nature of the covalent bonding network linking a given proton with the paramagnetic lanthanide.

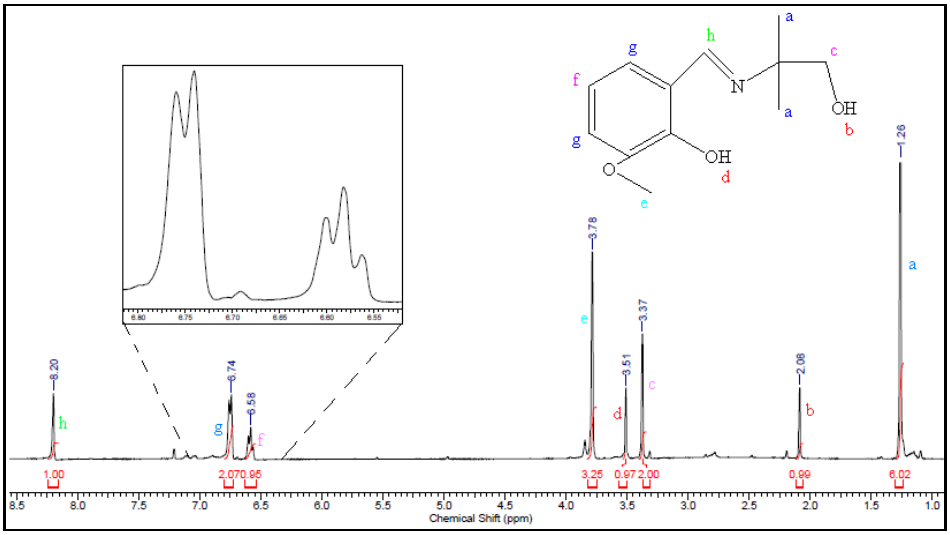

Figure 5a: Proton NMR spectrum of H_2L_1 in DMSO-d_6.

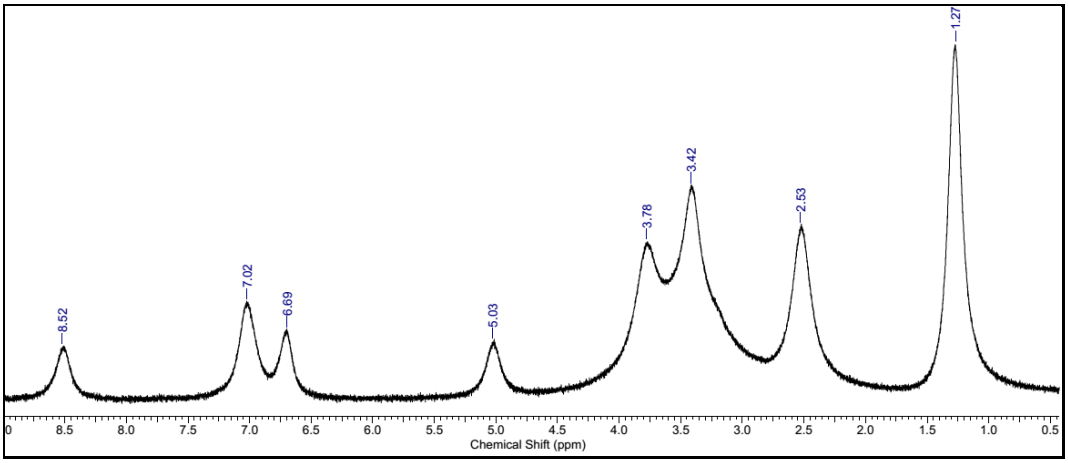

Figure 5b: The ^{1}H NMR spectrum of complex **1**.

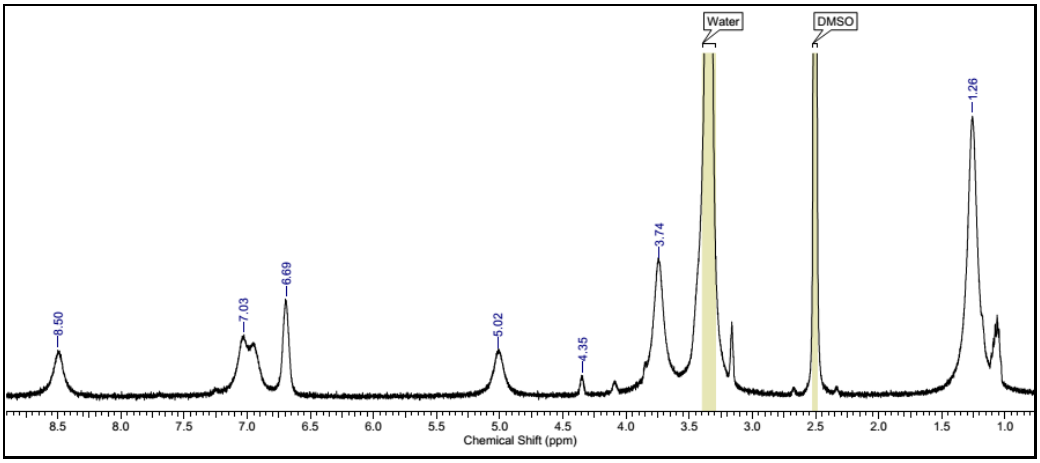

Figure 5c: ^{1}H NMR spectrum of complex **2**.

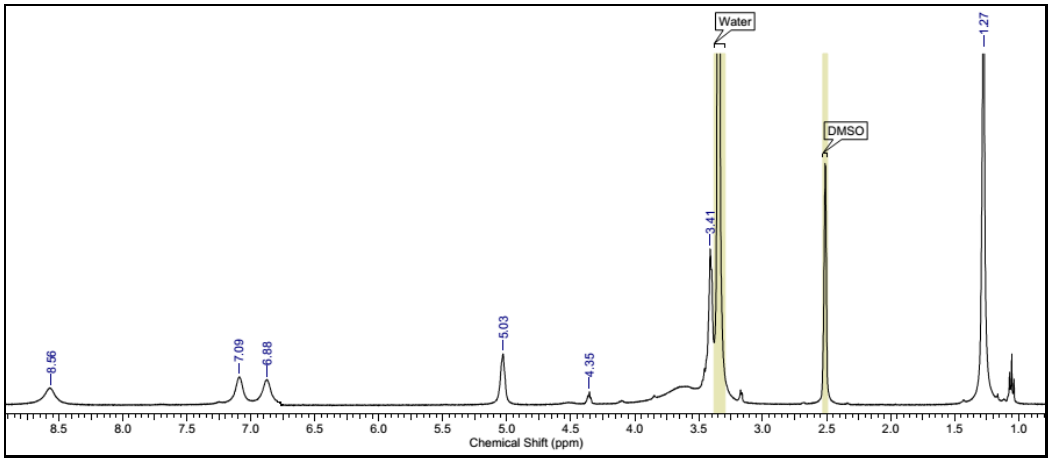

Figure 5d: Proton NMR spectrum of complex **3**.

4.3.3 UV-Vis spectroscopy

The electronic spectrum of the free ligand in the UV and visible region shows strong absorption peaks at 329 and 420 nm which are assigned to the π-π* and n-π* transitions, respectively [12]. The molar absorption coefficients of H_2L_1 are larger than those of complexes **1**-**3** which indicates ligand-centred solution absorption in the UV-Visible region (see Figure 6). There is no noticeable wavelength shift in the electronic spectrum of complex **1** relative to the free ligand, whereas absorptions are blue-shifted in complexes **2** and **3**. Higher energy absorptions are shifted by 31 nm while lower energy absorptions are blue-shifted by 86 and 50 nm upon coordination to Ho(III) and Nd(III), respectively. The shifts are attributed to the changes in energy levels of the ligand orbitals on coordination, and the latter can be a result of interelectronic repulsions between the 4*f* electrons [12,13].

4.3.4 Shape analysis

The coordination spheres of the Ln(III) ions in complexes **1** and **2** are given in Figures 7a and 7b respectively, with continuous shape measure (CShM) values listed in Table 1. The central Gd(III) and Ho(III) ions are bound to ten oxygen atoms in a tetradecahedron structure and the deviation parameters are 4.8273 and 4.7649,

respectively. The strength of ligand binding is probably responsible for the decrease in deviation parameters.

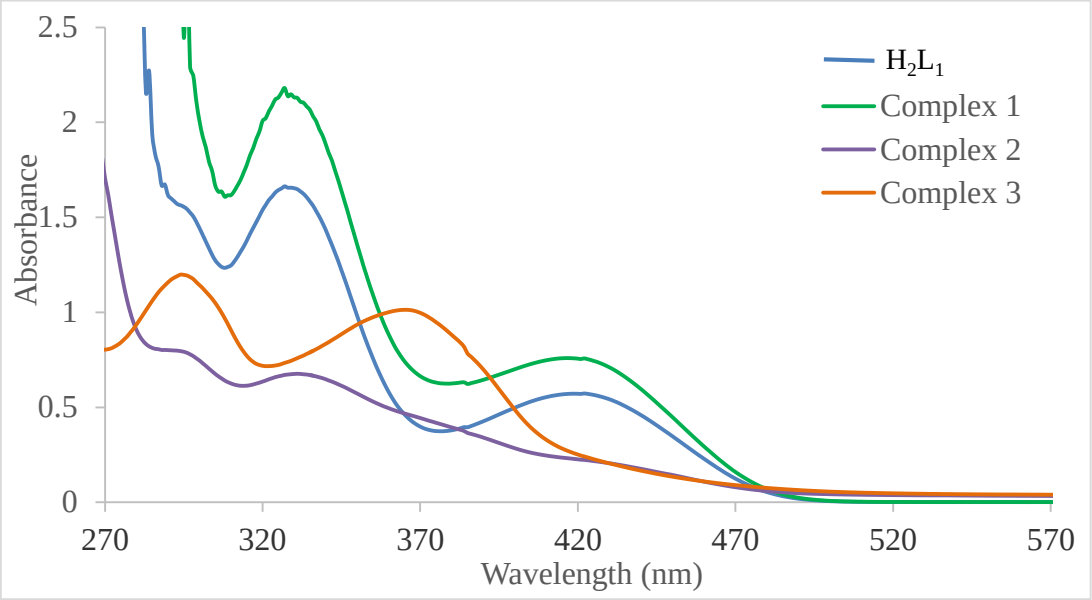

Figure 6: UV-Vis spectra of DMF solutions of H_2L_1 (6.25 x 10^{-5} M) and complexes **1-3** (5.10 x 10^{-4} M) at room temperature.

Table 1: CShM values for complexes **1** and **2**.

	DP-10	EPY-10	OBPY-10	PPR-10	PAPR-10	SDD-10	TD-10	HD-10
Gd(III)	34.3433	22.0157	16.4012	11.1501	13.9294	5.4730	**4.8273**	10.5900
Ho(III)	34.4753	22.1474	16.4074	11.2618	139733	5.4152	**4.7649**	10.3711

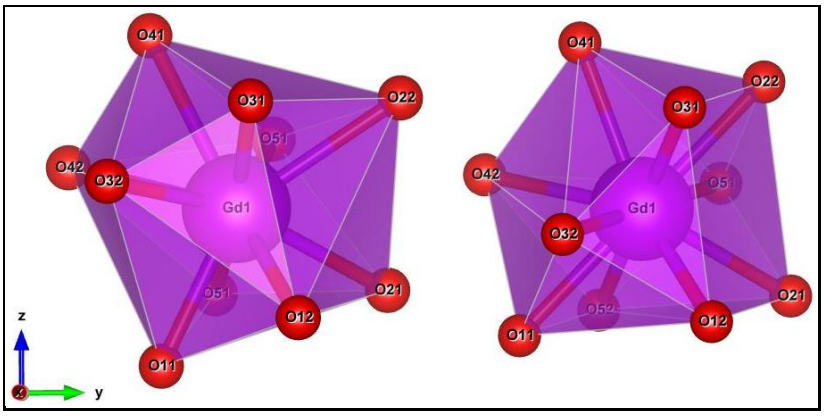

Figure 7a: Polyhedral view of the ten-coordinate Gd(III) complex (left) and the ideal TD-10 (right).

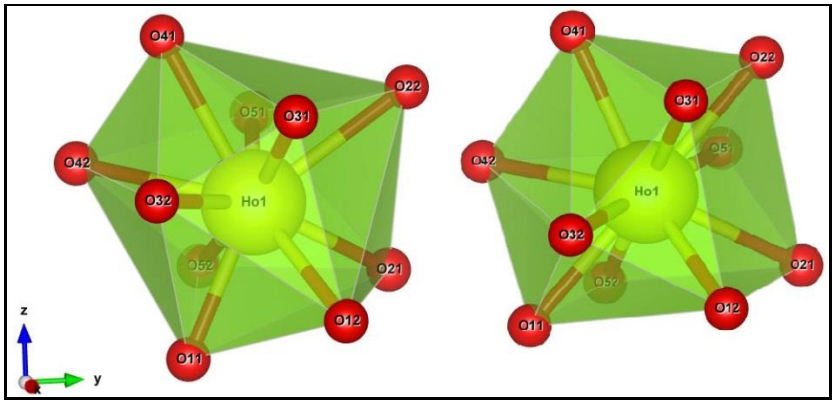

Figure 7b: The coordination sphere of Ho(III) (left) and the ideal TD-10 (right).

4.3.5 Crystal data

The single-crystal X-ray crystallographic studies reveal that complexes **1** and **2** are isostructural and crystallise in the monoclinic $P2_1/c$ space group. The Gd(III) and Ho(III) ions are both ten-coordinate with distorted tetradecahedron geometries. The crystal structures show that the lanthanide ions exist in the +3 oxidation state and the cationic charges are neutralised by three bidentately coordinated nitrate groups in each complex. Ten-coordination is achieved with four oxygen atoms originating from the methoxy sidearms and phenoxo groups of H_2L_1, and the remaining six oxygen atoms from three bidentate nitrato anions (Figures 8a and 8b). The Ln-O bonds involving the deprotonated phenol are shorter [range from 2.2502(15) to 2.3226(19) Å] than the Ln-$O_{methoxy}$ links that lie in the range 2.5352(16) to 2.582(2) Å. The Ln-$O_{nitrate}$ bonds vary from 2.4551(18) to 2.578(2) Å.

The average nitrate bite angles were found to be 50.61 and 51.27^o for complex **1** and **2**, respectively. It is also observed that the Ho(III) complex has larger ligand O-Ln-O bite angles compared to the Gd(III) complex. Therefore, ligand bite angles and ionic radii are correlated. There is an increase in bite angles as the ionic radii decreases. Relevant structural parameters are gathered in Table 2a.

Both H_2L_1 ligands remain protonated. However, proton migration occurred from the phenolic oxygen to the azomethine nitrogen atom to form a zwitterionic ligand as shown in Figure 8c.

The nitrogen atoms of the Schiff base ligand deviate from sp^2 hybridisation as supported by C-N-C bond angles that are larger than the ideal 120°, for example C(12)-N(1)-C(13) angles equals to 126.5(2) and 126.4(2)° in complexes **1** and **2**, respectively. The zwitterionic phenoxo-iminium ligand coordinates to the metal centres forming five-membered chelate rings with bite angles of approximately 64 and 65° for complexes **1** and **2**, respectively.

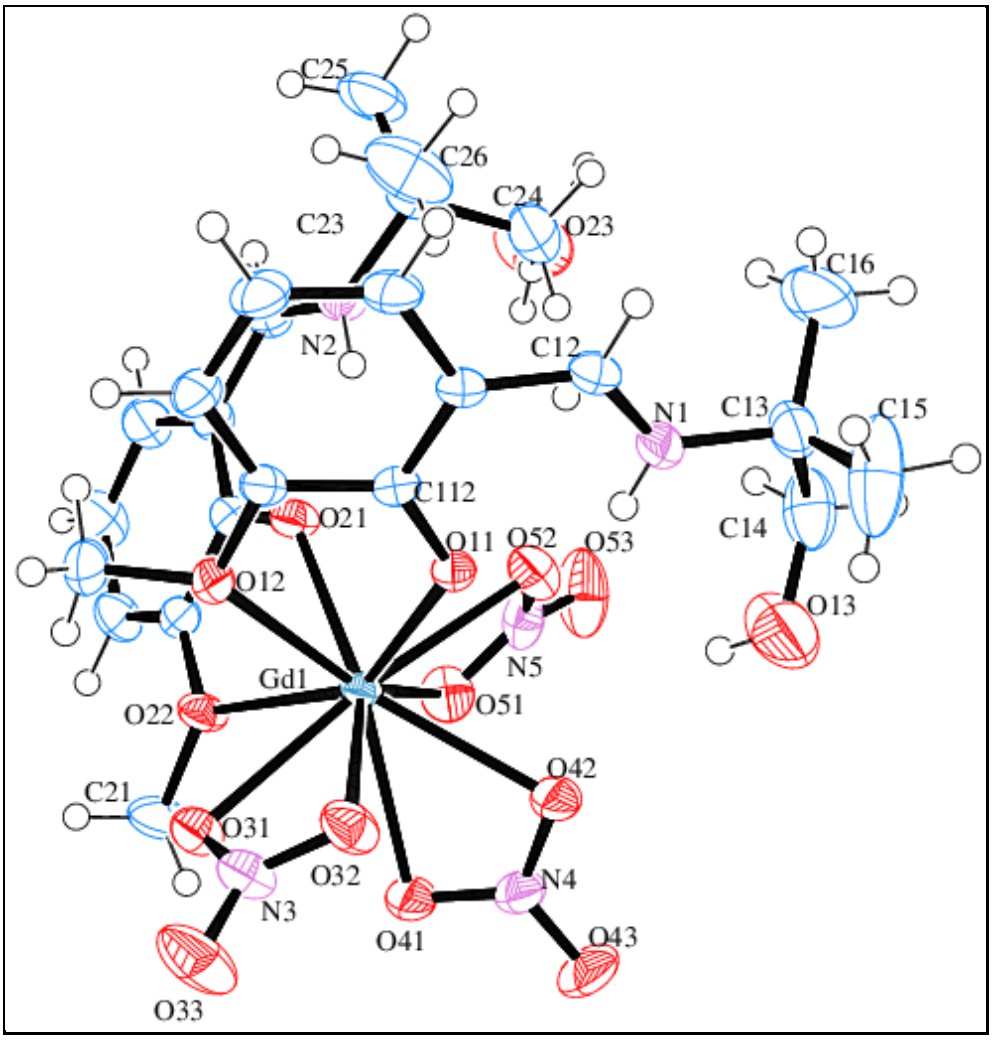

Figure 8a: ORTEP diagram (thermal ellipsoids at 50% probability) with a partial atom-numbering scheme for complex **1**.

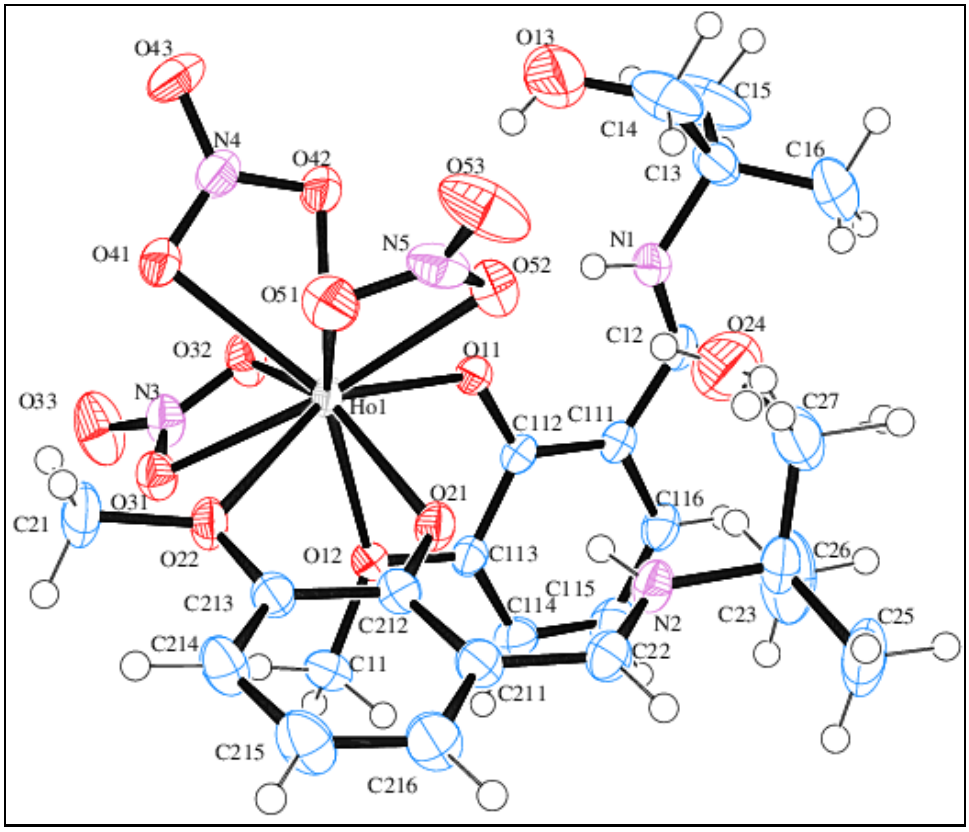

Figure 8b: ORTEP view of complex **2** showing 50% probability displacement ellipsoids and the atom-labelling.

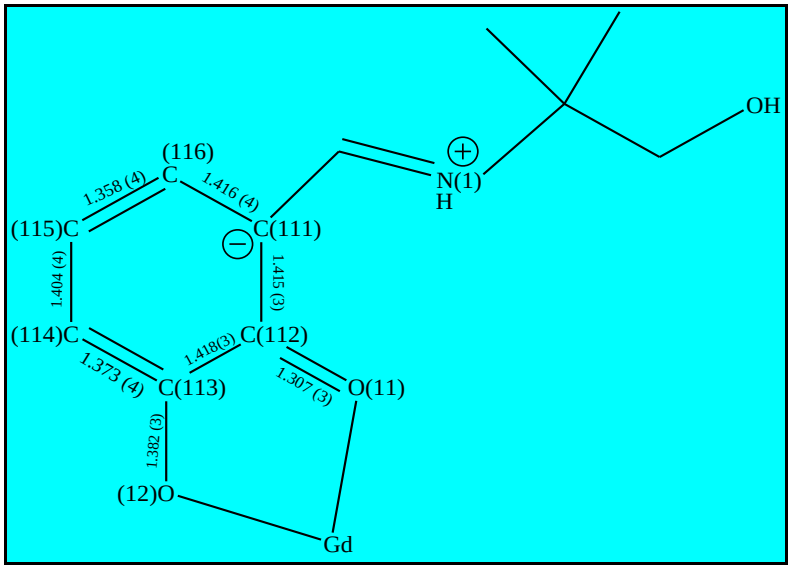

Figure 8c: Bidentate coordination of the ligand H_2L_1 in zwitterionic phenoxo-iminium form.

Table 2a: Selected bond lengths and angles in **1** and **2**.

1		**2**	
Bond lengths (Å)		**Bond lengths (Å)**	
Gd1-O11	2.2888(17)	Ho1-O11	2.2502(15)
Gd1-O12	2.5631(19)	Ho1-O12	2.5352(16)
Gd1-O21	2.3226(19)	Ho1-O21	2.2813(16)
Gd1-O22	2.582(2)	Ho1-O22	2.5482(16)
Gd1-O31	2.499(2)	Ho1-O31	2.4627(17)
Gd1-O32	2.514(2)	Ho1-O32	2.4693(18)
Gd1-O41	2.545(2)	Ho1-O41	2.5097(17)
Gd1-O42	2.510(2)	Ho1-O42	2.4648(18)
Gd1-O51	2.495(2)	Ho1-O51	2.4551(18)
Gd1-O52	2.578(2)	Ho1-O52	2.5671(18)
Bond angles (°)		**Bond angles (°)**	
O11-Gd1-O12	64.98(6)	O11-Ho1-O12	65.72(5)
O21-Gd1-O22	63.80(6)	O21-Ho1-O22	64.68(5)
O31-Gd1-O32	50.92(7)	O31-Ho1-O32	51.74(6)
O41-Gd1-O42	50.60(6)	O41-Ho1-O42	51.37(6)
O51-Gd1-O52	50.30(7)	O51-Ho1-O52	50.70(6)

The crystal packing in **1** and **2** is shown in Figures 8d and 8e, and the hydrogen bond geometries are given in Tables 2b and 2c. The crystal structures of the Gd(III) and Ho(III) complexes are stabilised by classical hydrogen bonds of the N-H···O and O-H···O type. The first kind of N-H···O hydrogen bonds are apparent between the azomethine hydrogen atom and the phenoxide of H_2L_1 which acts as the acceptor. The second kind of N-H···O hydrogen bonds is facilitated by the migrated proton attached to the azomethine which enables intramolecular hydrogen bonding with the terminal hydroxyl group of H_2L_1. Hydrogen bonds of the O-H···O type appear between the hydrogen atom on the terminal hydroxyl group of the Schiff base and the oxygen atom of the coordinated nitrate. The second kind of O-H···O interactions are supported

by the hydrogen atom of the hydroxyl group of one H_2L_1 ligand as the donor and the hydroxyl oxygen atom of another H_2L_1 as the acceptor.

In addition, weak C-H···O interactions participate in maintaining the crystal structure. Four kinds of these interactions exists, with the first kind maintained by one of the hydrogen atoms of the methoxy group as donor and the oxygen atom of the nitrate as acceptor, while the second kind is apparent between the azomethine hydrogen atom and the nitrate oxygen atom. Intramolecular interactions exist between one of the hydrogen atoms of the methyl group and the oxygen of the terminal hydroxyl group. Another kind of C-H···O contact is a result of weak interactions existing between the hydrogen atom (donor) of the methyl group and the nitrate oxygen atom.

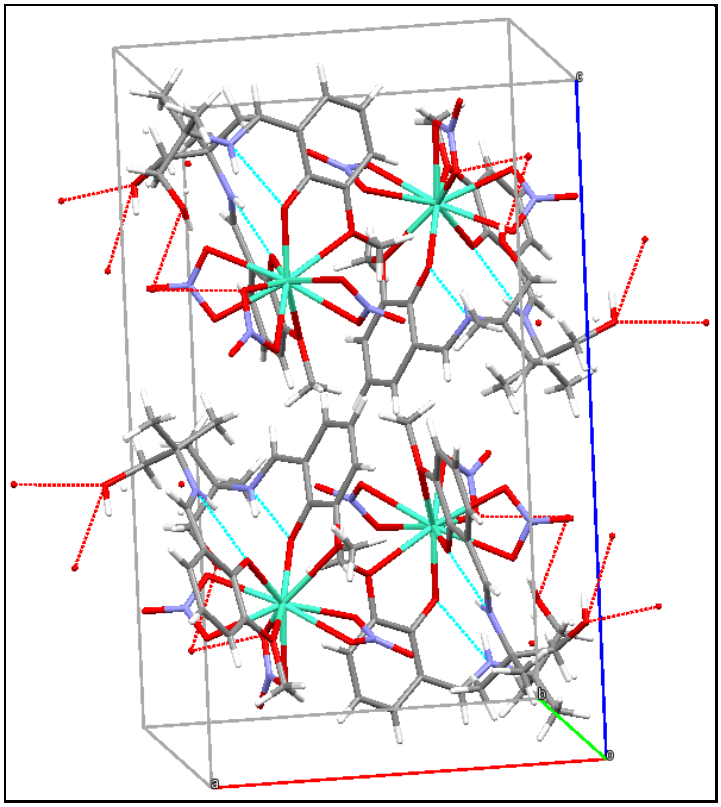

Figure 8d: Hydrogen bonding in complex **1**.

The correlation between Ln-O bond lengths or ligand bite angles and the number of 4*f* electrons is given by the plots in Figures 8f and 8g. The $Ln{-}O_{all}$ bond distances were obtained by averaging all Ln−O bonds in the coordination polyhedra of all metal

centres. These, together with the Ln-$O_{nitrate}$ and Ln-$O_{H_2L_1}$ bond lengths, were plotted to obtain evidence of the lanthanide contraction. As expected, the Ln-O bond lengths decrease in a linear fashion from Gd to Ho as the ionic radii decreases [14]. It is observed that the ligand bite angles are increasing as the number of 4*f* electrons increases, with a more linear graph observed for the nitrate angles.

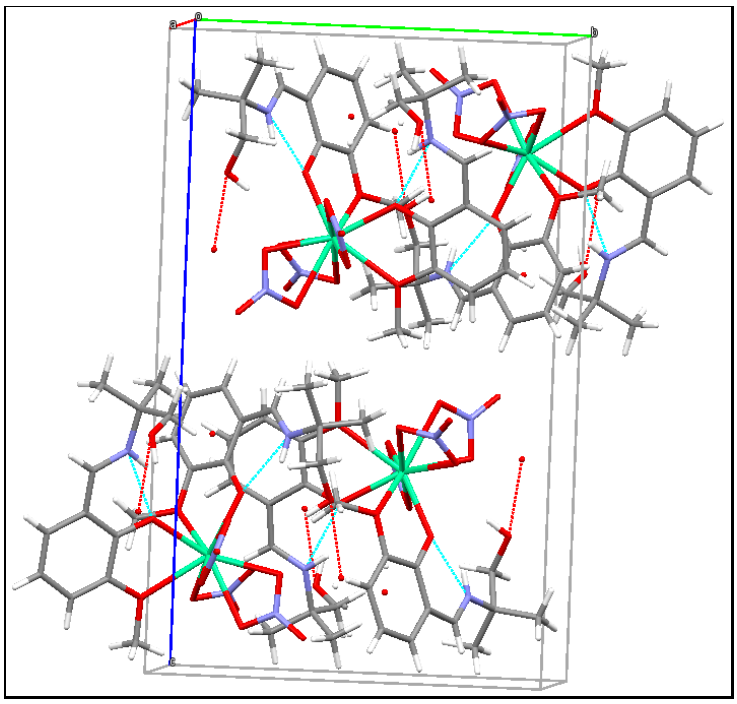

Figure 8e: Crystal packing in complex **2**.

Table 2b: Hydrogen bond geometry (Å, °) in complex **1**.

D*-H···*A	***D*-H**	**H···*A***	***D*···*A***	***D*-H···*A***
N(1)-H(1)···O(11)	0.83(4)	1.97(4)	2.640(3)	137(3)
N(1)-H(1)···O(13)	0.83(4)	2.40(4)	2.739(5)	105(3)
N(2)-H(2)···O(21)	0.89(4)	1.90(3)	2.635(3)	139(3)
O(13)-H(13)···O(42)	0.8400	2.4700	3.181(4)	143.00
O(23)-H(23)···O(13)	0.8400	2.0000	2.693(5)	139.00

D = donor, *A* = acceptor

Table 2c: Hydrogen bond parameters (Å, °) in complex **2**.

D*-H···*A	***D*-H**	**H···*A***	***D*···*A***	***D*-H···*A***
N(1)-H(1)···O(11)	0.80(3)	1.99(3)	2.633(3)	137(3)
N(1)-H(1)···O(13)	0.80(3)	2.43(3)	2.752(4)	106(2)
N(2)-H(2)···O(21)	0.86(3)	1.91(3)	2.632(2)	141(2)
O(13)-H(13)···O(42)	0.8400	2.4300	3.160(4)	146.00
O(13)-H(13)···O(52)	0.8400	2.5600	3.298(4)	147.00
O(23)-H(23)···O(13)	0.8400	2.0000	2.668(5)	135.00

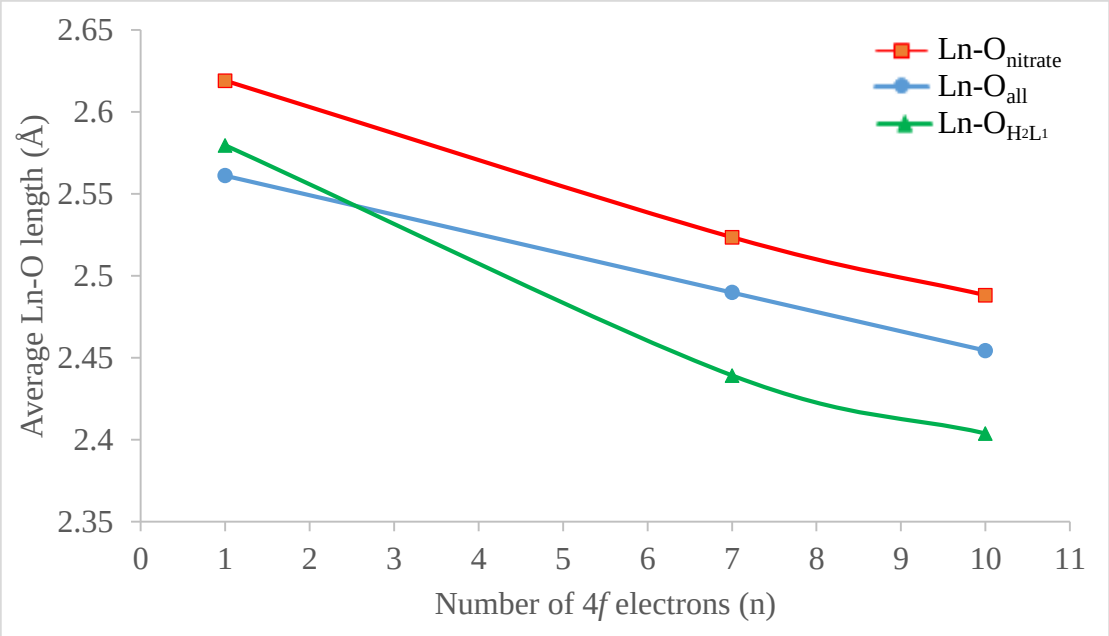

Figure 8f: Graph of mean Ln-O bond distances *versus* the number of 4*f* electrons.

4.3.6 Thermal analysis

The thermogravimetric analysis and differential thermogravimetric analysis (TG-DTG) curves of complexes **1-3** are shown in Figures 9a-9c. Complex **1** is stable, showing a TG plateau up to about 244-248 ^{o}C. This may indicate the absence of solvent molecules or water in the coordination environment of the rare-earth

compound [15]. Degradation then starts occurring from 248 ºC and peaks at 265.16 ºC as shown on the derivative curve.

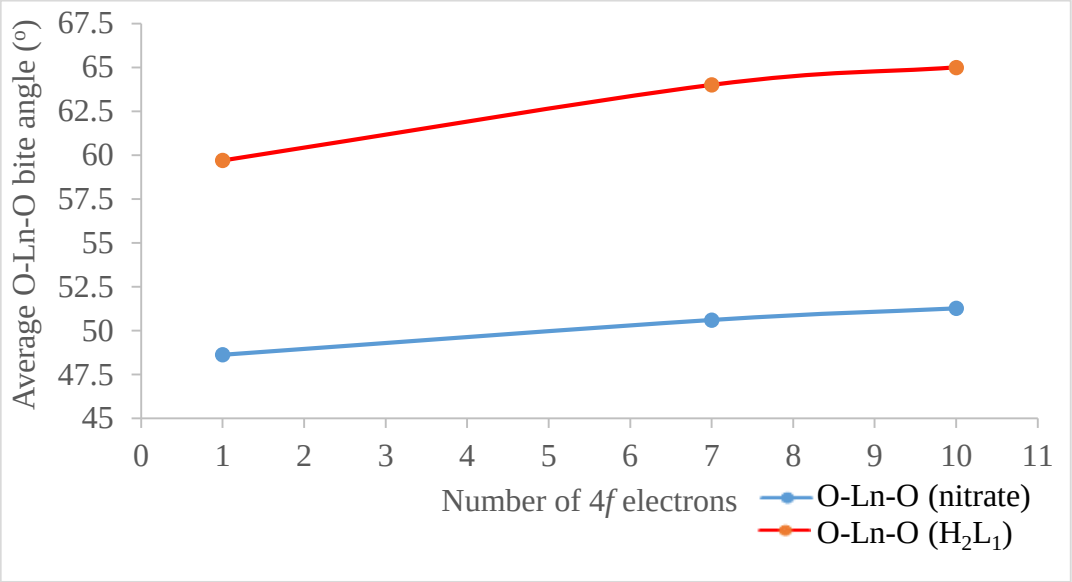

Figure 8g: Plot of average O-Ln-O ligand bite angles *versus* the number of 4*f* electrons.

For **2** and **3**, first mass losses of 1.53% and 2.25% are observed respectively, that could be attributed to loss of moisture from the samples. For complex **2**, the weight loss (7.52%) at the second step (170-173 ºC) with T_{DTG} at 171 ºC is assigned to the release of one coordinated nitrate ligand from the complex (calculated = 7.77%). The complex then shows stability until reaching 213 ºC, the temperature at which degradation continues.

The Nd(III) complex is seen to decompose in a different way from the Ho(III) complex. As the temperature is increased, the TG curve of complex **3** exhibits weight loss (36.40%) in a wider temperature range (230-314 ºC) which may be due to the decomposition of one H_2L_1 and one nitrate molecule. This is in agreement with the theoretical (calculated) loss of 36.72%. Inspection of the DTG curve shows that this weight loss follows a two-step decomposition pathway as shown by the two peaks at 270.45 and 288.65 ºC.

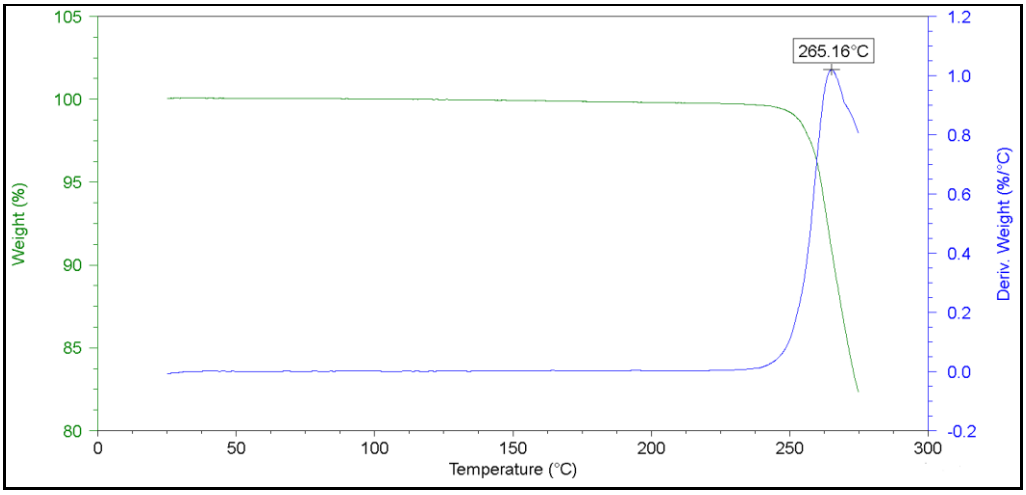

Figure 9a: TG and DTG curves of complex **1** showing the upper limit of stability.

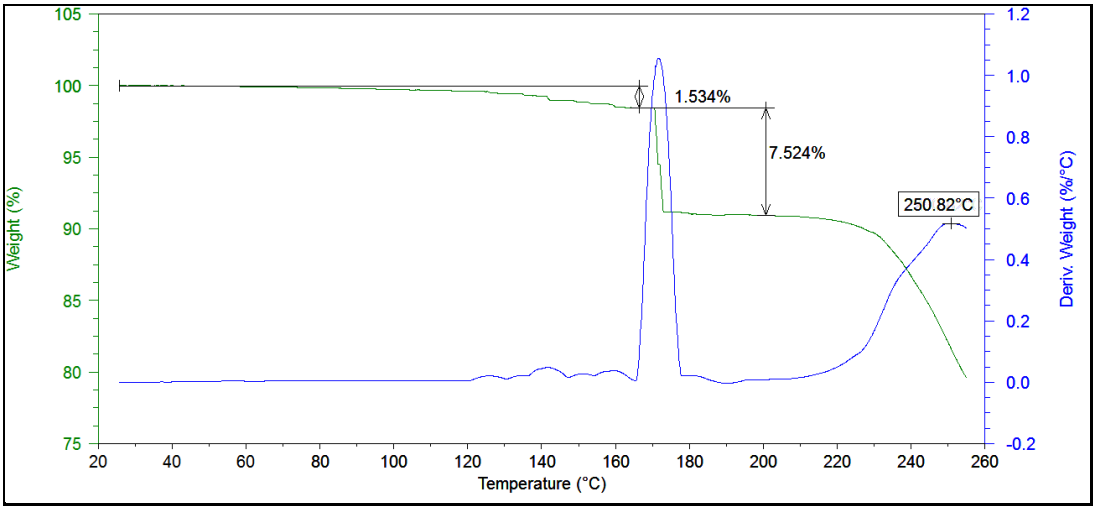

Figure 9b: TG-DTG curves of complex **2**.

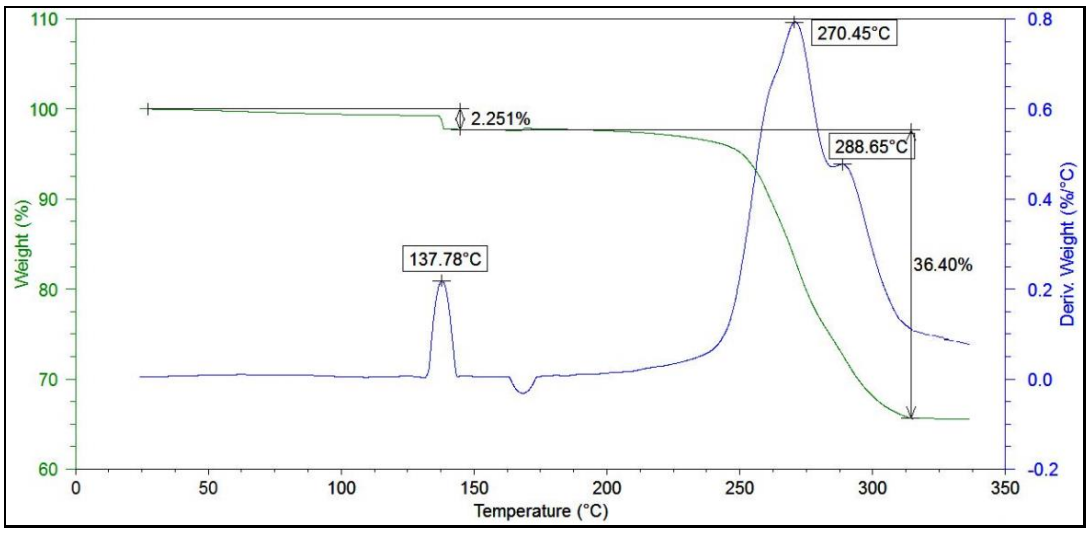

Figure 9c: TG-DTG curves of complex **3**.

4.3.7 Cyclic voltammetry

Figures 10a and 10b depicts the voltamograms of the Gd(III), Ho(III) and Nd(III) complexes. The cathodic peak potential (E_{pc}) values are observed at -1.83, -1.87 and -1.75 for complexes **1**, **2** and **3**, respectively. These peak potentials of the reduction current were taken at the scanning rate of 200 mVs^{-1} versus Ag/Ag^{+} and can be assigned to the reduction from Ln(III) to Ln(II) [16]. Ho(III) is the hardest to reduce. Anodic peak potentials are also observed for Gd(III) and Ho(III) at 0.963 and 1.046 V and these can be assigned to the oxidation of Ln(II) formed during the preceding cathodic scan to Ln(III).

Some 4*f* elements such as gadolinium require a much larger potential to accept electrons as evidenced by a very negative theoretical standard reduction potential of -2.28 V *versus* the Normal Hydrogen Electrode. However, the presence of the aromatic π-system may ensure easy reduction of the complex. This is made possible by the withdrawal of the electron density from the metal, thus stabilising the lower oxidation state [17].

In contrast, it is more difficult to reduce Nd(III) in $Nd(H_2L_1)_2(NO_3)_3$ than in the H_2pydm complex discussed in Chapter 3, as demonstrated by the lower reduction potential given by complex **3**. This could be attributed to differences in electron withdrawing abilities of the ligands [17].

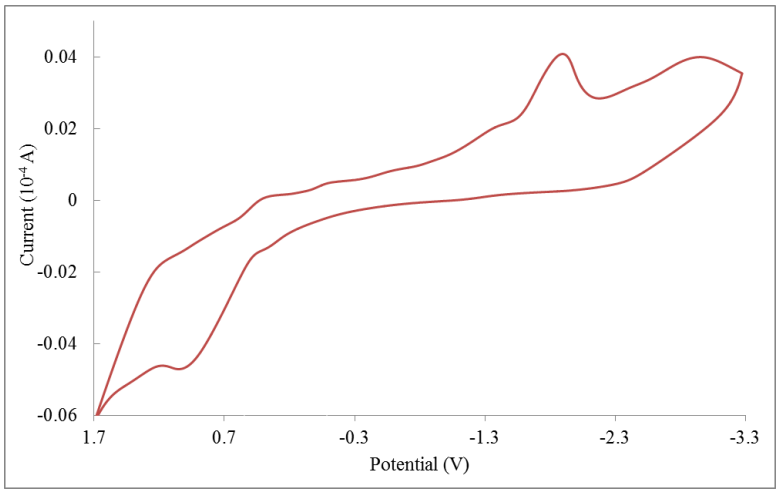

Figure 10a: Cyclic voltammogram of a 1.90 mM DMF solution of complex **1**.

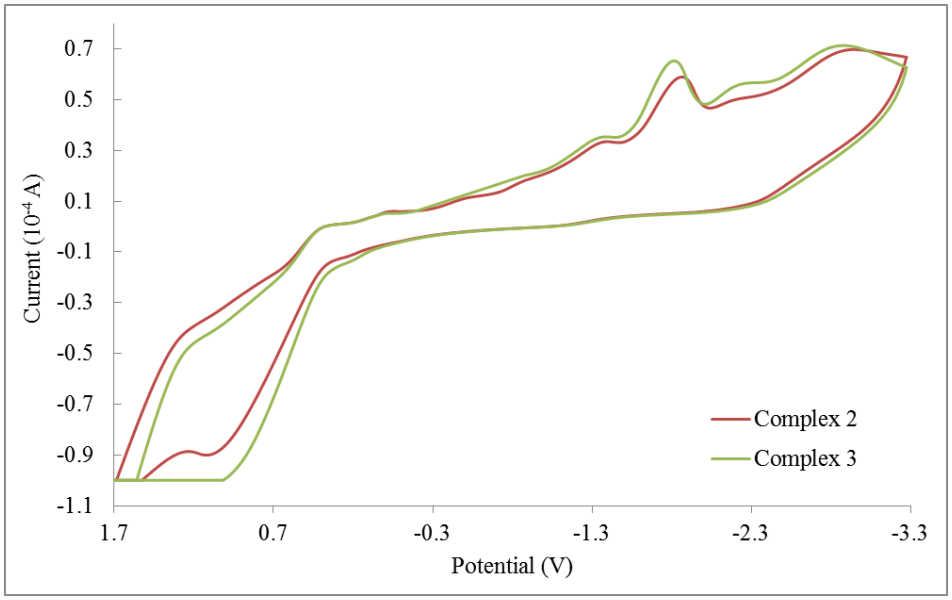

Figure 10b: Cyclic voltammograms of 3.21 mM DMF solutions of **2** and **3**.

Based on the above studies, it can be concluded that Nd(III) coordinates to H_2L_1 in the same manner as Gd(III) and Ho(III). The proposed coordination structure of the Nd(III) complex with the *o*-vanillin derived Schiff base is presented in Figure 11.

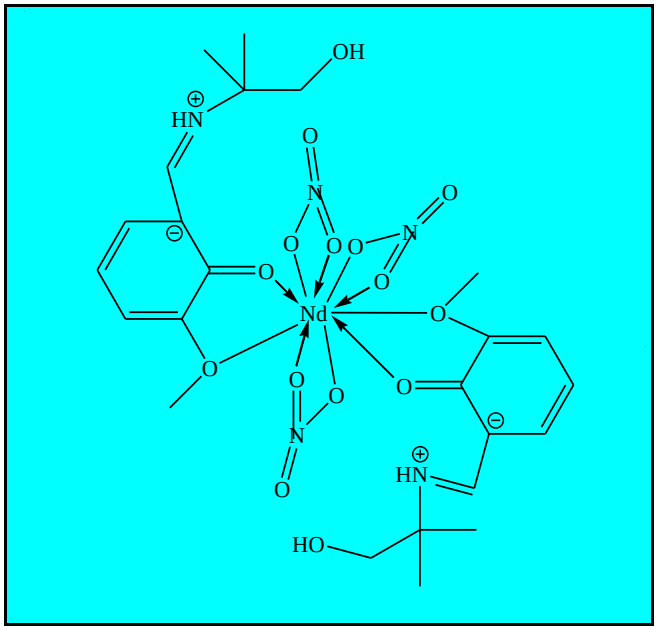

Figure 11: Proposed structure of the Nd(III)-H_2L_1 complex.

4.4 Conclusion

Coordination of the lanthanides Gd(III), Ho(III) and Nd(III) to the Schiff base ligand H_2L_1 converted the ligand to its zwitterionic phenoxo-iminium form as a result of proton migration from the phenol function to the imine function. The *o*-vanillin derivative coordinated bidentately *via* the phenolate oxygen and the methoxy oxygen atoms. SHAPE analyses of the ten-coordinate Gd(III) and Ho(III) complexes indicated distorted tetradecahedron geometries.

The crystal structure of the Nd(III) complex could not be obtained due to badly intertwined crystals. However, the use of other analytical techniques, such as microanalysis and IR, enabled the prediction of the structure of the complex. It was concluded that the Nd(III) complex was isostructural to the Gd(III) and Ho(III) compounds.

Thermal stability studies and thermal degradation behaviours of the complexes were studied. These studies (TG-DTG) played an important role in showing the upper limit of stabilities of complexes as well as early stages of degradation. Furthermore, it was noted that the complexes decompose *via* different pathways.

4.5 Crystallographic data

Table 3a: Crystal and structure refinement data for **1**.

Formula	$C_{24}H_{34}GdN_5O_{15}$
M_r (g.mol^{-1})	789.81
Crystal system	Monoclinic
Space group	$P2_1/c$
a, *b*, *c* [Å]	11.9775(4), 12.6167(3), 20.5691(5)
α, β, γ (°)	90, 90.271(1), 90
V (Å^3)	3108.30(15)
Z	4
ρ (mg.m^{-3})	1.688
μ (mm^{-1})	2.211
F(000)	1588
Crystal size (mm)	0.24×0.29×0.34
Temperature (K)	200
Mo *Kα* radiation, λ (Å)	0.71073
θ (min-max) (°)	1.7, 28.3
Data set	$-15\leq h\leq 13$; $-16\leq k\leq 14$; $-22\leq l\leq 27$
Tot., Unique data, R_{int}	28708, 7493, 0.016
Observed [I>2σ(I)] reflections	6385
$N_{reflections}$, $N_{parameters}$	7493, 433
$R[F^2>2\sigma(F^2)]$, $wR(F^2)$, *S*	0.0258, 0.0563, 1.17
$\Delta\rho_{min}$, $\Delta\rho_{max}$ (e. Å^{-3})	-0.90, 1.77

Table 3b: Crystal and structure refinement data for **2**.

Formula	$C_{24}H_{34}HoN_5O_{15}$
M_r (g.mol^{-1})	797.49
Crystal system	Monoclinic
Space group	$P2_1/c$
a, *b*, *c* [Å]	11.9411(5), 12.5894(5), 20.4572(9)
α, β, γ (°)	90, 90.335(2), 90
V (Å^3)	3075.3(2)
Z	4
ρ (mg.m^{-3})	1.722
μ (mm^{-1})	2.651
F(000)	1600
Crystal size (mm)	0.25×0.28×0.29
Temperature (K)	200
Mo *Kα* radiation, λ (Å)	0.71073
θ (min-max) (°)	1.7, 28.4
Data set	$-15\leq h\leq 15$; $-16\leq k\leq 16$; $-27\leq l\leq 27$
Tot., Unique data, R_{int}	28175, 7617, 0.019
Observed [I>2σ(I)] reflections	6534
$N_{reflections}$, $N_{parameters}$	7614, 436
$R[F^2>2\sigma(F^2)]$, $wR(F^2)$, *S*	0.0203, 0.0505, 1.03
$\Delta\rho_{min}$, $\Delta\rho_{max}$ (e.Å^{-3})	-0.76, 1.03

4.6 References

[1] A.O. Sobola, G.M. Watkins and B. Van Brecht, *S. Afr. J. Chem.*, **67** (2014) 45-46.

[2] X. Qin, Y. Ji, Y. Gao, L. Yan, S. Ding, Y. Wang and Z. Liu, *Z. Anorg. Allg. Chem.*, **640** (2014) 462-463.

[3] Y. Su, L. Yang, X. Jin, S. Weng and J. Wu, *J. Mol. Struct.*, **616** (2002) 221-230.

[4] T. Gao, P.-F. Yan, G.-M. Li, G.-F. Hou and J.-S. Gao, *Polyhedron*, **26** (2007) 5382–5383.

[5] W.-B. Sun, P.-F. Yan, G.-M. Li , H. Xu and J.-W. Zhang, *Journal of Solid State Chemistry*, **182** (2009) 382.

[6] M. Xu, Y.-C. Zhang, Z.-H. Xu and Z.-Z. Zeng, *Inorg. Chim. Acta*, **384** (2012) 327.

[7] G. Rajendran and V. Amitha, *Asian J. Chem.*, **19** (2007) 2538.

[8] C.C. Hinckley, *J .Amer. Chem. Soc.*, **91** (1969) 5160.

[9] J. Lisowski, J.L. Sessler, V. Lynch and T.D. Modyi, *J. Am. Chem. Soc.*, **117** (1995) 2273.

[10] A.F. Cockerill, G.L.O. Davies, R.C. Harden and D.M. Rackham, *Chem. Rev.*, **73** (1973).

[11] W.D. Horrocks and J.P. Sipe, *J. Am. Chem. Soc.*, **93** (1971).

[12] K. Raja, A. Suseelamma and K.H. Reddy, *J. Iran. Chem. Soc.*, **12** (2015) 1476.

[13] Q. Li, P. Yan, P. Chen, G. Hou and G. Li, *Inorg. Organomet. Polym.*, **22** (2012) 1175.

[14] S.A. Cotton, O.E. Noy, F. Liesener and P.R. Raithby, *Inorg. Chim. Acta*, **344** (2003) 39-40.

[15] B. Cristovao and Z. Hnatejko, *J. Mol. Struct.*, **1088** (2015) 52.

[16] H. Yamana, B.G. Park, O. Shirai, T. Fujii, A. Uehara and H. Moriyama, *Journal of Alloys and Compounds*, **408–412** (2006) 67.

[17] L.M.A. Monzon, *J. Electroanalyt. Chem.*, (2010) 1-6.

CHAPTER 5

Decomposition of an *o*-vanillin derived Schiff base ligand and its dinuclear Ce(III) complex

5.1 Introduction

In this chapter, the coordination properties of the potentially multidentate Schiff base ligand, 2-((*E*)-(1-hydroxy-2-methylpropan-2-ylimino)methyl)-6-methoxyphenol (H_2L_1, Figure 1) with Ce(III) are reported.

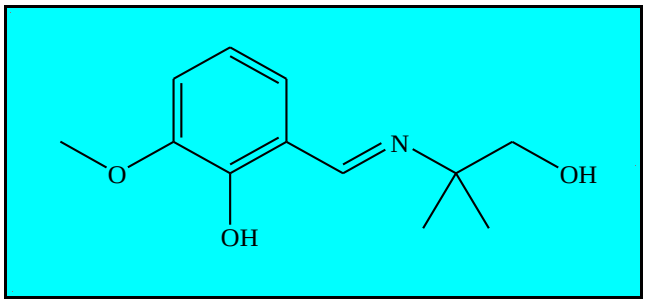

Figure 1: The structure of H_2L_1.

Recent studies have shown that a nickel complex of H_2L_1 has been synthesised and characterised for its luminescent and magnetic behaviour [1]. In the dinuclear Ni(II) complex, the monodeprotonated H_2L_1 acts as a tridentate chelate with coordination occurring through the imino nitrogen atom, the hydroxyl oxygen atom and one deprotonated phenolate oxygen atom. Completing the coordination environment around the metal centre is a monodeprotonated *o*-vanillin ($ovan^-$) molecule acting as a tridentate chelate utilising all three oxygen atoms. The Ni(II) ions are six-coordinate and display slightly distorted octahedral coordination [1]. The structure of this Ni(II) complex is shown in Figure 2.

Sobola *"et al"* also reported the hydrolysis of the methyl and methoxyl derivatives of *o*-vanillin Schiff bases in the presence of aqueous ammonia to yield *o*-vanillin (ovanH) [2]. The *o*-vanillin was then converted to (2-methoxy-6-imino)methylphenol and coordinated to Cu(II) leading to the formation of bis-(2-methoxy-6-imino)methylphenol copper(II) (Figure 3).

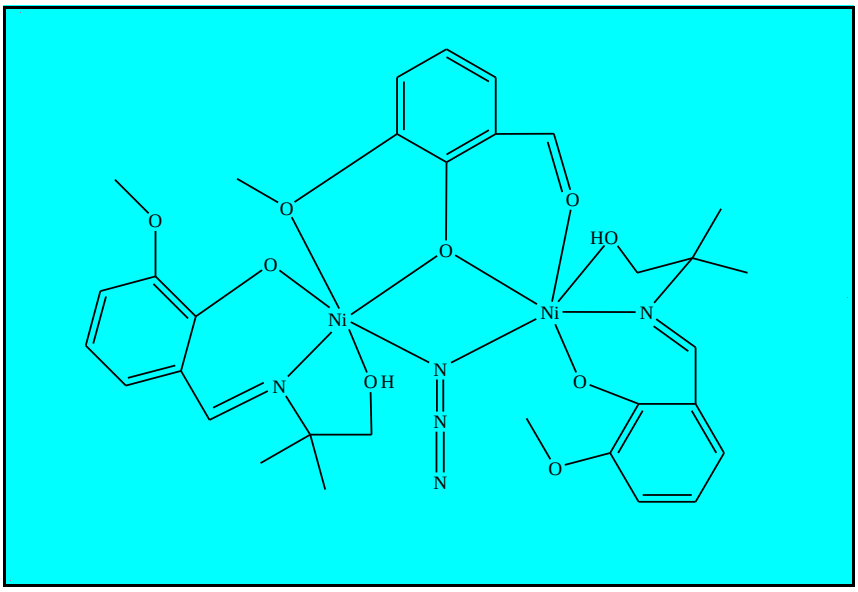

Figure 2: Coordination of H_2L_1 in the dinuclear Ni(II) complex.

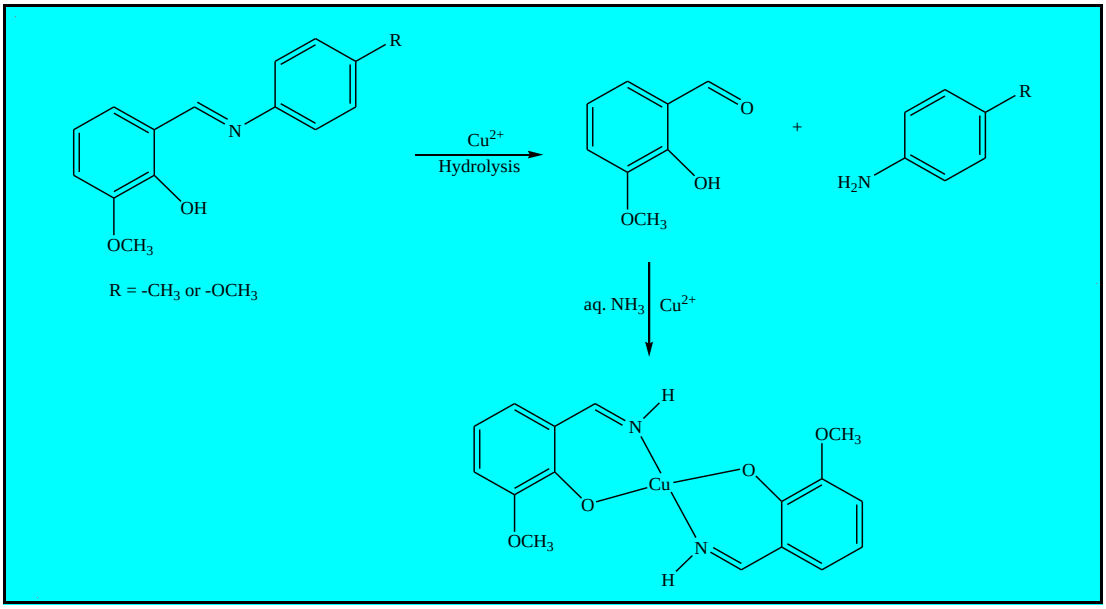

Figure 3: Synthetic route of Cu(ovan-NH)$_2$ from the hydrolysed Schiff base ligands.

A literature review revealed that no synthetic or structural characterisation of any 4*f* element with H_2L_1 has been done. This prompted an investigation into the coordination behaviour of these compounds to gain an understanding on configurations and spectral properties.

5.2 Synthesis of $[Ce_2(H_2L_1)(ovan)_3(NO_3)_3]$

To a 10 mL methanolic solution of H_2L_1 (0.345g, 1.55 mmol) was added a 5 mL methanolic solution of $Ce(NO_3)_3{\cdot}6H_2O$ (0.246g, 0.567 mmol). The resulting mixture was stirred continuously for 30 minutes at room temperature, followed by filtration of the yellow solution to get rid of undissolved material. Brown single crystals suitable for X-ray crystallography were grown within 3 days under vapour diffusion using diethyl ether. Yield: 65.7%, m.p. = 212.3-214.5 ^{o}C. Anal. Calcd. for $C_{36}H_{37}Ce_2N_4O_{21}$,2($CH_4O$) (%): C, 37.84; H, 3.76; N, 4.64. Found: C, 37.82; H, 3.71; N, 4.68. Conductivity (10^{-3} M, DMF): 184.0 $ohm^{-1}cm^2mol^{-1}$. UV-Vis (DMF, λ_{max} nm (ε, $M^{-1}cm^{-1}$)): 340 (1030). IR (cm^{-1}): ν_{as}(N-O) 1549 (s), ν(C-H) 1435(s), ν_s(N-O) 1297(s), ν(C-N) 1248(s), ν(Ce-O) 420(m).

5.3 Results and discussion

The compound $[Ce_2(H_2L_1)(ovan)_3(NO_3)_3]$ was synthesised by the reaction of $Ce(NO_3)_3{\cdot}6H_2O$ with a three-fold molar excess of H_2L_1 in methanol, with stirring at room temperature under nitrogen. Brown crystals were formed upon vapour diffusion using diethyl ether.

$$Ce(NO_3)_3{\cdot}6H_2O + 3H_2L_1 \xrightarrow[\text{Diethyl ether}]{\text{Methanol}} Ce_2(H_2L_1)(ovan)_3(NO_3)_3$$

The dinuclear complex is stable in air and is an electrolyte in DMF. It is soluble in a variety of solvents, such as methanol, ethanol, DMF and DMSO.

The introduction of a methanolic solution of $Ce(NO_3)_3 \cdot 6H_2O$ to H_2L_1 yielded *o*-vanillin due to hydrolysis of the imine bond, which then coordinated in its monodeprotonated form $ovan^-$ together with H_2L_1 (see Figure 4).

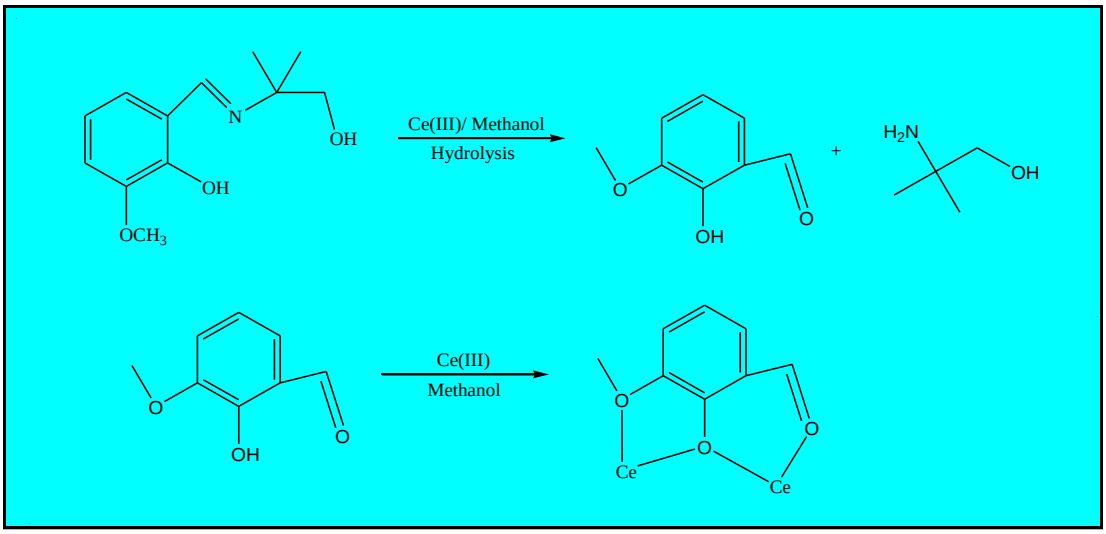

Figure 4: Formation of *o*-vanillin from the hydrolysis of the Schiff base and its bridging mode to the metal.

5.3.1 Infrared spectroscopy

The IR spectrum of the free H_2L_1 has been discussed in Chapter 4 [3]. Upon coordination, the O-H and C-H vibrational bands become less intense (see Figure 5). The C-H bending band is shifted to 1435 cm^{-1} and the ν(C-N) is shifted to lower energy by about 19 cm^{-1}. The appearance of the band at 420 cm^{-1} has been assigned to the ν(Ce-O), supporting the formation of Ce-O bonds [4]. The absorption bands at 1549 and 1297 cm^{-1} may be attributed to the N-O asymmetric (ν_{as}) and N-O symmetric (ν_s) stretches, respectively. The separation of the two frequency bands (ν_{as}-ν_s) is 252 cm^{-1}, which is in accordance with the bidentate character of the nitrate groups [4,5].

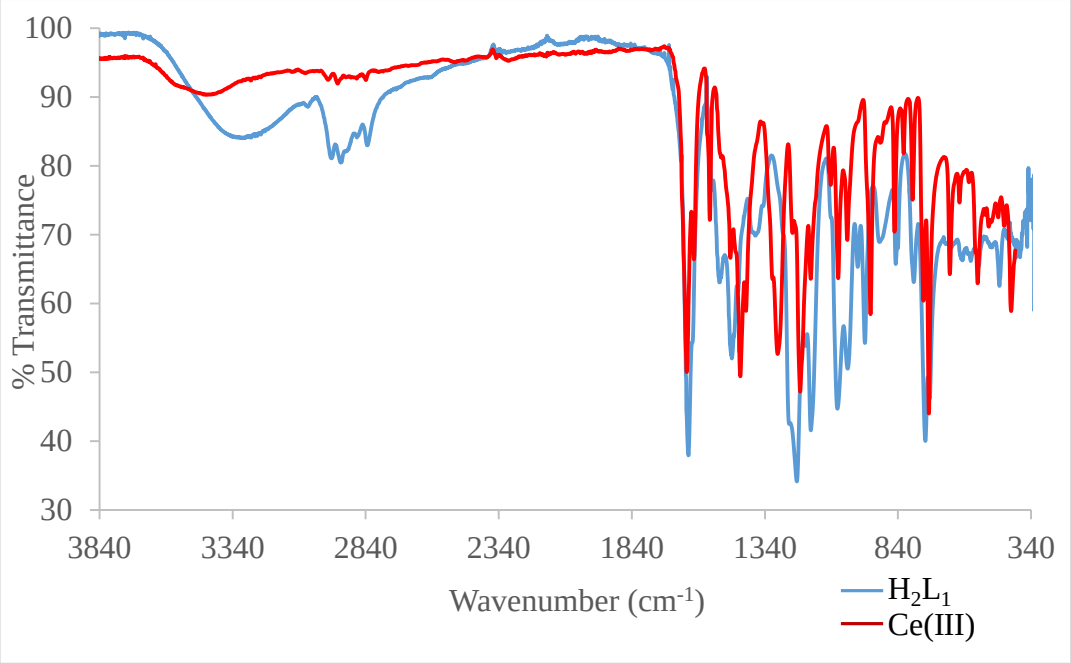

Figure 5: The IR spectra of uncoordinated H_2L_1 and the dinuclear Ce(III) complex.

5.3.2 NMR analysis

The proton NMR spectrum of H_2L_1 is given and discussed in Chapter 4 (Figure 4a). The difficulty in interpreting the ^{1}H NMR spectrum of the complex arises from the peak broadening as can be expected from the paramagnetic Ce(III) ion (Figure 6). The spectrum exhibits more peaks than expected for the Schiff base ligand. The additional signals can be attributed to the monoanionic *o*-vanillin protons.

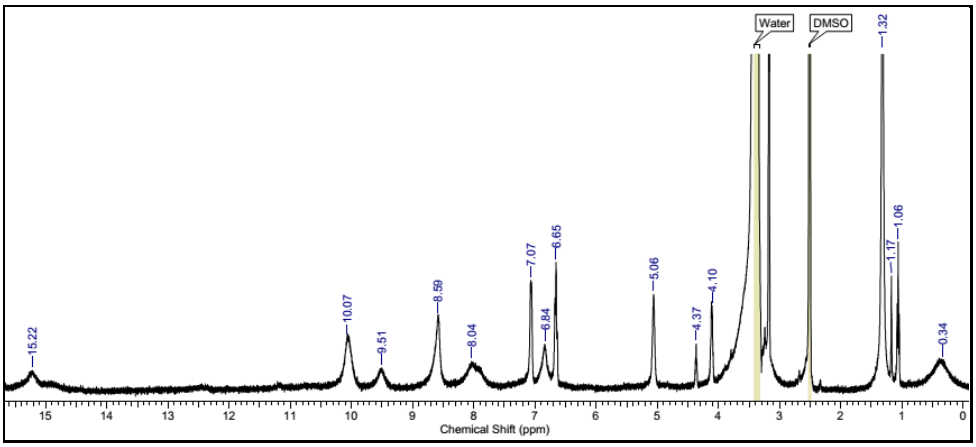

Figure 6: ^{1}H NMR of the metal complex in DMSO-d_6.

5.3.3 UV-Vis spectroscopy

The UV-Vis absorption spectrum of H_2L_1 shows strong π-π* and n-π* transition peaks at 329 and 420 nm, respectively. The absorption spectra of the free ligand and the dimeric complex are superimposed in Figure 7. It is noted that the lower wavelength absorption band in H_2L_1 is red-shifted by about 11 nm upon complexation with Ce(III) and the n-π* transition band flattens out. The shift is due to the effective crystal-field as a result of interelectronic repulsion between the 4*f* electrons and is related to covalence in the Ln-ligand bond [4].

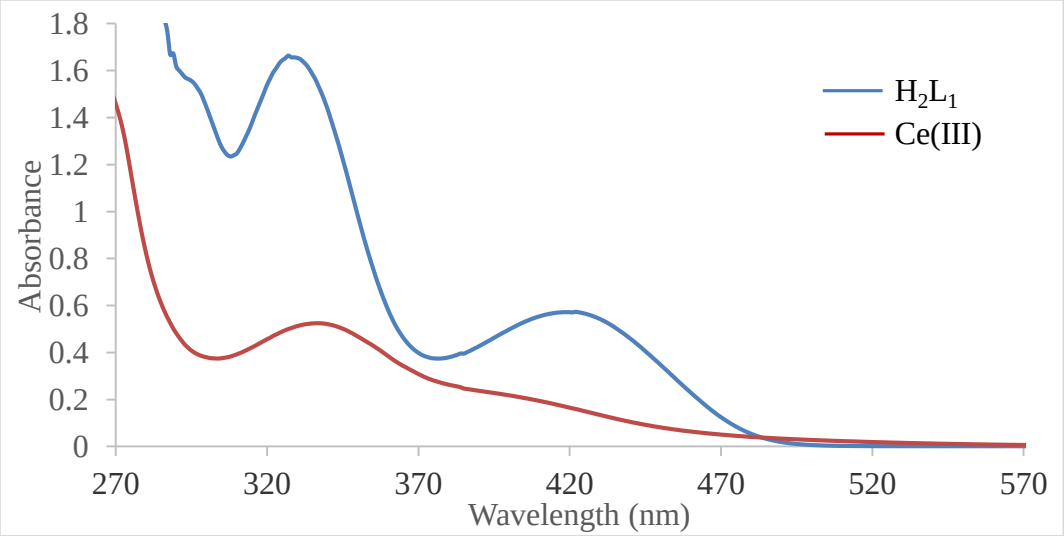

Figure 7: UV-Vis spectra of H_2L_1 (6.25×10^{-5} M) and the Ce(III) complex (5.10×10^{-4} M) in DMF solutions at room temperature.

5.3.4 Shape analysis

Polyhedral views of the two cerium atoms and ideal shapes are given in Figure 8, and deviation parameters (continuous shape measure values) are listed in Table 1. The geometries for the two Ce(III) ions in the dinuclear complex were found to be different. The shapes around the Ce1 and Ce2 atoms are tetradecahedron (TD-10) and staggered dodecahedron (SDD-10), respectively. The SDD-10 shape has 8_3+4_4 faces (8 triangles and 4 squares), 20 edges and exhibit D_2 symmetry. A less distorted coordination sphere is observed for the Ce2 atom compared to the Ce1 atom. When

taking into account steric effects; ligand type, size and shape are an important consideration in geometry [6]. The Ce2 ion has a lower deviation from the ideal shape due to the fairly rigid chelate rings resulting from small nitrate bite angles as well as shorter Ce(2)-O bond lengths afforded by the carbonyl groups of the deprotonated *o*-vanillin. In contrast, the Ce1 atom is connected to the huge H_2L_1 ligand with a larger bite angle and has only one nitrate group attached. In addition, it possesses longer Ce-$O_{methoxy}$ bonds than Ce2.

It is also noted that there is a very small difference between the CShM values of TD-10 and SDD-10 shapes for the Ce2 atom. Thus, an interconversion between the two polyhedral structures may occur in solution or solid state [7]. Rare-earth complexes show flexibility and are in dynamic behaviour especially in solution due to lack of strong, directional bonding as well as large ionic radii of the rare-earth ions and high coordination numbers. Therefore, interconversion is brought about by rearrangements of ligands influenced by steric factors. It is therefore necessary to describe the interconversion path between two ideal polyhedra by taking into account the minimum distortion angle, θ_{PT}, or the related minimum distortion constant, k_{PT}, which is obtained by calculation of the CShM of one shape (P) relative to the other (T) [7].

Table 1: SHAPE analysis of the dinuclear complex.

	DP-10	EPY-10	OBPY-10	PPR-10	PAPR-10	SDD-10	TD-10	HD-10
Ce1	36.3037	23.6085	16.4401	10.4555	14.2250	5.3426	**4.9327**	9.6425
Ce2	33.2272	22.1996	16.1922	9.6558	12.2478	**4.2017**	4.2705	10.4270

It is observed that there is a decrease in CShM values from Ce to Ho (Chapter 4) as the ionic radii decreases, except for the Ce2 atom coordination sphere that deviates from the trend. The reason could be that the Ce2 ion is not directly connected to the Schiff base ligand, but is only bonded to small nitrate groups and ovan$^-$.

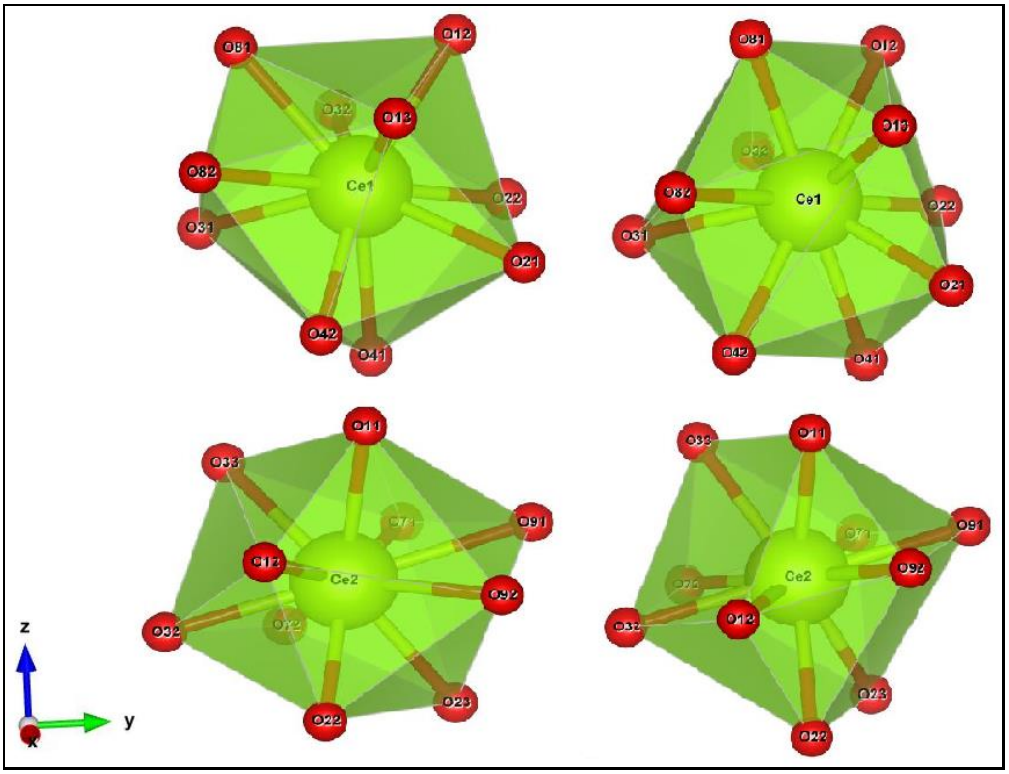

Figure 8: Polyhedral view of the ten-coordinate Ce1 atom (top left), ideal TD-10 (top right), ten-coordinate Ce2 atom (bottom left) and ideal SSD-10 (bottom right).

5.3.5 Crystal data

The complex crystallises in the monoclinic system with space group of $P2_1/c$. The structure consists of a neutral, well-separated dinuclear unit $[Ce_2(H_2L_1)(ovan)_3(NO_3)_3]$ and two crystallographic methanol molecules. As shown in Figure 9a, the dinuclear Ce(III) complex consists of two lanthanide ions, three bridging monodeprotonated *o*-vanillin molecules, three bidentate nitrate groups and one Schiff base ligand (H_2L_1), which acts in its bidentate *O,O*-donor mode. Both metal ions exist in the +3 oxidation state and a total of 6+ cationic charges is neutralised by three nitrate groups and three bridging phenolate oxygens. This scenario shows that the Schiff base ligand remains protonated. However, the phenolic hydrogen atom could not be located. This atom is expected either to be part of the phenolic group or bonded to the imino nitrogen atom in case of a proton transfer [8,9]. Inspection of the Ce-O bond distances revealed that one of the cerium ions cannot be in the +4 oxidation state since the bond lengths are

longer than expected for Ce(IV) [10]. Ce(IV) complexes give relatively lower Ce-O bond distances, such as in $[Ce(IV)(L_2)]\cdot 2CH_2Cl_2$ (H_2L = *N,N′*-bis(2-oxy-3-methoxybenzylidene) and the Ce(IV) complex with amine bis(phenolate) ligands in which the Ce-O bond lengths were found to be in the ranges 2.212(15)-2.226(16) and 2.139(3)-2.160(3) Å, respectively [10,11]. It is interesting to note that each of the rare-earth ions is decacoordinated but they have different coordination environments. The ten-coordinate centres, Ce1 and Ce2, adopt distorted tetradecahedron and staggered dodecahedron geometries, respectively.

The ten coordination sites of Ce1 are occupied by two oxygen atoms from the bidentate nitrate molecule, two oxygen atoms (from the alkoxyl and phenolic groups) from H_2L_1 and six oxygen atoms (two methoxyl, three deprotonated phenolate and one carbonyl oxygen) from *o*-vanillin. The Ce2 centre is coordinated to two bidentate nitrates and six oxygen atoms (three phenolate, two carbonyl and one methoxyl oxygen) from three monodeprotonated tridentate *o*-vanillin molecules. The two central Ce(III) ions are interconnected through oxygen bridges afforded by three deprotonated *o*-vanillin groups.

The bridging Ce(1)-O-Ce(2) angles [in the range 99.04(12)-102.76(12)^o] are normal and comparable to other Ln(III) centres bridged by the phenoxide groups. Examples of such complexes are the Dy(III) complex with the Schiff base *o*-vanillin oxime and the dinuclear Gd(III) complex with 2-[(2-hydroxypropylimino)methyl]phenol in which the Ln-O-Ln angles are in the ranges 103.89(10)–105.27(10)^o and 95.76(12)-96.26(12)^o, respectively [12,13]. The Ce-O-Ce bond angles are also in accordance with those in previously reported phenolate oxygen-bridged transition metal complexes, such as those in which the Zn-O-Zn angles were found to lie in the range of 94.962(2)-103.665(3)^o [1]. The H_2L_1 O-Ce-O bite angle is found to be 59.70(12)^o and the nitrate O-Ce-O bite angles range from 48.34(12)-49.19(13)^o. For ovan$^-$ coordination, it is observed that $O_{bridging}$-Ce-$O_{(C=O)}$ angles [average = 69.03^o] are significantly greater than $O_{bridging}$-Ce-$O_{methoxy}$ [average = 60.80^o], with the former giving six-membered chelate rings and the latter forming five-membered rings. Thus, there is a good correlation between bite angle and size of the chelate ring. The bigger

the ring, the wider the angle. A small difference in bite angles is seen between the five-membered chelate rings formed by H_2L_1 and $O_{bridging}$-Ce-$O_{methoxy}$.

An inspection of metric parameters shows that the average bond distances Ce-$O_{ovan\ methoxy}$ = 2.651 Å, Ce-$O_{nitrate}$ = 2.619 Å, Ce-$O_{H_2L_1}$ = 2.579 Å, Ce-$O_{ovan\ C=O}$ = 2.513 Å and Ce-$O_{bridging}$ = 2.460 Å are similar to those found in the literature [4]. Selected bond lengths and angles for the complex are presented in Table 2a. The Ce···Ce distance is equal to 3.823 Å. This distance is longer than those found in other similar dinuclear rare-earth complexes [5,13]. A photo of the crystals used for X-ray analysis is given in Figure 9b.

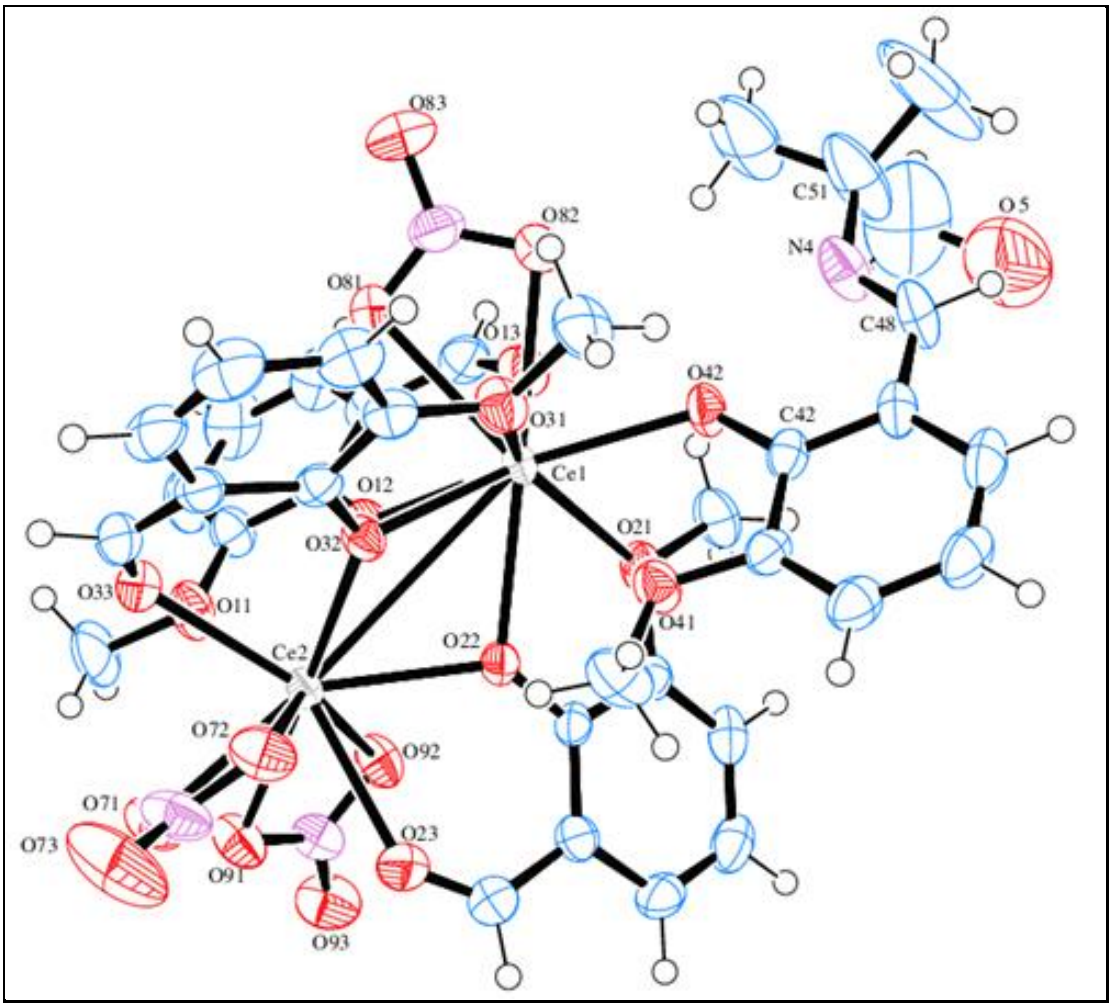

Figure 9a: The molecular structure of the Ce(III) complex showing 50% probability displacement ellipsoids and partial atom-labelling. The solvent of crystallisation (methanol) was omitted for clarity.

The plot of average Ln-O bond lengths against the number of 4*f* electrons in Figure 7f of Chapter 4 reveals that for the dinuclear cerium complex, the Ln−O_{all} lie below both Ln-$O_{nitrate}$ and Ln-$O_{H_2L_1}$. This is due to shorter Ce-O bond distances generated by the bridging and carbonyl oxygens of $ovan^-$.

Table 2a: Selected bond lengths and angles in $Ce_2(H_2L_1)(ovan)_3(NO_3)_3$.

Bond distances (Å)		**Bond angles (°)**	
Ce1-O13	2.465(4)	O41-Ce1-O42	59.70(12)
Ce2-O11	2.624(3)	O71-Ce2-O72	49.19(13)
Ce1-O12	2.508(3)	O91-Ce2-O92	48.34(12)
Ce2-O22	2.418(3)	Ce1-O12-Ce2	99.04(12)
Ce1-O41	2.770(3)	Ce1-O22-Ce2	102.76(12)
Ce1-O42	2.389(3)	Ce1-O32-Ce2	101.51(13)
Ce2-O71	2.610(4)	O12-Ce1-O13	69.76(13)
Ce2-O72	2.587(4)	O11-Ce2-O12	60.77(11)
O42-C42	1.309(6)	C48-N4-C51	128.3(6)

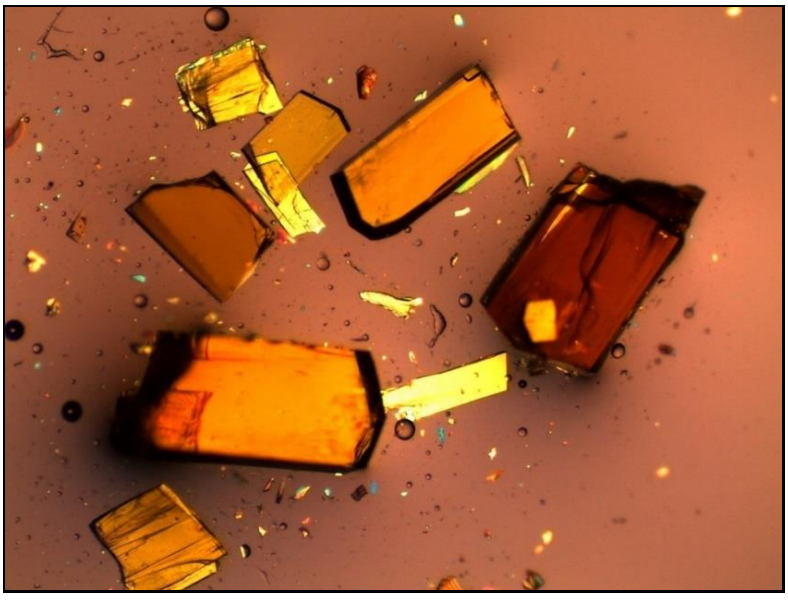

Figure 9b: A photo of the crystals of the Ce(III) complex used for X-ray analysis.

A detailed investigation of the packing diagram of the dimeric complex shows the existence of intra- and intermolecular hydrogen bonding interactions (Figure 9c and Table 2b). The O-H group of H_2L_1 is hydrogen bonded to the coordinated oxygen atom of the nitrate with an H···O bond distance of 2.3300 Å. An intramolecular hydrogen bond is seen in the ligand H_2L_1, with the hydroxyl group interacting with the imino nitrogen atom [O···N; 2.830(14) Å]. Additionally, intermolecular hydrogen bonds exist between the oxygen atoms of the lattice methanol molecules and the hydroxyl groups of the crystallographic solvent.

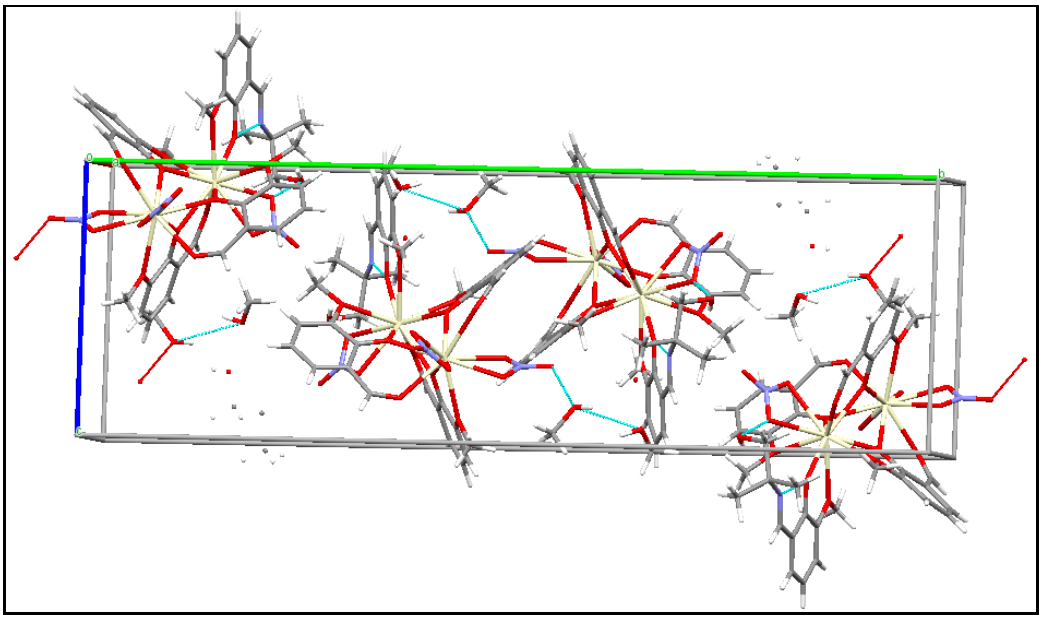

Figure 9c: Unit cell structure of $Ce_2(H_2L_1)(ovan)_3(NO_3)_3$.

Table 2b: Hydrogen bond parameters (Å, °) in the Ce(III) complex.

D*-H···*A	***D*-H**	**H···*A***	***D*···*A***	***D*-H···*A***
O(5)-H(5)···O(82)	0.8400	2.3300	2.865(14)	122.00
O(5)-H(5)···N(4)	0.8400	2.4800	2.830(14)	106.00
O(7)-H(7)···O(8)	0.8400	2.1900	2.850(15)	135.00
O(8)-H(8)···O(7)	0.8400	2.3200	2.850(15)	121.00

D = donor, *A* = acceptor.

5.3.6 Thermal analysis

The TG, DTG and DTA curves of the dinuclear complex are shown in Figure 10. The thermal analysis was carried out from room temperature to 260 ^{o}C under a N_2 atmosphere at a heating rate of 10 ^{o}C/min. At the first step (22-106 ^{o}C) there is a total mass loss of 5.49% and this corresponds to the loss of two methanol molecules (calculated = 5.31%). This mass loss has maximum rates, T_{DTG} and T_{DTA} at 44.36 and 47.77 ^{o}C, respectively [14]. The complex is then thermally stable up to 215 ^{o}C after which thermal degradation continued.

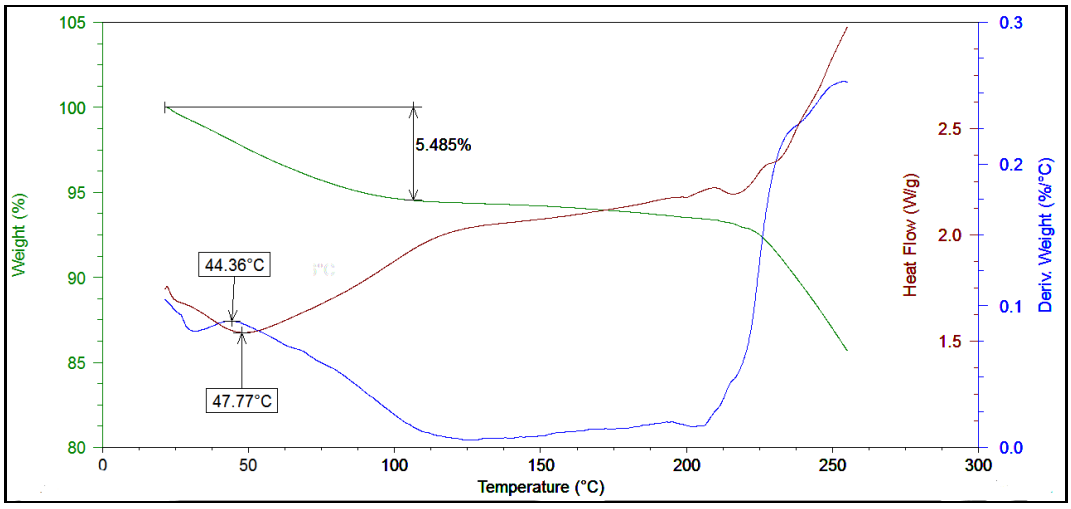

Figure 10: The TG, DTG and DTA curves of the Ce(III) complex.

5.3.7 Cyclic voltammetry

The cyclic voltammetric behaviour of the complex is shown in Figure 11. It can be seen that the complex has a cathodic peak at -1.66 V. The electrochemically active cerium centre is reduced from +3 to +2 [15].

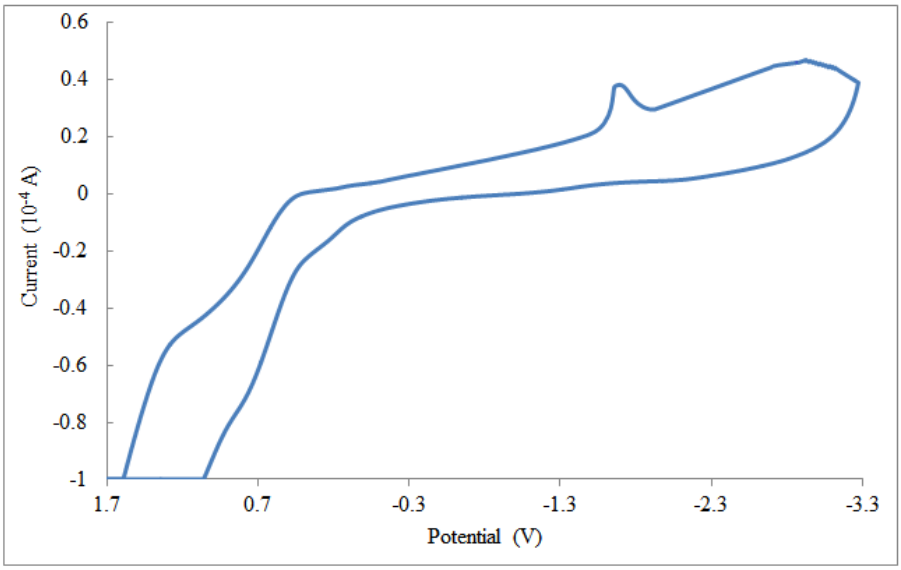

Figure 11: The cyclic voltammetry curve of the 2.07 mM DMF solution of the Ce(III) complex.

5.4 Conclusion

A novel dimeric cerium(III) complex, with the formula $[Ce_2(H_2L_1)(ovan)_3(NO_3)_3]$, has been successfully synthesised using the Schiff base ligand, 2-((*E*)-(1-hydroxy-2-methylpropan-2-ylimino)methyl)-6-methoxyphenol. The complex has been fully characterised using various physico-chemical techniques. The ligand coordinated bidentately *via* the phenolic and the methoxy oxygen atoms. Hydrolysis of the ligand occurred to yield *o*-vanillin, which connected the two Ce(III) centres through bridging phenolate oxygens. The shape studies of the coordination compound revealed different geometries adopted by the two metal centres.

5.5 Crystallographic data

Table 3: Crystal and structure refinement data for $Ce_2(H_2L_1)(ovan)_3(NO_3)_3$

Formula	$C_{36}H_{37}Ce_2N_4O_{21}$, $2(CH_4O)$
M_r (g.mol^{-1})	1206.02
Crystal system	Monoclinic
Space group	$P2_1/c$
a, b, c [Å]	12.3609(6), 33.9840(15), 11.8075(5)
α, β, γ (°)	90, 90.052(2), 90
V (Å^3)	4599.6(4)
Z	4
ρ (mg.m^{-3})	1.742
μ (mm^{-1})	2.043
F(000)	2404
Crystal size (mm)	0.32×0.34×0.44
Temperature (K)	200
Mo *Kα* radiation, λ (Å)	0.71073
θ (min-max) (°)	1.8, 28.4
Data set	$-16\leq h\leq 16$; $-41\leq k\leq 45$; $-14\leq l\leq 14$
Tot., Unique data, R_{int}	66489, 11484, 0.025
Observed [I>2σ(I)] reflections	10507
$N_{reflections}$, $N_{parameters}$	11484, 617
$R[F^2>2\sigma(F^2)]$, $wR(F^2)$, S	0.0490, 0.0991, 1.29
$\Delta\rho_{min}$, $\Delta\rho_{max}$ (e.Å^{-3})	-1.97, 1.84

5.6 References

[1] X. Qin, Y. Ji, Y. Gao, L. Yan, S. Ding, Y. Wang and Z. Liu, *Z. Anorg. Allg. Chem.*, **640** (2014) 462-463.

[2] A.O. Sobola, G.M. Watkins and B. van Brecht, *S. Afr. J. Chem.*, **67** (2014) 45-46.

[3] Y. Su, L. Yang, X. Jin, S. Weng and J. Wu, *J. Mol. Struct.*, **616** (2002) 221-230.

[4] K. Raja, A. Suseelamma and K.H. Reddy, *J. Iran. Chem. Soc.*, **12** (2015) 1476.

[5] M. Xu, Y.-C. Zhang, Z.-H. Xu and Z.-Z. Zeng, *Inorg. Chim. Acta*, **384** (2012) 327.

[6] G.A. Lawrance, *Introduction to Coordination Chemistry*, 1st edn, (2010) 20.

[7] D. Casanova, J. Cirera, M. Llunell, P. Alemany, D. Avnir and S. Alvarez, *J. Am. Chem. Soc.*, **126** (2004) 1755-1760.

[8] T. Gao, P.-F. Yan, G.-M. Li, G.-F. Hou and J.-S. Gao, *Polyhedron*, **26** (2007) 5382–5383.

[9] W.-B. Sun, P.-F. Yan, G.-M. Li , H. Xu and J.-W. Zhang, *Journal of Solid State Chemistry*, **182** (2009) 382.

[10] C. Chen, H. Chen, P. Yan, G. Hou and G. Li, *Inorg. Chim. Acta*, **405** (2013) 184.

[11] L. Li, F. Yuan, T. Li, Y. Zhou and M. Zhang, *Inorg. Chim. Acta*, **397** (2013) 72.

[12] I.J. Hewitt, Y. Lan, C.E. Anson, J. Luzon, R. Sessoli and A.K. Powell, *Chem. Commun.*, (2009) 6765.

[13] L. Zhang, Y. Ji, X. Xu, Z. Liu and J. Tang, *Journal of Luminescence*, **132** (2012) 1908.

[14] M.S. Refat, H.M.A. Al-Maydama, F.M. Al-Azab, R.R. Amin and Y.M.S. Jamil, *Spectrochim. Acta Part A: Molecular and Biomolecular Spectroscopy*, **128** (2014) 437.

[15] Y. Xuwu, S. Wujuan, K. Congyu, Z. Li, Z. Hangguo and G. Shengli, *Chem. Pap.*, **60** (2006) 134.

CHAPTER 6

Lanthanide-assisted conversion of thiosemicarbazones and thiosemicarbazides

6.1 Introduction

Previous studies on Cu(II) and Ni(II) with the ligand salicylaldehyde-*N*(4)-diethylthiosemicarbazone (H_2L_2) reported neutral and oxygen-bridged dinuclear species that crystallise in the monoclinic space group $P2_1/c$ (Figure 1). In both complexes the *O*,*N*,*S*-tridentate ligand is in the bideprotonated form (Figure 2) [1]. A π bond between the N-C bond is formed by conversion of the –C=S into –C-S^- to allow formation of a metal-sulfur sigma bond. This behaviour is very similar to that of the keto-enol tautomerism and is referred to as "thione-thiol tautomerism" [2]. The ligand is coordinated to the metals in the thiol form. These transition metal compounds were synthesised and characterised for their antimicrobial activities against pathogenic bacteria.

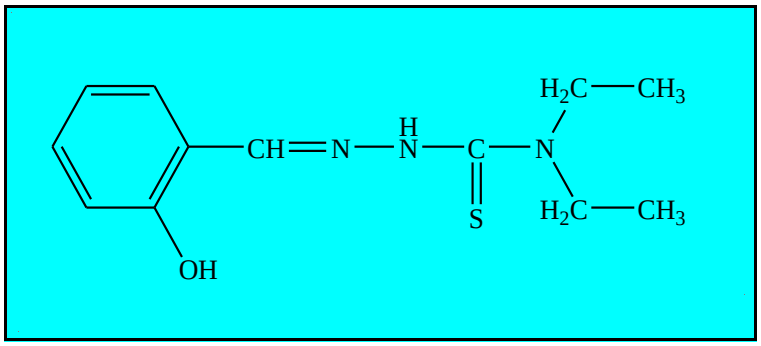

Figure 1: Structure of salicylaldehyde-*N*(4)-diethylthiosemicarbazone (H_2L_2).

No information has been found in the literature regarding the syntheses and characterisation of Ln(III) complexes with H_2L_2. This prompted an investigation into the coordination of the rare-earths with H_2L_2.

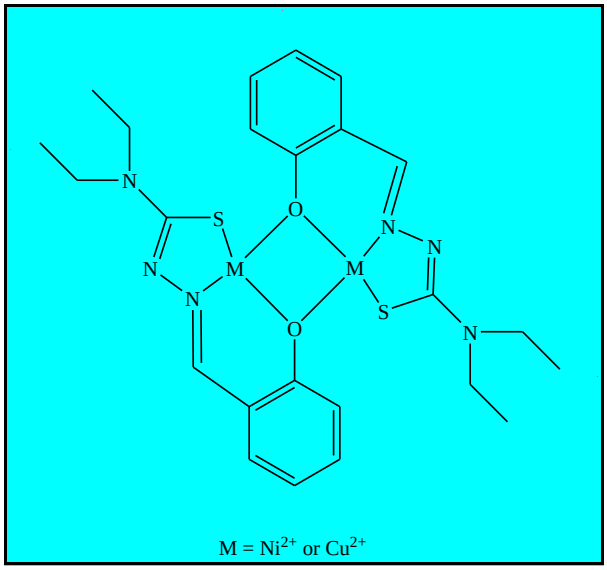

Figure 2: The structures of $[Ni(L_2)]_2$ and $[Cu(L_2)]_2$.

6.2 Synthesis of the thiosemicarbazone and thiosemicarbazide derivatives

6.2.1 Synthesis of (*E*)-2-[(*ortho*-hydroxy)benzylidene]-2-(thiomethyl)-thionohydrazide 1

A solution of salicylaldehyde-*N*(4)-diethylthiosemicarbazone (0.50 g, 2.0 mmol) in a 1:1 ethanol:methanol solution (10 mL) was added to a solution of $Tb(NO_3)_3 \cdot 5H_2O$ (0.44 g, 1.0 mmol) in 5mL ethanol:methanol (1:1, v/v). The reaction mixture was refluxed for 24 hours. Upon cooling to room temperature, cream X-ray quality crystals suitable for the diffraction study were obtained (Scheme 1). Yield: 63.6%, m.p. = 188.0-190.5 ^oC. Anal. Calcd. for $C_9H_{10}N_2OS_2$ (%): C, 47.76; H, 4.42; N, 12.38; S, 28.34. Found: C, 47.52; H, 4.11; N, 12.97; S, 28.38. IR (cm^{-1}): *v*(OH) 3620-3270(b), *v*(N-H) 3103(m), *v*(C-H) 2956(s), *v*(C=N) 1618(s), *v*(C-N) 1300(s), *v*(C=S) 750(s). ^1H NMR (DMSO-d_6, δ ppm): 13.33 (s, 1H, -OH), 10.23 (s, 1H, -CH=N-), 8.54 (s, 1H, -NH), 7.66-7.68 (d, 1H, Ar), 7.29-7.33 (t, 1H, Ar), 6.88-6.94 (m, 2H, Ar), 2.54 (s, 3H, $-CH_3$).

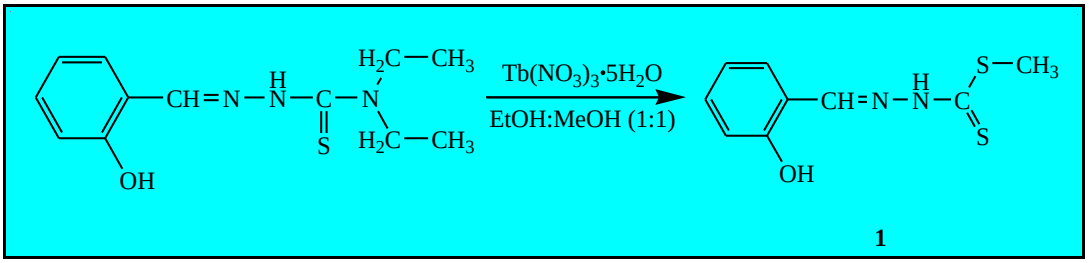

Scheme 1: Synthetic procedure of conversion product **1**.

6.2.2 Synthesis of bis[2,3-diaza-4-(2-hydroxyphenyl)-1-thiomethyl-buta-1,3-diene]disulfide 2

A 10 mL ethanolic solution of H_2L_2 (0.25 g, 1.0 mmol) was mixed with a 10 mL ethanolic solution of $SmCl_3 \cdot 6H_2O$ (0.36 g, 1.0 mmol), followed by stirring of the reaction mixture at room temperature for 4 hours. Single X-ray quality crystals were obtained upon slow solvent evaporation at room temperature (Scheme 2). Yield: 68.8%, m.p. = 172.5-174.8 ^oC. Anal. Calcd. for $C_{18}H_{18}N_4O_2S_4$ (%): C, 47.98; H, 4.03; N, 12.43; S, 28.41. Found: C, 47.93; H, 4.15; N, 12.35; S, 28.59. IR (cm^{-1}): *ν*(OH) 3620-3270(b), $\nu(C\text{-}H)_{aromatic}$ 3150(s), *ν*(C=N) 1616(s), *ν*(=C-H) 947(m). ^1H NMR (DMSO-d_6, δ ppm): 13.32 (s, 2H, -OH), 10.23 (s, 2H, -CH=N-), 7.66 (d, 2H, Ar), 7.31 (t, 2H, Ar), 6.91 (m, 4H, Ar), 2.54 (s, 6H, $-CH_3$).

Alternative method

A mixture of H_2L_2 (0.25 g, 1.0 mmol) and $La(NO_3)_3 \cdot 6H_2O$ (0.94 g, 1.0 mmol) in 15 mL methanol was stirred at 65 ^oC for 24 hours. After filtration, the remaining clear solution was kept at room temperature. Brown X-ray quality crystals were obtained upon evaporation of the solvent at room temperature (Scheme 2). Yield: 45.3%, m.p. = 172.5-174.8 ^oC.

6.2.3 Synthesis of 4-(4-bromophenyl)-1-(propan-2-ylidene)thiosemicarbazide 3

4-(4-bromophenyl)-3-thiosemicarbazide (0.49 g, 2.0 mmol) in 10 mL acetone was reacted with $La(NO_3)_3 \cdot 6H_2O$ (0.43 g, 1.0 mmol) in 5 mL acetone, with stirring for 24

hours at room temperature. Brown crystals suitable for the diffraction study were obtained upon recrystallisation from ethanol (Scheme 3). Yield: 42.4%, m.p. = 118.5-121.9 ^{o}C. Anal. Calcd. for $C_{10}H_{12}BrN_3S$ (%): C, 41.97; H, 4.23; N, 14.68; S, 11.20. Found: C, 41.59; H, 4.33; N, 14.76; S, 11.13. IR (cm^{-1}): *v*(N-H) 3288(m), *v*(C-H) 2981(s), *v*(C=N) 1589(s), *v*(C-N) 1265(s), *v*(C=S) 825(s). ^{1}H NMR (DMSO-d_6, δ ppm): 10.41 (s, 1H, C-NH-N), 9.88 (s, 1H, C-NH-C), 7.60-7.58 (d, 2H, Ar), 7.52-7.50 (d, 2H, Ar), 2.09 (s, 6H, -CH_3).

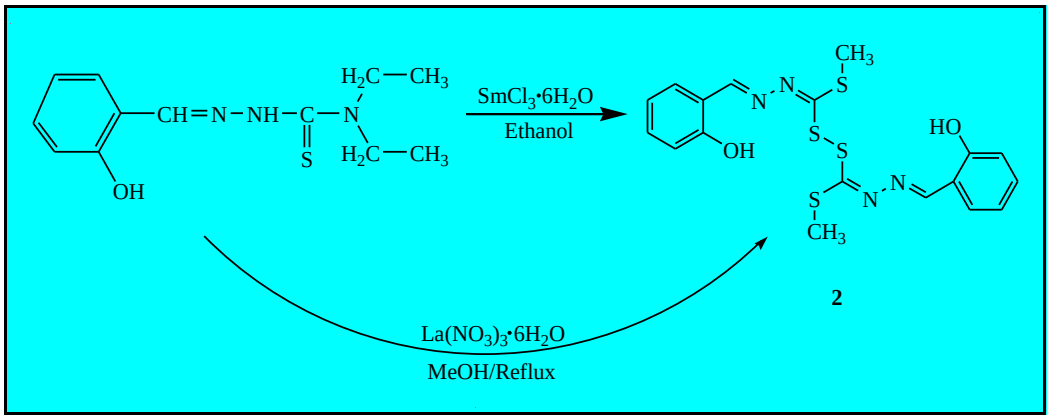

Scheme 2: Synthetic route of compound **2**.

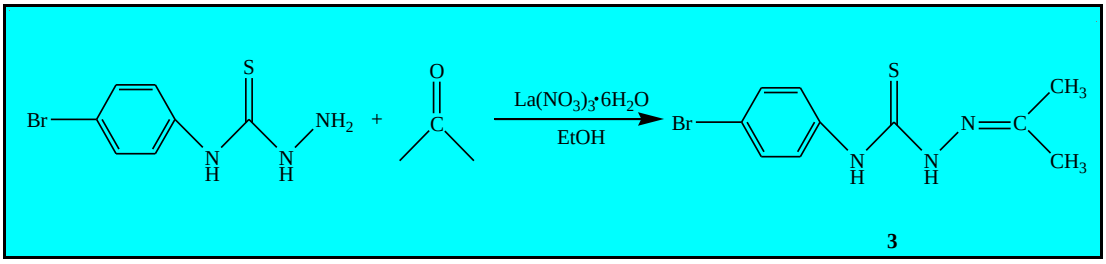

Scheme 3: Synthetic route for the formation of **3**.

6.3 Results and discussion

Attempts to coordinate H_2L_2 and 4-(4-bromophenyl)-3-thiosemicarbazide (H_2L_3) to the 4*f* elements led to unexpected results. Lanthanide-assisted conversion of salicylaldehyde-*N*(4)-diethylthiosemicarbazone and 4-(4-bromophenyl)-3-thiosemicarbazide has occurred to give three novel derivatives. The chemical structures

of the compounds have been confirmed by single-crystal X-ray diffraction analyses, elemental analyses, IR and NMR spectroscopy. Microanalyses of the compounds are in good agreement with their formulations. The obtained compounds are stable in air for weeks and are soluble in most polar solvents.

The reaction of H_2L_2 in the presence of hydrated Ln(III) salts led to the isolation of two new compounds: (*E*)-2-[(*ortho*-hydroxy)benzylidene]-2-(thiomethyl)-thionohydrazide (**1**) and bis[2,3-diaza-4-(2-hydroxyphenyl)-1-thiomethyl-buta-1,3-diene]disulfide (**2**). The latter being a dimer of the former. Compound **1** was formed through substitution of the $–N(CH_2CH_3)_2$ group with the $–SCH_3$ moiety. The important role of sulfur nucleophiles such as thiophenoxide, phenylsulfinate and thiocyanate in bond-breaking and bond-forming in nucleophilic substitution reactions is known [3]. The polarisable nature of sulfur results in the nucleophilic affinity towards saturated and unsaturated carbons [4]. It is likely that the rare-earths assisted in polarising the $–SCH_3$ unit, thereby increasing the nucleophilicity of the sulfur atom and raising its chances of attacking the electron-deficient carbon atom.

The symmetric disulfide (**2**) was derived from the *S*-methyl 3-(2-hydroxybenzylidene)dithiocarbazato scaffold upon oxidative sulfur-sulfur coupling, with the stronger Lewis acid, $SmCl_3·6H_2O$, giving a higher yield than $La(NO_3)_3·6H_2O$.

4-(4-Bromophenyl)-1-(propan-2-ylidene)thiosemicarbazide (**3**) was prepared from the reaction of H_2L_3 with acetone in an ethanolic solution of $La(NO_3)_3·6H_2O$. The isolated Schiff base was a result of a nucleophilic addition reaction in which the amine attacked the electron-deficient carbon atom of acetone (Figure 3) [3,5]. As a hard Lewis acid, $La(NO_3)_3·6H_2O$ assisted in the polarisation of the carbonyl group of acetone, thus modifying its electrophilicity and making it more reactive [6].

Possible reasons for the decomposition of the ligands or non-coordination to the rare-earth ions include the hard-soft acid-base (HSAB) theory and hydrolysis. According to the HSAB theory, lanthanide cations are considered as hard acids. Therefore, as a soft donor, sulfur is not expected to complex well with the lanthanides. Hydrolysis may be

due to the low stability of complexes that form between the hard rare-earths and soft sulfur-donor ligands [7,8]. The exact mechanism of the metal's involvement in the decompositions is a separate topic for further investigation.

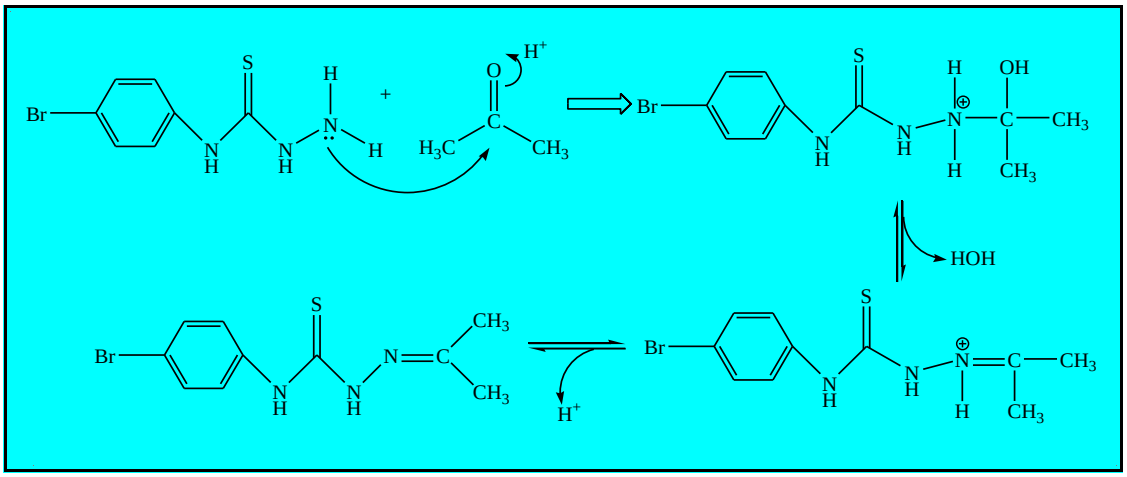

Figure 3: Mechanism of Schiff base formation. With an amine as a nucleophile, proton transfer and loss of water leads to a C=N bond.

6.3.1 Infrared spectroscopy

The IR spectra of H_2L_2, its derivatives and the thiosemicarbazide derivative provide information about the functional groups present in the molecules (Figures 4a and 4b). The band at 3114 cm^{-1} in the H_2L_2 spectrum corresponds to the N-H stretch and this appears at a lower wavenumber (3103 cm^{-1}) for **1** and higher frequency (3288 cm^{-1}) for **3**. This is because **3** has stronger N-H bonds [0.83(2) Å] that vibrate with higher frequency than **1** [N-H; 0.87(2) Å]. Another peak at 1604 cm^{-1} due to the azomethine (-CH=N) group of H_2L_2 is located at 1618, 1616 and 1589 cm^{-1} for **1**, **2** and **3**, respectively. Strong absorption peaks at 760, 750 and 825 cm^{-1} for H_2L_2, **1** and **3**, respectively are assigned to the *ν*(C=S) [1].

The C-H stretching vibration in the thiosemicarbazone (2867 cm^{-1}) is shifted to lower wavenumbers after conversion to compounds **1** (2956 cm^{-1}) and **2** (3150 cm^{-1}). The *ν*(C-H) appears at 2981 cm^{-1} in **3**. Broad bands in the 3620-3270 cm^{-1} region of compounds **1** and **2** can be attributed to the vibrations of the –OH group. Additionally, the *ν*(C-N)

is observed at wavenumbers of 1300 and 1265 cm^{-1} for **1** and **3**, respectively. A high absorbance peak at 947 cm^{-1} for compound **2** is due to the *v*(=C-H) [9].

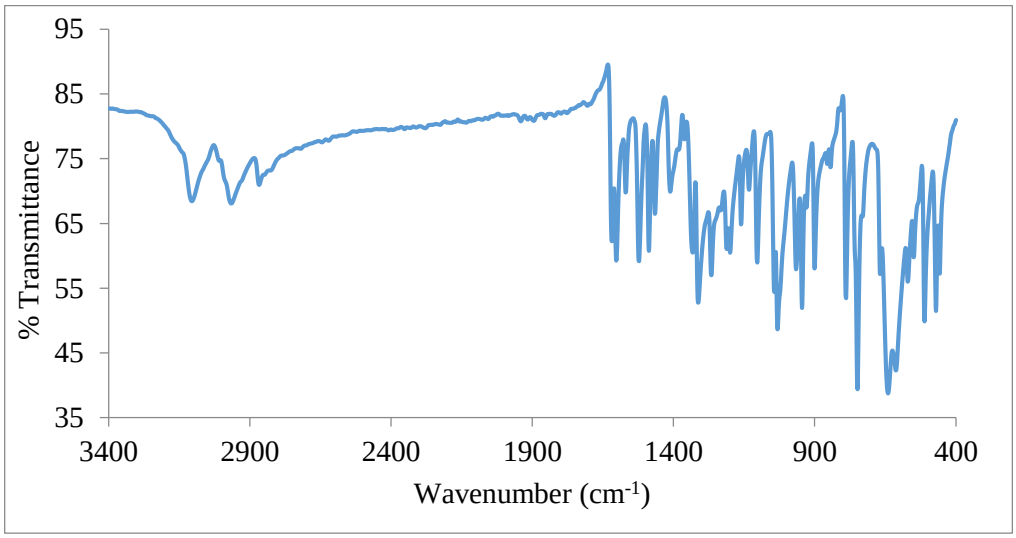

Figure 4a: The IR spectrum of H_2L_2.

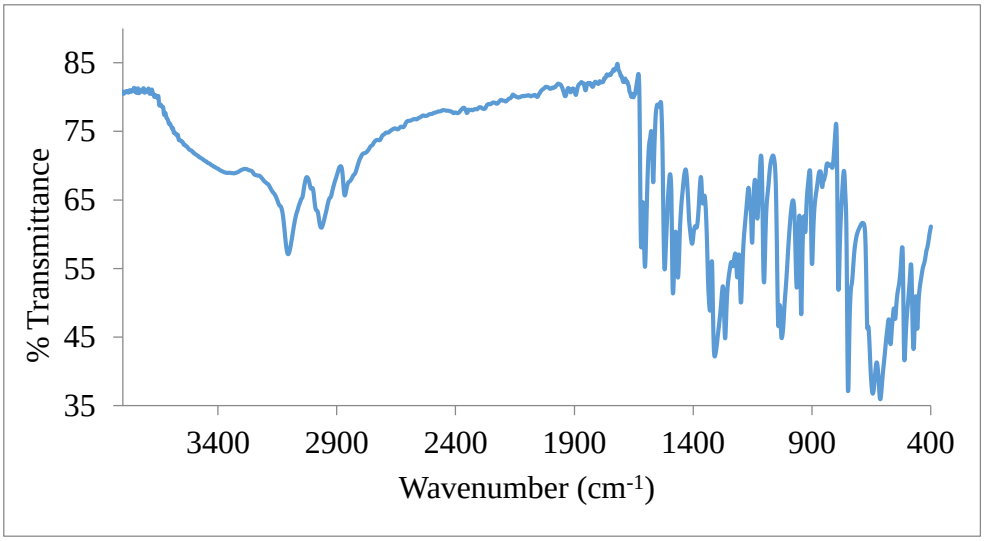

Figure 4b: IR spectrum of compound **1**.

6.3.2 NMR analysis

The ^1H NMR spectrum of H_2L_2 (Figure 5a) in DMSO-d_6 displays singlets at 11.74 and 11.11 ppm and these are ascribed to the thiosemicarbazate –NH and salicylaldehyde

–CH, respectively [1]. The singlet at δ8.55 ppm is assigned to the phenolic –OH proton and upfield of this peak are signals at 7.74 (doublet) and 7.68 ppm (triplet) which are due to the resonance of the two aromatic protons. The proton NMR spectrum also reveals a triplet at 7.37 ppm which is attributed to the two equivalent aromatic protons. The two sets of peaks, a quartet at 4.34 ppm (4H) and a triplet at 1.19 ppm (6H) are assigned to the protons of the two $–CH_2-$ and two $–CH_3$ groups of $–N(CH_2CH_3)_2$, respectively. The ^{13}C NMR spectrum with signal allocation is given in Figure 5b and it further supports the successful synthesis of the starting thiosemicarbazone.

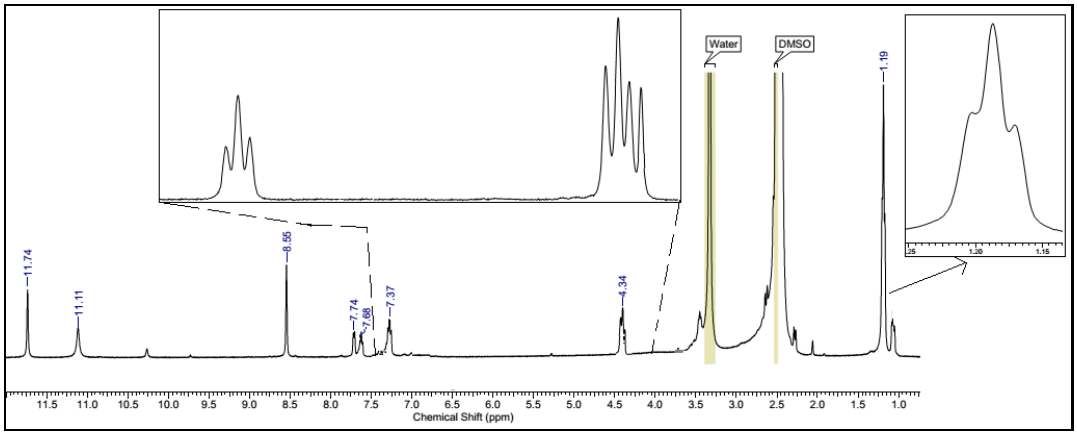

Figure 5a: ^{1}H NMR spectrum of H_2L_2.

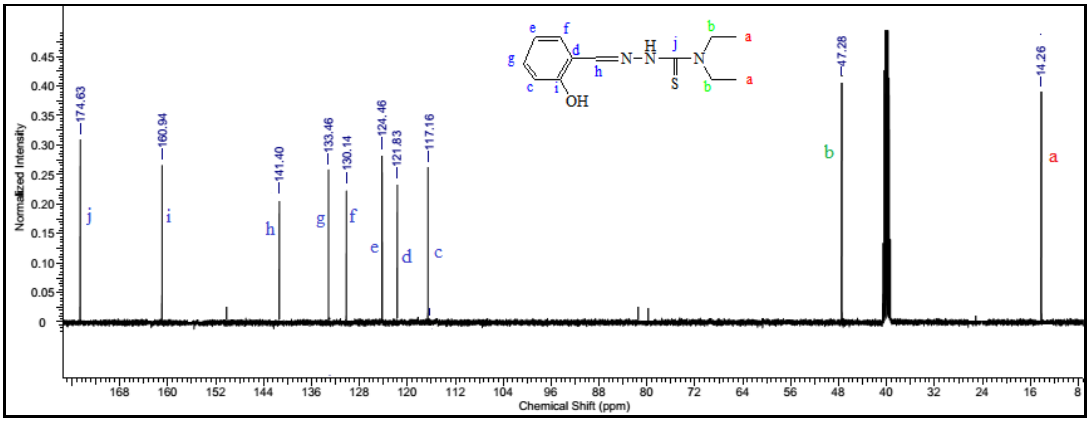

Figure 5b: ^{13}C NMR spectrum of H_2L_2.

The ^{1}H NMR spectrum of **1** (Figure 5c) indicates singlets at 2.54, 8.54, 10.23 and 13.33 ppm, assigned to H_a, H_e, H_f and H_g, respectively. The region 6.88 to 7.68 ppm integrates

for the 4 protons (H_b, H_c and H_d) of the aromatic ring. These signals are well resolved, with a two-proton quartet (6.88-6.94 ppm), a triplet at 7.29-7.33 ppm and a doublet at 7.66-7.68 ppm.

The ^{13}C NMR spectrum of **1** (see Figure 5d) displays ten signals, with the peak at 40 ppm arising from DMSO-d_6. The peaks at 116.89, 119.58, 120.10, 127.79, 132.68 and 157.70 ppm are assigned to the aromatic carbons C_{13}, C_{11}, C_{15}, C_{16}, C_{14} and C_{12}, respectively (refer to Figure 6a for the carbon atom-numbering). The peak due to the methyl carbon (C_3) occurs at the lowest chemical shift of 17.22 ppm. The aliphatic carbons, C_1 and C_2, produce signals at 145.11 and 197.75 ppm, respectively.

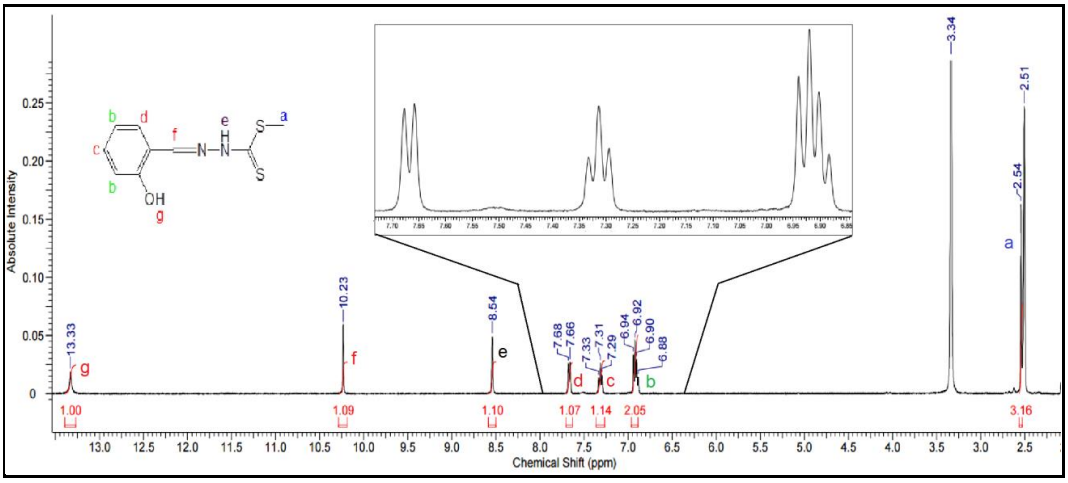

Figure 5c: The ^1H NMR spectrum of compound **1**.

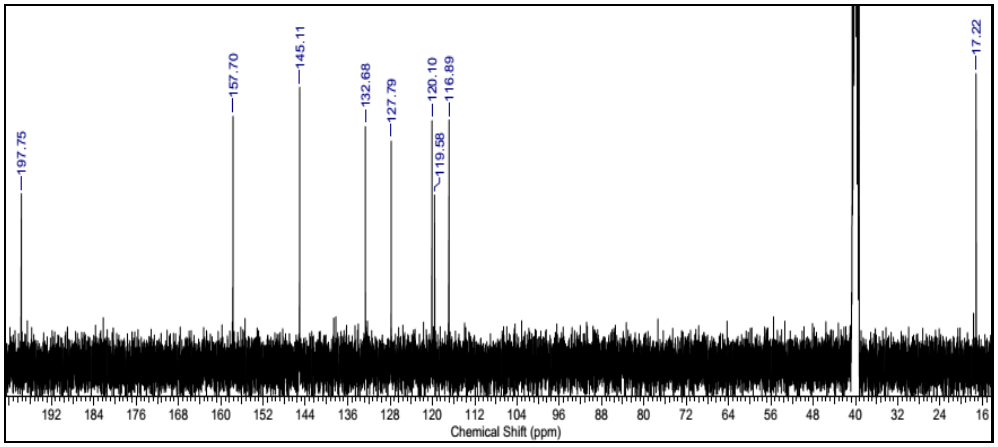

Figure 5d: The ^{13}C NMR spectrum of **1**.

The structure of **2** was confirmed by ^{1}H and ^{13}C NMR spectroscopy (Figures 5e and 5f). The proton NMR of the compound gives a singlet that occurs at low frequency of 13.32 ppm and assigned to the two phenolic –OH protons. This shift to lower field compared to **1** is an indication of the existence of hydrogen bonding in the molecule. The singlets observed at 10.23 and 2.54 ppm are due to the resonances of –CH=N- and $–CH_3$ group protons, respectively. The characteristic doublet-triplet-quartet set of peaks are caused by the resonances of the aromatic protons. The ^{13}C NMR spectrum peaks of the symmetric disulfide are tabulated in Table 1 (See Figure 6c for the carbon atom-numbering scheme).

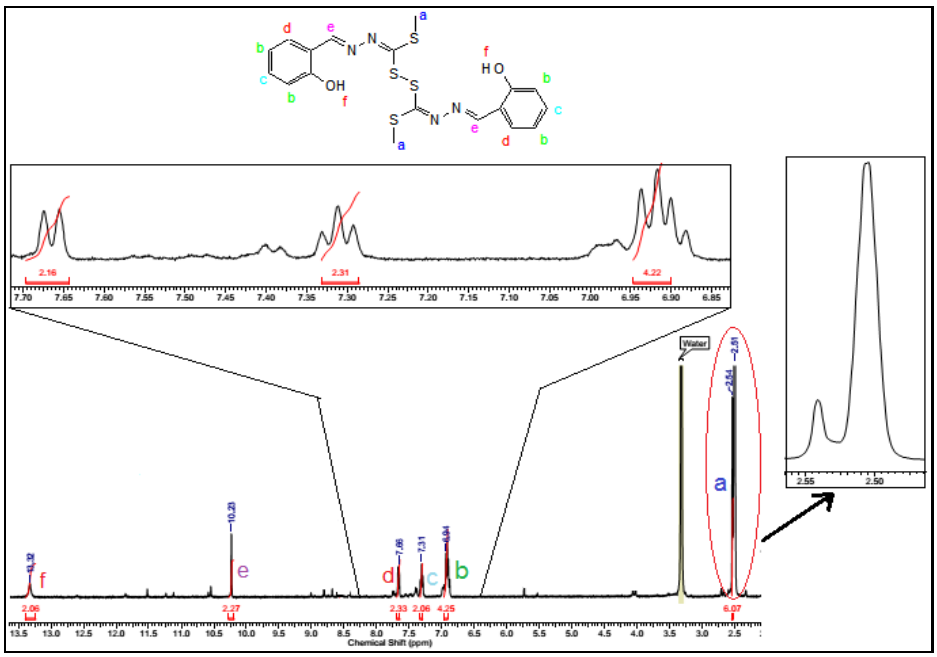

Figure 5e: The ^{1}H NMR spectrum of compound **2**.

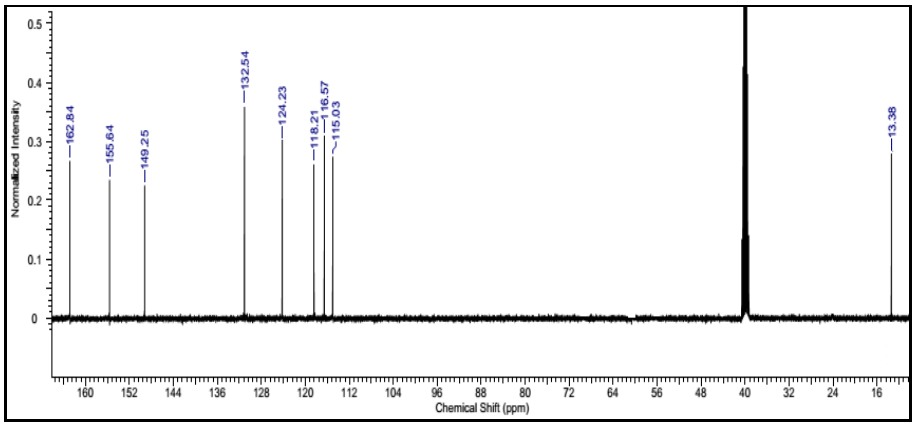

Figure 5f: The ^{13}C NMR spectrum of compound **2**.

Table 1a: Signal assignment in the ^{13}C NMR spectrum of **2**.

Chemical shift (ppm)	Assignment
13.38	C_3 and C_5
115.03	C_{13} and C_{23}
116.57	C_{11} and C_{21}
118.21	C_{15} and C_{25}
124.23	C_{16} and C_{26}
132.54	C_{14} and C_{24}
149.25	C_1 and C_6
155.64	C_2 and C_4
162.84	C_{12} and C_{22}

Figure 5g shows the ^1H NMR spectrum of **3**. The singlet at 2.09 ppm, integrating to 6 protons, is due to the equivalent protons on the methyl groups. Doublet signals are observed for the aromatic protons, H_b and H_c. The proton of the hydrazide group, H_e, resonates further downfield (10.41 ppm) compared to the proton of the aromatic C-NH which has a chemical shift of 9.88 ppm. This is because H_e is closer to the electronegative nitrogen atom (N3) which has a tendency to withdraw electrons towards itself. As a result, H_e has a less electron dense environment, and this leads to less shielding. The ^{13}C NMR of the thiosemicarbazide derivative is shown in Figure 5h, and peak assignment details are given in Table 1b (see the ORTEP plot of compound **3** for the carbon atom-labelling).

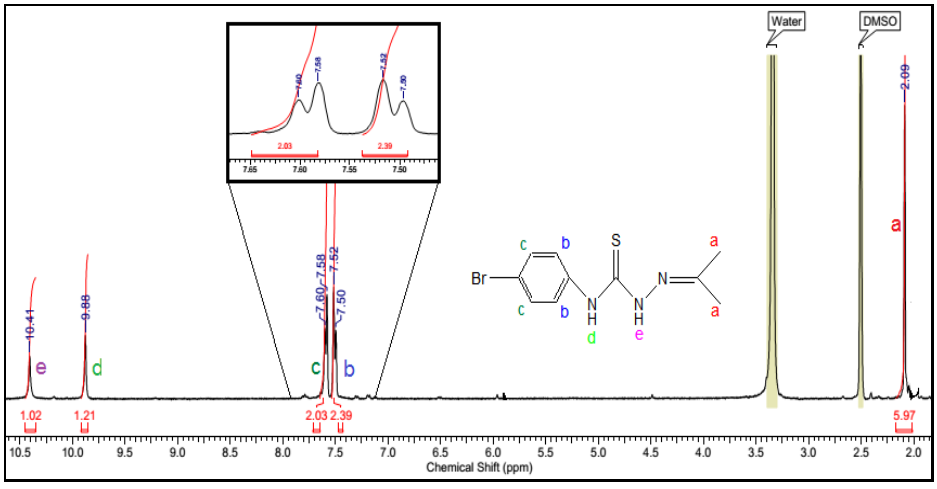

Figure 5g: ^1H NMR spectrum of **3**.

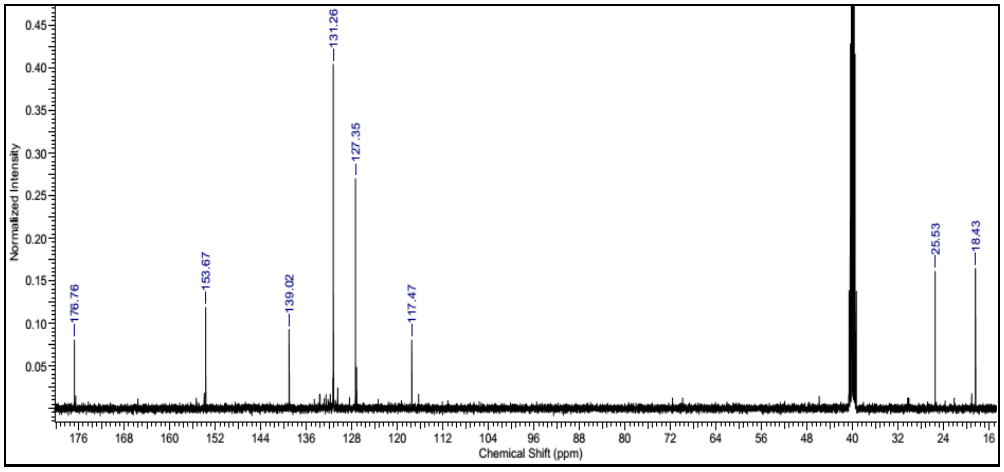

Figure 5h: The ^{13}C NMR spectrum of **3**.

Table 1b: Signal allocation in the ^{13}C NMR spectrum of compound **3**.

Chemical shift (ppm)	Allocation
18.43	C_4
25.53	C_3
117.47	C_{14}
127.35	C_{12} and C_{16}
131.26	C_{13} and C_{15}
139.02	C_{11}
153.67	C_2
176.76	C_1

6.3.3 Crystal data

The ORTEP plot with atom-labelling for **1** is given in Figure 6a. The length of the C(=S)–N(H) bond is 1.3330(19) Å which is indicative of a thioamide resonance involving a C=S bond [1.6668(15) Å]. Both values are found to be shorter than the average reported values for other compounds having a thionohydrazide-derived Schiff base motif whose parameters are on the Cambridge Structural Database. The (*E*) configuration is displayed by the C1=N1 bond [1.2852(19) Å]. The S1-C3-H bond angles are equal to 109^o, hence the C3 atom is sp^3 hybridised. The oxygen atom O1 is

also sp^3 hybridised as seen by the C12-O1-H1A bond angle of 110.0°. The hybridisation of the sulfur atoms, a third-row analogue of oxygen, can also be described using hybrid orbitals. The S1 atom which is bonded to two carbon atoms shows a significant deviation from the ideal tetrahedral geometry. The sp^2 hybridisation of the C1 and N1 atoms is supported by their bond angles of C11-C1-N1 = 121.74(13)° and N2-N1-C1 = 116.48(12)°, respectively [10]. Selected bond distances and angles are listed in Table 2a.

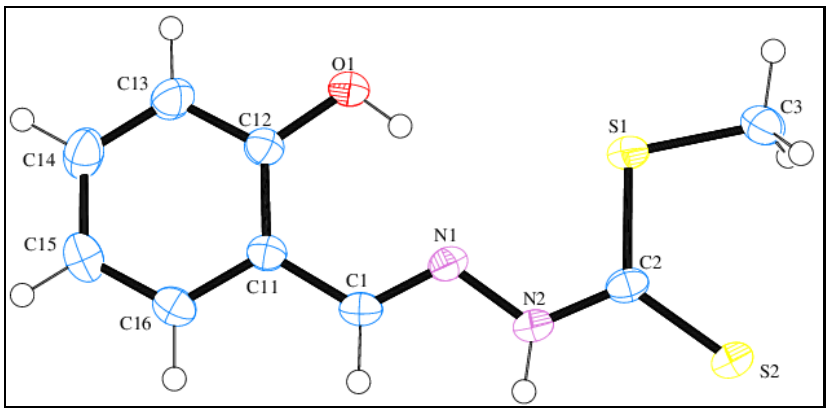

Figure 6a: The ORTEP view of the asymmetric Schiff base **1** (50% probability displacement ellipsoids).

Table 2a: Selected bond lengths and angles in compound **1**.

Bond lengths (Å)		**Bond angles (°)**	
S1–C2	1.7438(14)	C2–S1–C3	102.12(7)
S1–C3	1.7921(16)	N2–N1–C1	116.48(12)
S2–C2	1.6668(15)	C12–O1–H1A	110.00
O1–C12	1.3549(19)	N1–N2–C2	120.77(12)
N1–N2	1.3781(18)	N1– C1–C11	121.74(13)
N1–C1	1.2852(19)	S1–C2–N2	114.10(11)
O1–H1A	0.8400	S2–C2–N2	120.89(11)
N2–C2	1.333(2)	S1–C2–S2	125.02(9)
C1–C11	1.442(2)	N1–N2–H2	117.6(13)
N2–H2	0.87(2)	C2–N2–H2	121.3(13)
C11–C16	1.401(2)	C1–C11–C12	122.72(13)

Hydrogen bonding details in **1** are given in Figure 6b and Table 2b. In the crystal structure of this asymmetric Schiff base, intramolecular O-H···N and intermolecular N-H···S hydrogen bonds are observed next to the C-H···O contacts which assists in stabilising the molecular packing. Hydrogen bonds of the O-H···N type give rise to cyclic patterns in between the hydroxyl group and the imino nitrogen atom, while formation of centrosymmetric dimers is a result of intermolecular hydrogen bonds.

The C-H···O contacts appear to be in a range that falls by more than 0.1 Å below the sum of van der Waals radii of the atoms participating in them. These originate from a hydrogen atom of the thiomethyl group and extend the dimers to undulated strands along [1 0 1]. Considering graph-set analysis on the unary level, $S(6)R^2_2(8)$ and $R^2_2(20)$ are descriptors for classical hydrogen bonds and C-H···O contacts, respectively [11,12]. The shortest intercentroid distance between two centres of gravity was found at 4.0727 Å [13].

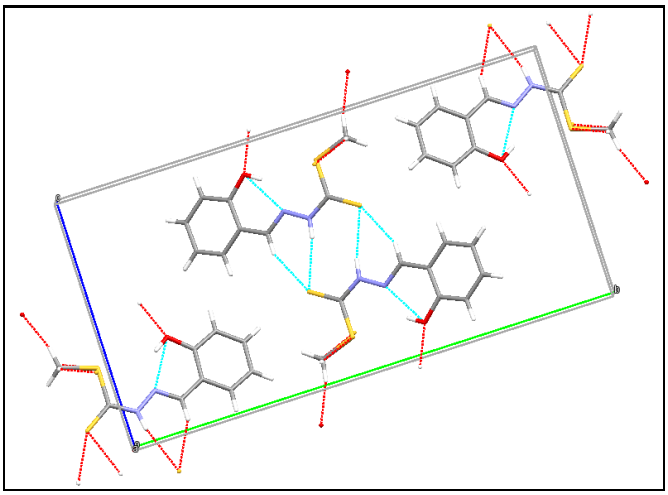

Figure 6b: Hydrogen bonding in **1** from *Mercury 3.6*.

Table 2b: Hydrogen bond geometry (Å, °) for compound **1**.

D*-H···*A	***D*-H**	**H···*A***	***D*···*A***	***D*-H···*A***
O(1)-H(1*A*)···N(1)	0.84	1.92	2.6567(16)	145
N(2)-H(2)···S(2)^{i}	0.87(2)	2.54(2)	3.3910(13)	169.1(18)
C(3)-H(3*B*)···O(1)^{ii}	0.98	2.57	3.4651(19)	152

Symmetry codes: (i) –x+2, -y, -z; (ii) –x+1, -y, -z+1. *D* = donor, *A* = acceptor

Figure 6c shows the structure of the symmetric disulphide **2**. The N1-N2 bond [1.404(2) Å] differ slightly from N3-N4 bond length found at 1.407(2) Å which is also in accordance with the most common bond lengths reported for other compounds featuring a double imine unit of the (C=)N–N(=C) type whose metrical parameters have been deposited with the Cambridge Structural Database. The central S–S bond length = 2.0387(6) Å and the C2-S1-S3-C5 torsional angle = 88.73(9)^{o}. These two values are in agreement with the most commonly reported values for compounds bearing a C–S–S–C moiety involving two sp^2 hybridised carbon atoms [14,15].

Previous studies on bis[isopropoxy(thiocarbonyl)]disulfane, $[(CH_3)_2CHOC(S)S]_2$, reported a dihedral C-S-S-C angle of 85.0(2)^{o} and this is slightly smaller than for compound **2** [14]. The average S-S bond distance was found to be 2.042(2) Å, which is in good agreement with that of **2** [14,15]. The sp^2 hybridisations of these carbons is confirmed by bond angles, S3-C4-N3 = 119.91(15)^{o} [or S3-C4-S4 = 116.89(11)^{o}] and S1-C2-N2 = 121.02(15)^{o} [or S1-C2-S2 = 117.85(11)^{o}]. It is observed that the angles S-C-N > S-C-S. This could be due to the fact that the S-C-N bond angle is associated with a shorter C-N bond which causes the bond angle to widen. Another factor could be the bulky group attached to N2 and N3 which leads to van der Waals repulsions and widening of the S-C-N angle [16].

The average C-O bond length is 1.354 Å and the C-S bond distance lies in the range 1.719(2) to 1.790(2) Å. These bond distances are in agreement with those found in literature [15]. The reported bond lengths agree well with those of *β*-oxodithioesters, such as methyl 3-(4'-phenyl)-3-hydroxy-2-propenedithiolate, with C-O bond distances that lie in the range 1.329(2)-1.334(3) Å. The average single C-S bond length of the *β*-oxodithioester [1.786(3)-1.801(3) Å] is significantly shorter than the carbon-sulfur double bonds in **1** and **3** that were found to be 1.6668(15) and 1.6686(16) Å, respectively [15]. The imine-type double bonds towards aromatic moieties are (*E*)-configured while they are (*Z*)-configured towards the central S–S moiety in both cases.

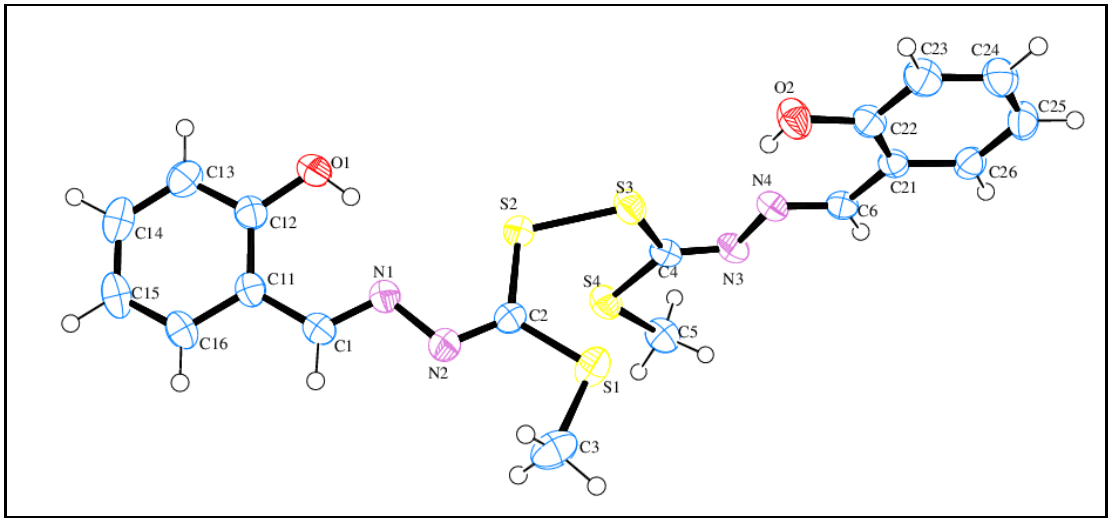

Figure 6c: The ORTEP diagram (50% ellipsoidal probability) with atom-numbering scheme for the symmetric disulfide **2**.

Table 2c: Selected bond lengths and angles in **2**.

Bond lengths (Å)		**Bond angles (°)**	
O1-C12	1.355(2)	N1-C1-C11	121.44(16)
O2-C22	1.354(2)	C1-N1-N2	114.39(14)
N1-N2	1.407(2)	C6-N4-N3	113.21(15)
N3-N4	1.404(2)	C2-N2-N1	111.33(14)
S1-C2	1.7908(18)	C4-N3-N4	112.56(15)
S4-C5	1.7375(18)	C2-S1-C3	99.98(11)
N2-C2	1.283(2)	C4-S4-C5	101.46(10)
N3-C4	1.285(2)	C12-O1-H1A	109.00

Figure 6d and Table 2d give details on the hydrogen bonding network in **2**. Classical intramolecular hydrogen bonds of the O–H···N type are apparent next to C–H···O contacts. Similar to **1**, the range of C-H···O contacts falls by more than 0.1 Å below the

sum of van der Waals radii of the atoms participating in them. The intramolecular hydrogen bonds arise from the interaction of the phenolic hydroxyl group and one of the imine-type nitrogen atoms. The first type of C–H···O contacts are maintained by one of the vinylic hydrogen atoms as the donor and the oxygen atom of the hydroxyl group of the other half of the molecule as the acceptor. The second kind of C–H···O contacts exists between the phenolic hydrogen in the *ortho* position and the oxygen atom of the hydroxyl group of the other half of the molecule, thus leading to centrosymmetric dimers.

Graph-set analysis shows that the descriptor for these C-H···O contacts is $S(6)S(6)C^1_1(14)R^2_2(34)$, and in total the molecules are connected to layers perpendicular to the crystallographic *a* axis [11,12]. Furthermore, one C-H···π interaction exists involving one of the hydrogen atoms of the methyl group. The shortest intercentroid distance between two centres of gravity is found to lie between the two different phenyl groups in neighbouring molecules and was measured at 5.1327(11) Å [17].

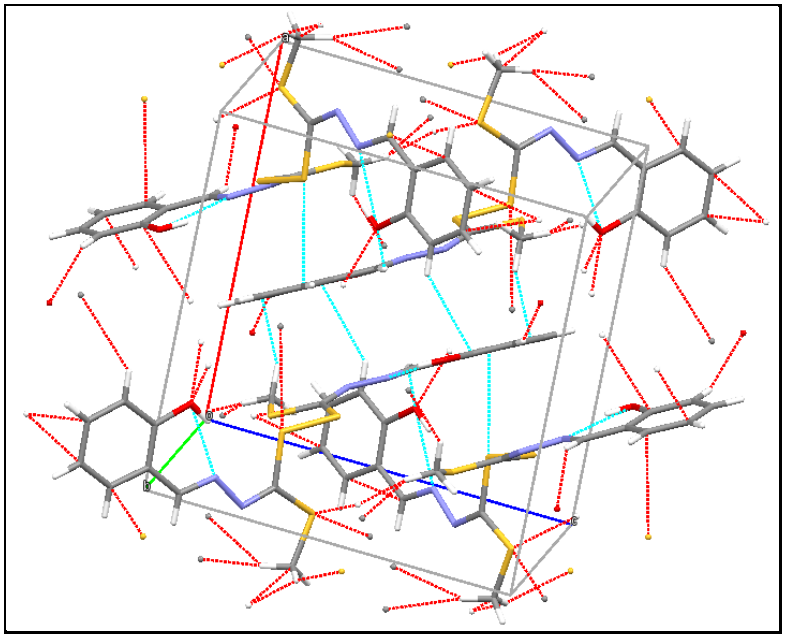

Figure 6d: Hydrogen bonding network in **2**.

Table 2d: Hydrogen bond parameters (Å, °) for compound **2**.

D*-H···*A	***D*-H**	**H···*A***	***D*···*A***	***D*-H···*A***
O(1)-H(1A)···N(1)	0.84	1.89	2.629(2)	146
O(2)-H(2)···N(3)	0.84	1.91	2.649(2)	146
C(4)-H(4)···O(1)^{i}	0.95	2.57	3.380(2)	144
C(23)-H(23)···O(1)^{ii}	0.95	2.56	3.451(2)	156
C(3)-H(3*B*)···C_g^{iii}	0.98	2.73	3.578(2)	146

Symmetry codes: (i) x, -y+1/2, z-1/2; (ii) –x, -y+1, -z; (iii) –x+1, y-1/2, -z+1/2.

A thermal ellipsoidal plot (ORTEP-3) at 50% probability level for **3** is given in Figure 6e. The C=S bond length of 1.6686(16) Å is in good agreement with other thioketones. Examples include thiobenzophenone and thioformaldehyde where the C=S bond lengths are equal to 1.66 and 1.64 Å, respectively [18]. The C1-N1 bond length of 1.343(2) Å is slightly different from the C1-N2 bond length of 1.366(2) Å, with the shorter bond being towards the nitrogen atom bonded to the aromatic system. This indicates a delocalisation of electrons near the aromatic system [19]. The C-Br distance of 1.9052(17) Å agrees well with those reported for the starting compound, 4-(4-bromophenyl)-3-thiosemicarbazide, (average = 1.902 Å) [19]. Selected bond lengths and angles of **3** are listed in Table 2e.

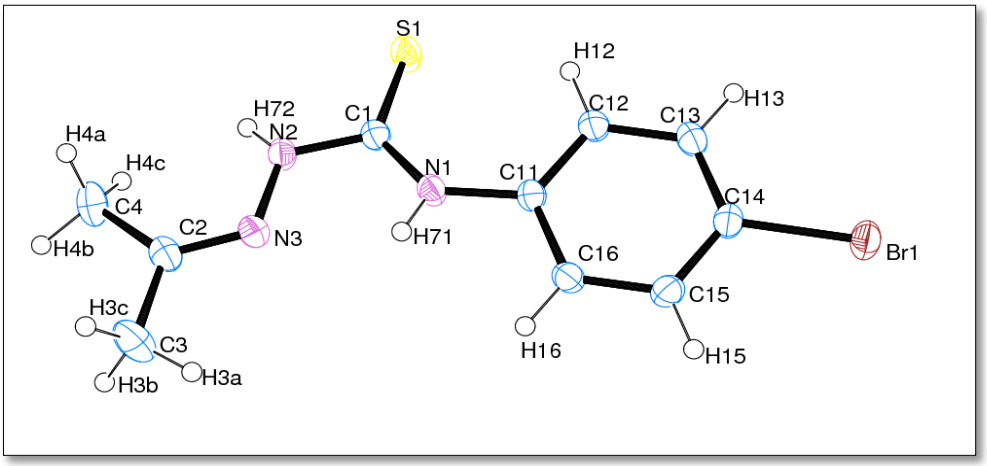

Figure 6e: The ORTEP plot of the thiosemicarbazide derivative **3** (50% probability displacement ellipsoids).

Table 2e: Selected bond lengths and angles in **3**.

Bond lengths (Å)		**Bond angles (°)**	
Br–C14	1.9052(17)	C1–N1–C11	132.37(14)
S1–C1	1.6686(16)	C1–N1–H71	112.7(15)
N1–C1	1.343(2)	C11–N1–H71	114.8(15)
N1–C11	1.408(2)	C1–N2–N3	119.02(14)
N1–H71	0.83(2)	C1–N2–H72	117.0(15)
N2–C1	1.366(2)	N3–N2–H72	122.1(16)
N2–N3	1.3855(19)	C2–N3–N2	117.92(15)
N2–H72	0.83(2)	N1–C1–N2	113.02(14)
N3–C2	1.278(2)	N1–C1–S1	128.43(13)
C2–C4	1.488(3)	N2–C1–S1	118.54(13)
C2–C3	1.495(3)	N3–C2–C4	125.92(17)
C3–H3A	0.9800	C4–C2–C3	117.78(16)

Intramolecular N-H···N and intermolecular N-H···Br hydrogen bonding occurs in compound **3** next to C-H···S contacts and these play an important role in the stabilisation of the molecular packing (Figure 6f and Table 2f). The range of C-H···S contacts falls by more than 0.1 Å below the sum of the van der Waals radii of the atoms participating in them. Classical intermolecular hydrogen bonds occur between the hydrogen atom in the *ortho* position and the bromine atom, resulting in centrosymmetric dimers.

Graph-set analysis gives $S(5)C^1_1(9)$ as the descriptor for the classical hydrogen bonds on the unary level, whereas $R^2_2(14)$ is the descriptor for the C–H···S contacts on the same level [11,12]. In total, the molecules are connected to strands along the crystallographic *b* axis and the shortest intercentroid distance between two centers of gravity was found at 4.5388(10) Å [20].

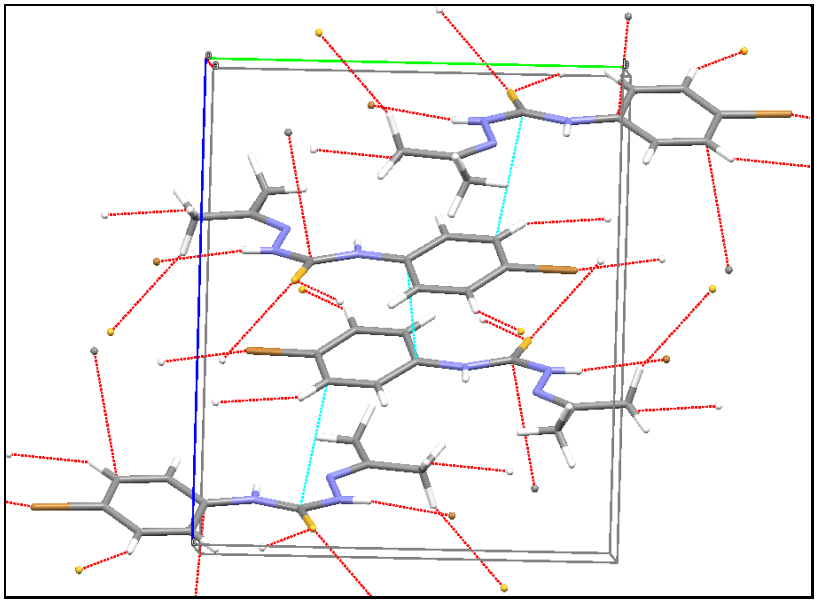

Figure 6f: Packing diagram showing one unit cell in **3**.

Table 2f: Hydrogen bond geometry (Å, °) for compound **3**.

D*-H···*A	***D*-H**	**H···*A***	***D*···*A***	***D*-H···*A***
N(1)-H(71)···N(3)	0.83(2)	2.09(2)	2.568(2)	116.9(19)
N(2)-H(72)···Br(1)^{i}	0.83(2)	3.03(2)	3.8176(15)	159.3(19)
C(13)-H(13)···S(1)^{ii}	0.95	2.88	3.7731(17)	158

Symmetry codes: (i) x, y-1, z; (ii) –x, -y+1, -z+1

6.3.4 Thermal analysis

Thermal behaviour of compound **1** was investigated with TG and DSC measurements (Figures 7a and 7b). From the TG curve it can be concluded that the compound starts decomposing (weight loss) at about 191 ºC, with major weight loss occurring rapidly between 193 and 264 ºC.

Investigation of the DTG curve reveals that the sequence of degradation starts with degradation of solvent methanol at 65 ºC, followed by decomposition in two steps as shown by the two peaks at 206 and 250 ºC.

The DSC curve shows an endothermic peak with a maximum at 208.09 ºC. The endothermic peak is in the temperature range of 196.07 ºC to 234.58 ºC, which fits well with that of weight loss in the TG curve.

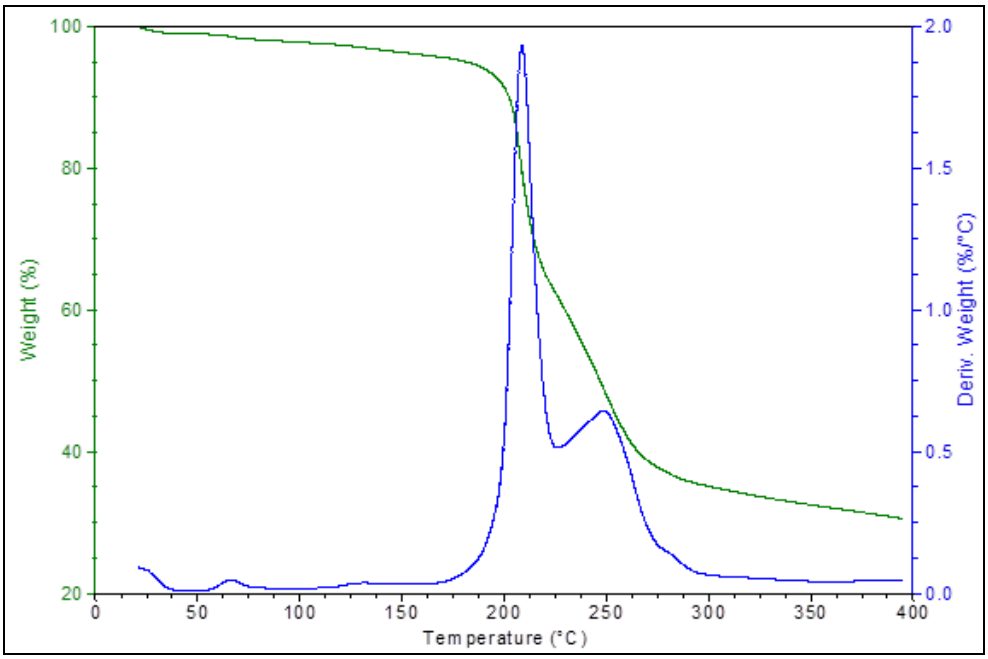

Figure 7a: TG and DTG curves for compound **1**.

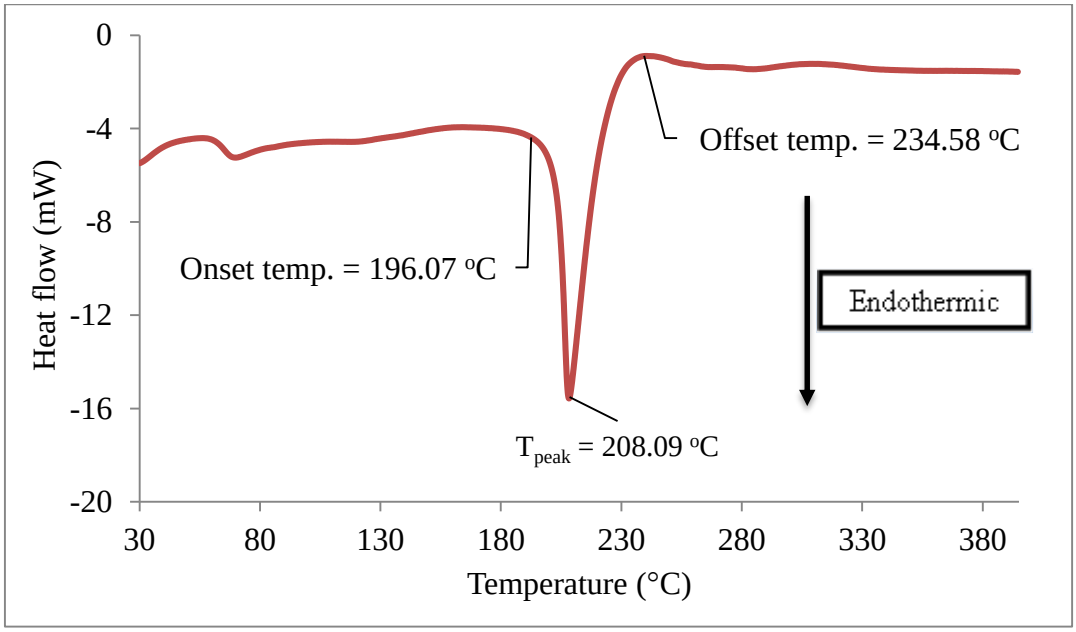

Figure 7b: Differential scanning calorimetry thermogram for compound **1**.

Thermal analysis of **2** (see Figures 7c and 7d) shows a TG curve with mass loss commencing at 176 ^{o}C, which is very rapid until reaching 248 ^{o}C. The upper limit of stability of the compound (176 ^{o}C) is lower than that of its monomer, **1** (191 ^{o}C). The lower stability in the dimer can be attributed to the low strength of the S-S bond which is reflected in its bond distance. From the TG plot it seems like a single-stage decomposition process. However, upon investigation of the DTG, a decomposition profile which occurs through two steps is revealed, as shown by two peaks in the temperature range 150-250 ^{o}C.

The DSC curve shows two endothermic peaks with maxima at 169.17 ^{o}C and 193.38 ^{o}C, corresponding to the two decomposition steps on the DTG curve, followed by a recrystallisation process which peaks at 255.65 ^{o}C [21].

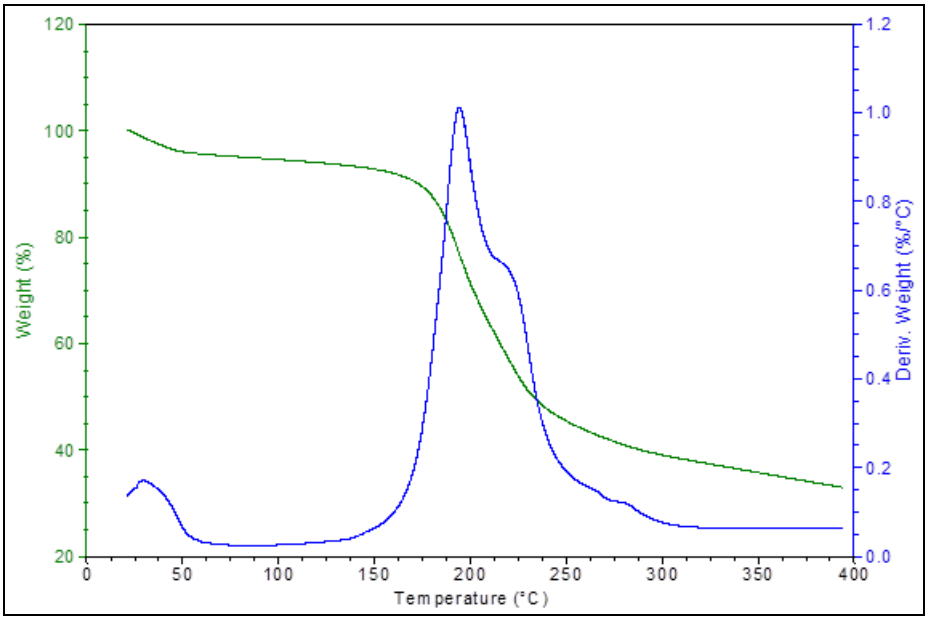

Figure 7c: TG and DTG curves for compound **2**.

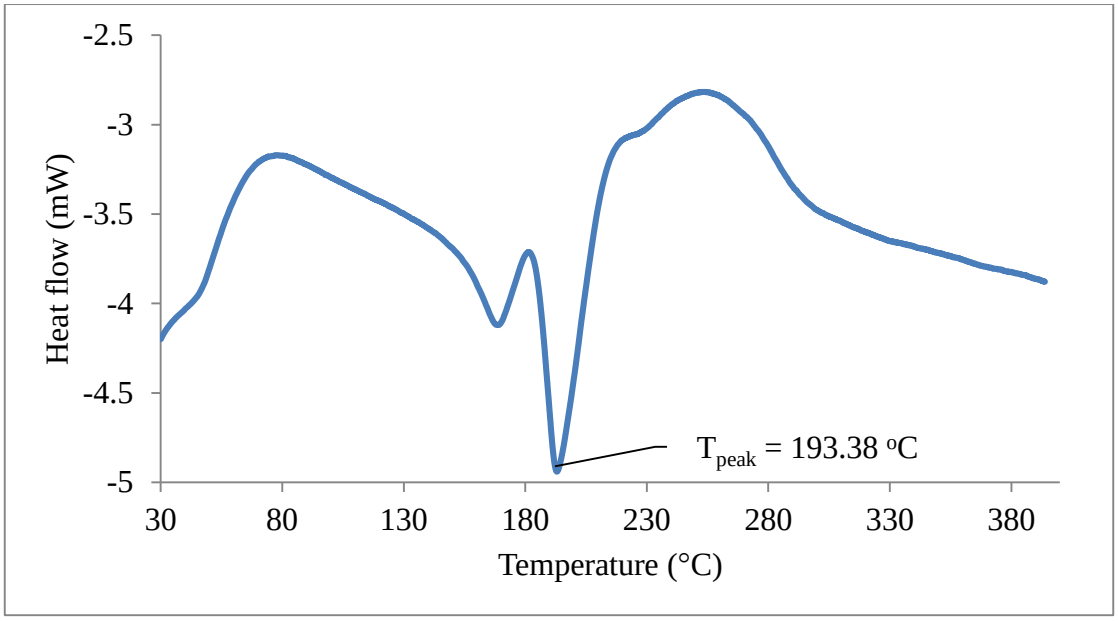

Figure 7d: DSC thermogram for compound **2**.

6.4 Conclusion

It was considered worthwhile to investigate the coordination ability of salicylaldehyde-*N*(4)-diethylthiosemicarbazone in complexation reactions with lanthanides. However, unexpected reactions occurred. Previous studies on H_2L_2 revealed that the favourable configuration in coordination has sulfur as one of the donor sites. The soft sulfur atom of the thiosemicarbazone or thiosemicarbazide is not a good site for coordination to hard Lewis acids. Thus, all attempts to coordinate the thiosemicarbazone and thiosemicarbazide proved unsuccessful, and was ascribed to the hard nature of the Ln(III) ion having a preference for similar B-type donor-atoms.

Schiff base type tridentate *O*,*N*,*S*- and bidentate *N*,*S*-donor ligands were successfully isolated from a thiosemicarbazone and a thiosemicarbazide with the assistance of the lanthanides. Generally, they are obtained upon acid-catalysed condensation of a primary amine and a ketone.

6.5 Crystallographic data

Table 3a: Crystal data for compound **1**.

Formula	$C_9H_{10}N_2OS_2$
M_r (g.mol^{-1})	226.33
Crystal system	Monoclinic
Space group	$P2_1/n$
Hall symbol	-P 2yn
a, *b*, *c* [Å]	4.0727(2), 22.2556(13), 11.4854(6)
α, β, γ (°)	90, 98.364(3), 90
V (Å^3)	1029.97(10)
Z	4
ρ (g.cm^{-3})	1.460
μ (mm^{-1})	0.484
F (000)	472
Crystal size (mm)	0.05 × 0.11 × 0.78
Temperature (K)	200
λ (Å)	0.71073
θ (min-max) (°)	1.8, 28.3
Data set	$-5\leq h\leq 5$; $-29\leq k\leq 23$; $-15\leq l\leq 12$
Tot., Uniq. Data, R_{int}	9308, 2566, 0.019
Observed data [I>2.0σ(I)]	2072
N_{ref}, N_{par}	2566, 133
$R[F^2>2\sigma(F^2)]$, $wR(F^2)$, *S*	0.0295, 0.0725, 1.03
$\Delta\rho_{min}$, $\Delta\rho_{max}$ (e.Å^{-3})	-0.19, 0.26

Table 3b: Crystal data for compound **2**.

Formula	$C_{18}H_{18}N_4O_2S_4$
M_r (g.mol^{-1})	450.60
Crystal system	Monoclinic
Space group	$P2_1/c$
a, b, c [Å]	12.3623(6), 14.0153(7), 11.9869(6)
β (°)	93.148(2)
V (Å^3)	2073.73(18)
Z	4
ρ (mg.m^{-3})	1.443
Mo *Kα* radiation, λ (Å)	0.71073
μ (mm^{-1})	0.48
Crystal size (mm)	0.57 × 0.23 × 0.19
Temperature (K)	200
θ (min-max) (°)	0.888, 1.000
No. of measured, independent and observed [I>2σ(I)] reflections	19638, 5147, 4144
R_{int}	0.034
$(\sin\theta/\lambda)_{max}$ (Å^{-1})	0.667
$R[F^2>2\sigma(F^2)]$, $wR(F^2)$, S	0.036, 0.099, 1.02
$N_{reflections}$, $N_{parameters}$	5147, 257
$\Delta\rho_{min}$, $\Delta\rho_{max}$ (e.Å^{-3})	-0.23, 0.38

Table 3c: Crystal data for compound **3**.

Formula	$C_{10}H_{12}BrN_3S$
M_r (g.mol^{-1})	286.20
Crystal system	Monoclinic
Space group	$P2_1/n$
Temperature (K)	200
a, *b*, *c* [Å]	8.5610(2), 11.0120(3), 13.2140(4)
β (°)	107.345(1)
V (Å^3)	1189.09(6)
Z	4
ρ (mg.m^{-3})	1.599
Mo *Kα* radiation, λ (Å)	0.71069
μ (mm^{-1})	3.60
Crystal size (mm)	0.37 × 0.23 × 0.11
θ (min-max) (°)	0.746, 1.000
No. of measured, independent and observed [I>2σ(I)] reflections	13943, 3076, 2672
R_{int}	0.019
$(\sin\theta/\lambda)_{max}$ (Å^{-1})	0.676
$R[F^2>2\sigma(F^2)]$, $wR(F^2)$, *S*	0.025, 0.065, 1.05
$N_{reflections}$, $N_{parameters}$	3076, 146
$\Delta\rho_{min}$, $\Delta\rho_{max}$ (e.Å^{-3})	-0.25, 0.74

6.6 References

[1] N.C. Saha, R. Pradhan, M. Das, N. Khatun, D. Mitra, A. Samanta, A.M.Z. Slawin, A.D. Jana, J. Klanke and E. Rentschler, *J. Coord. Chem.*, **67** (2014) 286-287.

[2] A.M. Hammam, M.A. EL-Gahami, Z.A. Khafagi, M.S. AL-Salami and S.A. Ibrahim, *J. Mater. Environ. Sci.*, **6** (2015) 1596.

[3] T.N. Sorell, *Organic Chemistry*, 2nd edn, (2006) 608.

[4] A.J. Parker, *Organic Sulfur Compounds*, (1961) 103.

[5] J. McMurry, *Organic Chemistry*, 9th edn, (2015) 612.

[6] I.V. Basalov, S.C. Rosca, D.M. Lyubov, A.N. Selikhov, G.K. Fukin, Y. Sarazin, J-F. Carpentier and A.A. Trifonov, *Inorg. Chem.*, **53** (2014) 1654.

[7] M.D. Regulacio, M.H. Pablico, J.A. Vasquez, P.N. Myers, S. Gentry, M. Prushan, S. Tam-Chang and S.L. Stoll, *Inorg. Chem.*, **47** (2008) 1512.

[8] S. Cotton, *Lanthanide and Actinide Chemistry*, John Wiley & Sons, 2006, 46.

[9] P. Chen, H. Chen, P. Yan, Y. Wang and G. Li, *Cryst. Eng. Comm.*, **13** (2011) 6238.

[10] J. McMurry, *Organic Chemistry*, **1** (2009) 20.

[11] J. Bernstein, R.E. Davis, L. Shimoni and N.L. Chang: *Patterns in Hydrogen Bonding: Functionality and Graph Set Analysis in Crystals*., *Angew. Chem.* Int. Ed. Engl. **34** (1995) 1555–1573.

[12] M. C. Etter, J.C. MacDonald and J. Bernstein: *Graph-set analysis of hydrogen-bond patterns in organic crystals.*, *Acta Crystallogr*. **B46** (1990) 256–262.

[13] T. Madanhire, A. Abrahams, E.C. Hosten and R. Betz, *Z. Kristallogr. NCS*, **230** (2015) 13-14.

[14] C. Chatgilialoglu and K.-D. Asmus, *Sulfur-Centered Reactive Intermediates in Chemistry and Biology, Series A: Life Sciences*, **197** (1990) 230.

[15] M.C. Mancilla-Gonzalez, V. Jancik, D. Martinez-Otero, M. Moya-Cabrera and I. Garcia-Orozco, *J. Organomet. Chem.*, **770** (2014) 36.

[16] W.A. Shirley, R. Hoffmann and V.S. Mastryukov, *J. Phys. Chem.*, **99** (1995) 4025.

[17] T. Madanhire, A. Abrahams, E.C. Hosten and R. Betz, *Z. Kristallogr. NCS*, **230** (2015) 89-90.

[18] R. Sustmann, W. Sicking and R. Huisgen, *J. Am. Chem. Soc.*, **125** (2003) 14427.

[19] S. Seth, A. Biswas, A. Banerjee, S.K. Chattopadhay and S. Ghosh, *Acta Cryst.*, **C52** (1996) 2377-2378.

[20] T. Madanhire, A. Abrahams, E.C. Hosten and R. Betz, *Z. Kristallogr. NCS*, **230** (2015) 67-68.

[21] E. Klata, K. Van de Velde and I. Krucinska, *Polymer Testing*, **22** (2003) 929–929.